IRE Transactions

ON MILITARY ELECTRONICS

Volume MIL-3 **OCTOBER, 1959** **Number 4**

U. S. AIR FORCE SPACE ISSUE

PUBLISHED BY THE

PROFESSIONAL GROUP ON MILITARY ELECTRONICS

IRE TRANSACTIONS® ON MILITARY ELECTRONICS

Published by the Institute of Radio Engineers, Inc., for the Professional Group on Military Electronics at 1 East 79th Street, New York 21, New York. Responsibility for the contents rests upon the authors, and not upon the IRE, the Group, or its members. Individual copies available for sale to IRE-PGMIL members at $1.30; to IRE members at $1.95; and to nonmembers at $3.90.

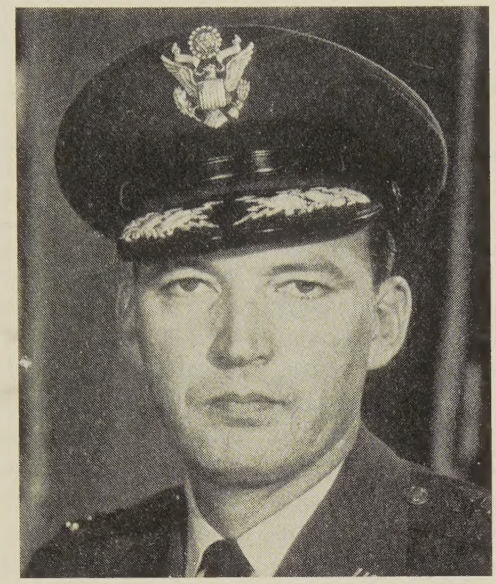

Lt. General Bernard A. Schriever

Bernard A. Schriever was born in Bremen, Germany, on September 14, 1910. He came to the United States with his parents in 1917 and was naturalized in 1923. He received his early schooling in San Antonio, Texas, and was graduated from Texas A & M, College Station, Texas, in 1931, with a B.S. degree in engineering. He received the M.S. degree in aeronautical engineering in 1942 from Stanford University, Stanford, Calif.

During World War II, he organized material and maintenance supply lines for the 5th Air Force Service Command, and flew 63 combat missions in the South Pacific. At the war's end, he was Commander, Advanced Headquarters, Far East Air Service Command.

In 1946, he was assigned to Air Force Headquarters as Chief, Scientific Liaison Section, Deputy Chief of Staff, Material. In 1949, he entered the National War College. Following his graduation, he returned to Headquarters, USAF, for assignment as Assistant DCSD for Development Planning.

He became Assistant to the Commander, Air Research and Development Command, in May, 1954. In this position, he organized the Ballistic Missile Division (then Western Development Division) and was its first commander. This organizational arrangement provided a clear line of authority to top echelons in the Air Force and the Department of Defense.

In August of that year, he assumed the additional responsibilities of Commander, Air Force Ballistic Missile Division, ARDC. In this position, he implemented the unique management concepts by which the ARDC/AMC/SAC team develops the Atlas, Titan, Thor, and Minuteman ballistic missile weapon systems, along with their complementary space systems and early warning and communications satellites, and brings them to initial operational status. One of the most far-reaching of these management concepts is that of concurrency, wherein all phases of the normal design-to-deployment cycle are pursued simultaneously rather than sequentially. Concurrency was an important factor in enabling the scientific-industrial-military team to cut roughly in half the normal weapon system development cycle.

In April, 1959, General Schriever was appointed Commander, ARDC, with the rank of Lieutenant General. ARDC includes eleven major research, development, and test centers, and two major development branches: the Ballistic Missile Division and the Air Defense Systems Integration Division.

Guest Editorial

FOR many years the Air Force has manifested an intense interest in science and technology. Because of this interest, it has initiated or supported a large number of programs which have contributed in a major way to aeronautics and space. Examples of some positive results are the development of the first large liquid rocket engines in this country; the development of the precision-floated gyro capability at the Instrumentation Laboratory, Massachusetts Institute of Technology; and numerous contributions to aviation medicine, to the basic knowledge of stability and control, and to systems engineering. Major improvement of airborne computers by the Air Force has provided a firm basis for later missile and space applications. Light-weight components developed and tested under Air Force sponsorship have likewise found many applications. Our stellar inertial and terminal guidance techniques are likely to find application in space technology as they already have in missiles.

In the past five years, the state-of-the-art has received an even greater impetus because of the accelerated ballistic missile programs. These programs have benefited from the assistance of some of the best scientific, technical, and managerial talent in the country. The keynote of the entire effort has been teamwork and cooperation among science, industry, and the military. The result has been a compression of the time between initial planning and operational availability of important weapon systems, with numerous corollary results such as major additions to production and test facilities, and to the experience of personnel.

Air Force space programs such as Discoverer, Atlas in orbit, and the Thor-Able series came as a natural consequence of the vehicles, facilities and experience developed in our ballistic missile programs. The result of these programs has been some outstanding successes in space exploration, with a broad capability for further important work in space by the Air Force and by other agencies. A little thought is sufficient to convince one that certain space applications are a necessary adjunct to strategic weapon systems such as ballistic missiles. It is therefore our intention to continue to pursue new programs with great vigor. Without doubt, a sizeable portion of our research and development budget will be devoted to advanced systems and techniques related to space applications. It is obvious that a substantial part of this will be in electronics, guidance, communications, and related areas.

The advances in technology which I have mentioned have resulted in a number of significant technical papers, some of which have already been published. Examples of the subjects are tropospheric propagation, accelerometers, gyroscopes, testing, long and short baseline radio-guidance systems, inertial guidance, computer circuitry, and reliability. The paper on "Baseline Guidance Systems," by Grisetti and Mullen, published in the December, 1958 issue of these TRANSACTIONS, was based upon work performed in one of our programs. Scientists and engineers working with us have been encouraged to publish the results of their work and to participate in lectures and in symposia. The accompanying papers are exemplary of some recent work by scientists and engineers on our teams. Publication of such articles is consistent with my belief that the maximum dissemination of unclassified information is important and is very much in the national interest.

B. A. SCHRIEVER
Lieutenant General, USAF

Scientific Objectives of the Able-3 Program*

APPLIED PHYSICS DEPARTMENT, SPACE TECHNOLOGY LABORATORIES, INC.†

Summary—**The purpose of the Able-3 program is to place a scientific observatory in a highly elliptic satellite orbit. A scintillation counter, ion chamber, Geiger counter, and proportional counter telescope in the payload permit comprehensive mapping of corpuscular radiation over a large volume of the geomagnetic region, including the Van Allen radiation belts. Simultaneously, the fundamental static quantities, electron density, and vector magnetic intensity are to be measured. A VLF experiment is included to measure upper atmosphere VLF noise and to study the propagation characteristic of VLF between the ground and the satellite. A radio scintillation experiment using radio telescopes will measure the effects of ionospheric irregularities on amplitude and phase. Micrometeorite detection equipment in the payload provides a two-point momentum spectrum of micrometeorites encountered, and an image scanner is included to examine reflection characteristics of the earth.**

I. Introduction

THE goals of the Able-3 program in placing a scientific observatory in a large elliptic satellite orbit (nominal apogee 20,000 miles, perigee 150 miles) are to provide scientific data concerning the earth and its adjacent space and to test the equipment for application to later space flights. It is the purpose of this paper to establish the framework of scientific background and specific objectives and instrumentation for the Able-3 scientific measurements.

The most important general knowledge which has emerged during the past decade or so, and which is strongly supported by the IGY findings, is the great degree of intimacy between solar and ionospheric weather. It is no longer adequate to envisage the sun as a remote glowing sphere radiating into space at 6000° K. Actually, the coronal plasma (at a temperature of order one million degrees) spreads out over all of interplanetary space. The density of ionized gas in interplanetary space is everywhere greater than previously supposed. Photographic studies of the motion of comet tails indicate a continuous outpouring of coronal gas with velocities of order 500 to 1500 km/second. From these observations, it has been possible to estimate a plasma density at the orbit of earth of 500 ions per cubic centimeter, and it is expected that much higher densities occur during violent solar outbursts. Theories of whistling atmospherics also require densities of this same magnitude. Considerable additional evidence also supports the same conclusion.

This highly conductive wind can be expected to draw out the solar magnetic field radially. However, this wind cannot penetrate freely across the geomagnetic field. Calculations of the interaction energies indicate that an everyday solar wind may penetrate to about 25,000 km above the surface of the earth, while a strong solar wind is expected to penetrate to about 3500 km. The motion of this tenuous, ionized gas is controlled by electrical and magnetic forces which are themselves strongly perturbed by the motion of the gas itself. We can therefore expect this complicated electrodynamical interplay to define a magnetically erratic region which may properly be deemed the end of the earth's magnetic field. This region is of paramount importance to study experimentally since it is probably the source of those systems of currents and associated geomagnetic disturbances that bear a close relationship to the morphology of the aurora and, indeed, the entire atmosphere. Although the complicated cooperative plasma dynamics of this zone of interaction are yet to be worked out, some theoreticians appear to believe that conditions are favorable for accelerating charges to the high energies, 100 kev, observed in auroral arcs. One viewpoint concerning the recently discovered, trapped, high-energy particles, referred to as the Van Allen radiation belt, is that they too are the result of direct impact of the solar wind. To be sure, it has already been surmised that the auroral phenomenon may be a direct manifestation of instabilities in the radiation belt. However, the extent to which the aurora is under indirect solar control or is a manifestation of terrestrial forces (radiation belt) is not as yet ascertained. Moreover, no explanation has as yet been offered as to why it is a night-side phenomenon.

It should be noted that an alternative point of view for the origin of the inner radiation belt exists, that is, the neutron decay hypothesis. This theory assumes that neutrons, back-scattered by nuclear collision produced by cosmic ray impact with molecules in the atmosphere, decay into protons and electrons, some of which become magnetically trapped. Such an hypothesis does not, of course, require the interaction between the corona wind and the geomagnetic field. An understanding of how such magnetodynamic processes store energy and produce high-energy corpuscles in the solar-terrestrial realm may go a long way toward explaining the still unanswered questions concerning the primary mechanisms which produce and accelerate cosmic ray particles.

In addition to the corpuscular phenomenon, it is supposed that the solar-earth impact zone is a generator of a variety of electromagnetic, very low frequency (VLF) signals which have been observed. This noise propagates to earth approximately along magnetic field lines in the manner of lightning-generated whistlers. This VLF emission

* Manuscript received by the PGMIL, July 21, 1959. The Able-3 vehicle was launched on August 7, and has since been designated Explorer VI.

† Los Angeles, Calif.

appears to be strongly correlated with solar activity. For many, but not all, of these signals a recent theory suggests that the excitation mechanism is similar to the operation of a traveling-wave tube. That is, the electromagnetic noise is excited in the exosphere by streams of high-speed particles traveling along the magnetic field lines. This electromagnetic emission is a resonance effect which occurs when the velocity of the ionized stream is equal to the phase velocity of the electromagnetic wave. A model for most of the exosphere can be constructed in terms of this theory by detailed interpretation of several categories of received noises. This model requires that the ratio of electron density to magnetic field strength be nearly constant. Unfortunately, this theory, which is related to the ordinary Čerenkov theory, does not appear advanced enough to predict signal intensities which can be tested against observed signal strength. Moreover, there appear to be several categories of VLF emission which cannot be explained in terms of the traveling-wave tube mechanism. The Čerenkov mechanism is a distinct possibility as a source of VLF radiation. There is a large range of low frequencies for which the phase velocity of the extraordinary propagation mode is less than the speed of light by as much as a factor of one hundred. According to the Čerenkov theory, electrons, protons or any charged particle moving through the static plasma with velocities greater than the electromagnetic phase velocity ought to radiate, and the total energy of this radiation is proportional to the distance traveled by the charged stream as well as its density. It is the long mean free path for electrons and protons (approximately 10^{10} cm) which provides the opportunity for accumulating substantial signal strength. Moreover, unlike the applications in nuclear physics, Čerenkov emission is possible in the exosphere for nonrelativistic as well as relativistic particles, a range of velocities likely to be present in the Van Allen radiation belt. Reasonable estimates indicate that streams of high-energy electrons, or protons, could provide measurable VLF signals if the electrons were to contribute incoherently to the Čerenkov emission. More realistic estimates accounting for the very long wavelengths indicate that aggregates of electrons when bunched into sizes considerably smaller than the wavelength may contribute coherently rather than independently with the result that relatively large VLF signal intensities are expected. However, if the bunching in the high-energy streams extends over regions comparable or larger in size than the wavelength, no emission may occur in the sense that a steady current can produce no time-dependent polarization of the ambient medium. Consequently, the VLF signature bears a close relationship to the sizes of the electron aggregations in the high-energy streams and such bunching is clearly related to the injection mechanism by which such streams are created in the upper atmosphere.

Additional sources of VLF background are "bremstrahlung," the radiation produced by high-energy electron scatter from protons and the cyclotron radiation from the trapped Van Allen electrons. Estimates indicate that the latter mechanism is the more appreciable and that, now, coherent radiation of considerable intensity arises from bunches which are small in extent compared with the radii of their orbits rather than radiation wavelength while no radiation is expected for bunching sizes that are comparable to orbital radii.

It also appears that the signal strength should be considerably greater for ground reception, especially in polar areas where the strong geometric convergence factor effectively collects the radiation originating in a large area. This follows from the conservation of magnetic flux. It follows that the signal amplification on the ground would increase in proportion to the cube of the distance between the center of the earth and the excitation region. Conversely, it may be expected that VLF emission which is easily detected on the ground need not be as easily detected in a satellite. These geometric factors concerning signal amplification do not depend upon the particular VLF emission mechanism.

Again, regardless of the specific mechanism responsible for the VLF emission, there is the intriguing possibility that a trapping process exists which tends to contain and magnify the VLF energy in the exosphere. The containment process envisaged here is simply one of selective reflection, or partial reflection, produced by the gradients in the refractive index of the propagating mode, gradients which can look fairly abrupt in terms of the scale of wavelengths characterizing VLF radiation. Such "discontinuities" may occur upon approach toward the ionosphere from external regions. The increase in electron density as well as a corresponding increase in magnetic intensity produce the gradient in refractive index. It is known, for example, that whistlers do not always appear when there is a discharge of lightning. Thus, conditions for propagation appear to vary in a manner which is presumably unknown, and present knowledge cannot rule out the consequent possibility of the existence of a VLF "corona" on earth and perhaps upon other magnetized planets. The importance of investigating this new propagating medium in the upper atmosphere and, in particular, of identifying the emission process or processes cannot be overemphasized. If, for example, the VLF phenomenon were understood in terrestrial space, then VLF reception might prove valuable as an environmental probe of other planetary bodies. Apart from general scientific interest, there is the obvious possibility for a new means of long-range communication with low-power transmitters over natural, giant, magnetic propagation ducts.

As is usual when great gaps in understanding exist, the discussion is bold and inconclusive. Nevertheless, it furnishes valuable guidelines for an experimental space program. It indicates the necessity for a coherent measurement program throughout a relatively enormous region

of space extending over perhaps 1 to 7 earth radii. This region includes the solar wind-geomagnetic interaction zone, which is inaccessible to conventional sounding techniques except by man-made VLF signals. This region also contains the provocative Van Allen radiation belt. At the present time very little detail is known about the energy spectrum, composition, distribution in space, and temporal behavior of these "belts." Indeed, the most valuable and interesting aspects of the radiation belts will be their spatial symmetries or asymmetries and their fluctuations as a function of time.

At this point it is appropriate to enumerate a few of the principal lines of investigation of the Able-3 earth satellite. More specific description of the methods of investigation appear in later sections.

1) The satellite will be equipped with high and low energy cosmic ray detectors which will be operated continuously inside and outside the radiation belt. The instruments are a scintillation counter, Geiger counter, ionization chamber, and a proportional counter telescope.
2) The vehicle will be equipped to receive a VLF keyed signal at $15{,}500 \pm 50$ cps from a ground-based transmitter, and also measure the emission noise intensity in this same band. For the transmitted signal, the pulse travel time as well as the intensity will be measured.
3) The third and perhaps central set of measurements is of the two vital, dynamically associated "ambient" space parameters, electron concentration and magnetic vector. These will be measured continuously throughout the interaction zone identified above. The basic instrument to be used for these studies are a Doppler-difference frequency technique for electron density measurement, and a dual magnetometer system, employing a search coil magnetometer and a flux gate magnetometer which will determine the magnetic field vector.

It is to be noted that these experiments will be carried out over a highly elliptical orbit, for a nominal lifetime of a year, with an apogee in excess of 20,000 miles from the surface and with a perigee of 150 to 300 miles. Since the orbit is initially inclined at 45°, its precessional motion will permit measurements to be made over a more than adequate volume of the space about the earth.

Since the upper regions of space which we have been discussing are geomagnetically coupled with the ionosphere, it is essential to the understanding of either region that we attempt to correlate some of the effects of their interaction. To identify the pertinent areas of study, it is first necessary to distinguish the two regions, both of which are, of course, ionized and magnetic. There is no sharp demarcation between them, but the increase in neutral particle density in descent ultimately will define layers, the motion of which is no longer controlled by magnetohydrodynamic forces owing to the increased electronic collision frequency. Consequently, an interim region exists where the macroscopic plasma motion becomes gradually disentangled from the geomagnetic field. The rate at which this occurs is, of course, influenced by solar photo effects as well as electron recombination processes. As a result, a variety of distributed ionization irregularities as well as anisotropies associated with the geomagnetic field occur throughout this region, including a large but unknown part of the ionosphere. However, the disturbances through this important region can be revealed in depth by radio studies which utilize wavelengths that are small relative to the scale sizes of the irregularities. This affords a very important advantage not possible with VLF measurements in such media, namely that the theory of radio propagation is well established for such media. Thus, the natural tool for relating the ionosphere with the higher realms already under investigation in the Able-3 program is electromagnetic radiation at frequencies which will register the integrated coupling effects. To accomplish this merely requires that the satellite be tracked at those frequencies in an appropriate manner.

It is now desirable to convey a brief description of the motion of the ionosphere. The "undisturbed" ionosphere exhibits a wide variety of motions ranging from large-scale tides, to east-west drifts, to small-scale irregularities. No composite account of these motions can as yet be given, notwithstanding the existence of a great amount of pertinent but isolated data accumulated by radio observations of meteor trail configuration, auroral forms, and radio-star scintillation rate measurements. The latter have provided useful data on line-of-sight irregularities as well as information concerning the drift motion of these irregularities, sometimes reffered to as blobs. It has also revealed puzzling phenomena such as the night-side maximum in scintillation amplitude, and the night-side phenomenon of spread F. However, these manifestations may only be superficial consequences of larger geomagnetic systematics perhaps involving the highly energized radiation belt. As previously mentioned, the aurora is also a "puzzling" night-side phenomenon.

To gather useful data concerning these complex motions in the ionosphere, it is therefore important to include line-of-sight scintillation rate measurements for studies of ion cloud drifts and ionospheric irregularities simultaneously with the measurements made in the upper atmosphere. This is easily accomplished as part of the Able-3 program merely by tracking the telemetry beacon already on the vehicle.

It is perhaps appropriate to elaborate further on the importance of measuring ionospheric fluctuation rates. The phase fluctuation imposed upon signals from distance sources produces frequency dependent angle-of-arrival errors, or source flicker. This introduces a natural limit to

tracking accuracy. Therefore, a thoroughgoing knowledge concerning expected phase and amplitude signal fluctuations for arbitrary line of sight is essential for the design and evaluation of long-range missiles and space vehicles. At the present time the data which are available are those accumulated by radio-star scintillation measurements. The data are inadequate in two important respects:

1) The statistics, although probably adequate for determining the variance of signal amplitude and direction of arrival, are inadequate for establishing confidence in the power spectrum. Since star signals are weak, the poor signal-to-noise ratio causes poor time resolution of the signals and this interferes with extracting an adequate power spectrum from the records. This problem would not arise in the case of the satellite source.
2) Little information is available concerning the effect of varying the distance between two antennas forming an interferometer. Such information is important for determining the scale, or size, of the irregularities of electron density in the ionosphere. The degree of anisotropy in this quantity is also important. For example, if it is elongated in the direction of the geomagnetic field, the region which would produce the major scintillation effect must be high enough so that collisions no longer dominate the motion of the ionized clouds, but rather magnetoelectrodynamic forces are determinate. The scale of electron density irregularities and the degree of isotropy can be easily measured by the addition of a mobile third receiver to an interferometer system, and such a unit has been included in the Able-3 research program. In addition, such an arrangement will allow the determination of drift motions in all directions.

The instrumentation for the scintillation rate measurement involves two 40-foot diameter radio telescopes on an east-west baseline and a portable Yagi antenna. The Able-3 108-mc beacon signals will be tracked while scintillations in phase and amplitude as a function of baseline orientation and antenna separation will be recorded.

Before discussing the remaining scientific experiments of the Able-3 program, it is important to underline the significance of those which have already been discussed. Clearly this group of experiments involves measurements of quantities that, according to available facts as well as theoretical inference, are dynamically interrelated rather than isolated. The basic data gathered from such a coherent set of experiments can be expected to be invaluable, especially when interpreted together with world-wide monitoring measurements that are continuously and independently being carried out. Although it is impossible to predict the exact use of these comprehensive measurements in terms of what new theoretical or practical advances can ensue, it is safe to say that this new and interrelated information will at least furnish a far more precise description of the important phenomena in the upper atmosphere and eliminate erroneous views. This aggregate of measurements certainly achieves the most coordinated simultaneity of observations in extraterrestrial space that has ever been attempted.

Space research in the future will undoubtedly require instruments capable of providing pictures of celestial objects. The measurement of radiation ranging from the ultraviolet through infrared wavelengths can provide important scientific data. It is particularly significant for solar system probes to the planets (or moon) because the data may be obtained from early missions, ones in which the vehicles do not make a soft landing.

With regard to this photo range, the planetary bodies may be divided into three groups: first, bodies with little or no atmosphere, for example, Mercury or the moon; second, bodies with an atmosphere which is at least partially transparent, for example, earth and Mars; third, bodies with an atmosphere which is opaque, for example, Venus.

Next, consider the measurements in more detail. Taking the moon as an illustration of the first class of bodies, one of the unsolved, but extremely important, problems is the determination of the structure and substance of the surface in local areas; for example, are such areas covered with dust or hard rock? A brightness scan of the surface giving reflection characteristics as a function of angle would help resolve this question. In addition, information on the appearance of the backside of the moon would help determine the origin of geophysical features of the lunar surface.

Useful measurements of bodies with partially transparent atmospheres such as the earth would include measurement of cloud cover, movement of cloud masses, narrow-band absorption measurements, and reflection characteristics of the surface at various wavelengths. The first two would be useful for predicting weather, the third for determining temperature structure and density of certain molecules in the upper atmosphere, and the first and fourth for determination of the albedo and the heat balance of the planet.

For the case of a planet with an opaque atmosphere, such as Venus, brightness scans across the top of the atmosphere would yield limb darkening data, which are useful in determining the temperature structure of the atmosphere. Depending upon the data obtained, it may also be possible to ascertain the particle sizes in the upper atmosphere, and also to determine whether or not they are molecules, vapor droplets, or dust particles. Local variations in these data may also help to estimate the amount of atmospheric circulation. In addition, energy measurements in or near a particular absorption band may be used to make quantitative estimates of the presence of certain atmospheric gases.

In view of the wide variety of future applications for photo sensors, such a device has been placed on the Able-3 vehicle. Because of the very stringent weight and volume

requirements, it is a relatively crude sensor. However, it does incorporate an automatic scanning system so that data will be obtained from the entire surface of the earth. Experience gained in the design and use of this system will be invaluable for the eventual development of proficiency in acquiring and transmitting high-resolution pictorial images from space vehicles.

Since the Able-3 studies are preparatory to future space probe programs, it was obvious that, quite apart from the considerable scientific interest attached to micrometeoritic data and which is discussed below, superior statistics as to their momentum flux are required for the practical purpose of evaluating their damage potential. Consequently, a micrometeoritic momentum spectrometer is included as an important part of the Able-3 program.

II. Radiation Experiments

A. Introduction

Three radiation experiments are carried in the Able-3 payload: a scintillation counter prepared at Space Technology Laboratories, Inc., a Geiger counter and ionization chamber combination designed and built at the University of Minnesota, and a proportional counter telescope conceived by scientists of the Enrico Fermi Institute of Nuclear Studies of the University of Chicago and designed and built at the Chicago Midway Laboratories, a division of the University's Laboratory for Applied Science.

The primary objective of these experiments is to study the intensity, composition, energy spectrum, extent, and time variation of the terrestrial radiation belts discovered as a result of experiments carried on the Explorer satellites and Pioneer space probes. Previous experiments have shown that there are two distinct regions or belts of radiation surrounding the earth. The inner belt contains a large number of highly energetic particles believed to be protons produced by the decay of neutrons created in the earth's atmosphere by the primary cosmic radiation. In addition, it is believed that the inner belt also contains large numbers of low-energy particles, probably electrons of a solar origin. These low-energy particles may be much more numerous than the high-energy ones. The particles in the outer radiation belt have much lower energies than those in the inner belt and are believed to be electrons of solar origin released during solar flares. It now appears that a large percentage of these electrons have energies well below 500 kev.

The Able-3 satellite passes through the radiation belt twice during each revolution. Due to the apsidal motion of the orbit, the vehicle will pass through nearly all of the belt between 45°N and 45°S latitude during its nominal one-year useful lifetime. Thus it will be possible to map nearly the complete radiation belt during this time. However, since the apsidal motion is slow, it will also be possible to study the time variations of the belt over both long and short periods.

B. Description of the Experiments

1) Scintillation Counter (STL): The scintillation counter is designed to measure the total flux of electrons of energy greater than 225 kev and protons of energy greater than 2 mev. The detector is a plastic cylinder 2.5 centimeters in diameter and 0.64 centimeter thick. Light pulses are detected with a Dumont 6467 photomultiplier. The detector is surrounded by 10 mg/cm^2 of aluminum. There is a 5-centimeter aluminum window in the side of the vehicle, also 10 mg/cm^2 thick. To decrease noise in the output, the scaling circuit is biased to accept pulses equivalent to an energy loss in the plastic of at least 200 kev. The aluminum window subtends a solid angle of about 0.5 steradian at the detector.

Data are recorded and transmitted in both analog and digital form. The output of the photomultiplier is amplified and then fed to a scaling circuit with a scaling factor of 2^{20}. The analog data transmitted consist of the output of the 2^8, 2^{14}, and 2^{20} scalers. These pulses are transmitted on the same channel and are distinguished by their amplitudes, which are respectively 12, 23, and 66 per cent of the maximum bandwidth. In low flux regions, the 2^8 scale output furnishes most of the usable data. As the counting rate increases, these pulses blend into nearly a straight line, but the 2^{14} scale pulses are still easily resolvable. In intense regions only the 2^{20} scale pulses are resolvable. Due to the approximately one microsecond resolving time of the detector and its associated circuitry, it is unlikely that the counting rates wil become high enough to make it impossible to resolve the 2^{20} scale pulses. The output of the 2^{20} scaler is transmitted as digital output.

2) Ionization Chamber—Geiger Counter (University of Minnesota): The University of Minnesota experiment uses two detectors, an ionization chamber and a Geiger counter. The ion chamber is of the integrating type developed by Neher and Millikan of California Institute of Technology, and recently used extensively on University of Minnesota balloon flights. It consists of a 3-inch sphere filled with argon gas to an absolute pressure of approximately 6 atmospheres. The ions are collected by a quartz rod, the upper end of which is coated with Aquadag. The conducting rod is charged to a positive potential of 270 volts by an 8-micron gold-coated quartz fiber mounted on a side arm. When the fiber is connected to the positive potential, it is attracted to the rod, charging the system to the full potential of 270 volts. The fiber is then repelled by the electrostatic charge of the system. As the central rod collects electrons formed by ionizing radiation in the argon gas of the chamber, its potential drops, and the fiber slowly moves back until it is close enough to be violently attracted by the image charge. The fiber then recharges the rod and the charging pulse actuates the external electronic circuit. Thus each pulse from the chamber represents the collection of approximately 10^{-11} coulomb of electricity. Data are recorded in both analog and digital form; the subcarrier frequency on the analog output is devi-

ated for every 32 ion chamber pulses, and, in addition, the digital output for very low rate measures the time between two pulses of the ion chamber by counting the impulses from a standard time source and storing them in the digital accumulator by means of electronic gates. For very high pulsing rates, for example in the earth's corona, the time between pulses is too short to store clock signals so every ion chamber pulse is fed directly to the digital accumulator. Ambiguities which may arise in intermediate regions can be resolved by comparison with the analog record.

The second detector used in this experiment is a small Halogen Geiger counter (Anton type 302). This detector has been previously used on the Pioneer III and IV space probes. The counting rate is recorded in digital and analog form. The analog data are recorded with scale factors of 2^8 and 2^{17} and transmitted continuously on the same channel as the ion chamber data. The three signals are distinguished by their amplitudes. The digital data are handled in the same manner as the digital output of the ion chamber except that a scale factor of 2^{10} is used. The ambiguity in the counting rate in high flux regions introduced by deadtime effects is resolved by the ion chamber since in high flux regions the ionization is high.

Neither the ion chamber nor the Geiger counter has been deliberately shielded. The shields encountered by the incident radiation are the walls of the vehicle, an aluminum can surrounding the complete experiment, the walls of the detectors, and the other apparatus present in the vehicle. The minimum energy particles which can enter the detectors are about 1.25 mev electrons or 25 mev protons. Due to the different shielding in different directions, the geomagnetic factors of the detectors are functions of energy, measured during calibration experiments.

Preliminary results of the Pioneer III and IV space probes indicate a large variation in the outer radiation belt, believed to be the result of several solar storms which immediately preceded the paunch of Pioneer IV. The Able-3 vehicle will be in its orbit long enough so that it will be possible to correlate changes in the intensity of the radiation belts with solar activity. These changes could be due to changes in the amount of trapped radiation or to streams of charged particles from the sun passing in the vicinity of the vehicle but not necessarily being trapped in the terrestrial magnetic field.

The intensity of trapped radiation can be expected to vary with the magnetic field, and therefore the results of the radiation experiments will be correlated with the magnetic field measurements.

3) Proportional Counter Telescope (University of Chicago): About a year ago, it was decided to build an instrument which would measure high energy charged particles in the presence of strong bremstrahlung. The apparatus is composed of a triple coincidence counter system surrounded by 5 gm/cm^2 of lead. By making the counters operate in the semiproportional region, the deadtime of the counters was reduced to the order of one microsecond, and threefold coincidences due to charged cosmic ray particles can be readily measured even though the detector is situated in the low energy trapped radiation where bremstrahlung might produce a high counting rate in the individual counters. To avoid the problem of directionality while passing through the earth's field, the telescope was made essentially omnidirectional. The apparatus consists of seven cylindrical proportional counters, six in a concentric ring around the seventh, with the outer counters connected in two adjacent groups of three. The pulses from each group of counters are first amplified before entering the triple coincidence circuit. The pulse output of the triple coincidence circuit is recorded with binary scalers having a storage of 2^{11} to 2^{16} depending upon the particular flight requirements. The central counter, which forms the second counter of the triple coincidence, is also used independently to determine the single counter count rate for charged particles inside the lead shielding. Thus the single counter provides a measure of the bremstrahlung and is used as a monitor of this radiation, in addition to providing the single count rate needed for correction of accidentals at very high levels of flux. The output of the single counter is likewise fed to a scaling circuit. Both the single-counts scaler and the triple coincidence counts scaler feed their outputs into binary storage units provided by STL, which may then be read out upon command.

The minimum energy required to penetrate the triple coincidence counter with shielding is 70 mev for protons and 12 mev for electrons. Thus, only relativistic electrons will be measured as triple coincidence events and only protons in excess of 70 mev will be registered.

This detector system was used on the attempted lunar shot of November 8, 1958, in which the detector entered the lower edge of the Van Allen region near the equator. From the count rates in the triple coincidence detector it has been determined that near the lower edge of this zone the flux of energetic particles was approximately 400/cm^2-second and is composed of either protons above 70 mev or electrons about 12 mev. The evidence favors a proton component.

C. Supporting Experiments

In addition to the satellite-borne radiation experiments described above, an extensive program of supporting experiments is planned by the university groups. Both universities plan to continue their programs of balloon flights to monitor the cosmic ray intensity at the top of the atmosphere. The University of Chicago maintains a network of ground stations running northward from the equator which will continuously monitor the cosmic ray intensity throughout the period of satellite data acquisition. All participants have planned an extensive alert network to insure maximum data acquisition from the satellite during times of intense solar activity.

D. Objectives of the Experiments

Although each of these experiments is independent and complete in itself, the results cannot be completely evaluated

separately. Each measures the integrated flux of particles above its energy cut-off. However, due to the different shielding used, each has a different cut-off, as shown in Table I. Thus it should be possible to obtain a three-point intensity vs energy spectrum.

TABLE I

Experiment	Detection Threshold (mev)	
	Electrons	Protons
Scintillation Counter	0.225	2.0
Geiger Counter—Ionization Chamber	1.25	25
Proportional Counter—Telescope	12	70

Since the University of Minnesota experiment measures both ionization and counting rate with similarly shielded detectors, it is possible to compute the mean ionization per particle and thus obtain some indication of the composition and energy of the radiation.

The principal objectives of the University of Chicago and University of Minnesota experiments require measurements from space probes as proposed under the Able-4 program. The use of the same instrumentation on the Able-3 satellite serves three purposes: first, it is identical with the equipment to be carried in the Able-4 vehicles and therefore represents a checkout of the system for these shots. Secondly, there exists the possibility of simultaneous measurements from the Abe-3 and Able-4 instruments, which would provide information not possible from a single vehicle. Thirdly, the University of Chicago experiment provides a means for investigating the high-energy portion of the charged radiation trapped in the earth's magnetic field.

The experiments from the two universities cover two areas of physics: first, they are concerned with the solar production of charged particles of cosmic ray and lower energies and secondly, the University of Chicago experiment is designed to study the modulation of the extra solar cosmic ray particles by transient magnetic fields in the interplanetary medium. These measurements have a bearing upon the description of the solar-generated plasmas in the interplanetary medium.

1) Solar Production of Charged Particles: The second problem is the observation of transient intensity increases of nonrelativistic particles which may occur around the time of the solar activity maximum. Already several events have been reported which suggest that solar flares may produce low-energy particles in great numbers and that these particles are dominantly protons and alpha particles. These bursts from the sun are of considerable importance, not only for verifying the characteristics of the acceleration mechanism, but also for their use as probes to explore the magnetic fields in the intervening interplanetary space.

2) Magnetic Fields in Interplanetary Space—The Modulation of Cosmic Ray Intensity: It is now well established that over the period of a solar cycle the flux of relativistic particles that reaches the earth may be reduced by more than a factor of two at times of maximum solar activity. Aside from this 11-year cycle variation in which the intensity is reduced at the times of solar maximum, there exist sharp decreases of intensity that take place in the order of hours and usually represent somewhat smaller reductions of total intensity. There is good evidence indicating that these two phenomena represent the modulation of pre-existent cosmic rays—cosmic rays which come from the galaxy. We currently believe that the modulation takes place through disordered magnetic fields in interplanetary space. The questions now open relate to the location of these fields, their scale size, and whether the same fields account for both types of modulation effects (11-year and F-decreases). There is some evidence that the two mechanisms, although physically similar, involve phenomena of different sizes, namely, that the 11-year cycle requires the distribution of magnetic fields over the entire inner solar system, whereas the mechanism producing the Forbush-decreases may be more localized in the vicinity of the earth. A space probe in the interplanetary medium which shows that the cosmic radiation remains at the intensity observed near the earth would favor a large-scale modulation mechanism, whereas an observation showing that the intensity rises by factor two or more beyond the environment of earth would prove that the 11-year cycle effect is of local origin.

III. Whistler-Mode Experiment (Stanford University)

A form of VLF radio noise, usually having a pitch decreasing with time over a period of about one or two seconds, has been observed for decades. It has been established that such a noise signal, called a "whistler," is a pulse of VLF energy produced by a lighting stroke and propagated along the magnetic field lines from the source up through the ionosphere, reaching heights of several earth radii from the surface, and then guided by the magnetic field down through the ionosphere to reach the surface at a point (the conjugate point) lying on the same magnetic line of force as the source. The pulse may then be reflected from the ground to make a number of trips along the field lines between the source and the conjugate point. One essential requirement for the existence of this propagation mode, called the "whistler mode," is the presence of electrons having a density of several hundred per cubic centimeter at all points along the path. Thus the whistler mode is connected with both magnetic intensity and electron density in regions well above the main portion of the ionosphere.

A direct observation of naturally occurring whistlers from a satellite is subject to the disadvantage that the location of the source pulse is uncertain, and the identification of the ground-propagated pulse, if observed, is a matter of chance. Much of the information concerning natural whistlers as observed at ground stations is obtained from a study of their amplitude and frequency changes with time. To carry out similar observations from a satel-

lite requires a wide-band receiver and either wide-band telemetry (several kilocycles of bandwidth) or airborne processing equipment. The whistler-mode experiment for the Able-3 program is based on the observation of the whistler-mode propagation of coded signals transmitted from existing VLF transmitters. The transmission of such "artificial whistlers" between a 15.5-kc transmitter near Washington, D.C., and a receiver located at the southern tip of South America has already been demonstrated.

The airborne receiver for the Able-3 program is a tuned radio-frequency (TRF) receiver tuned to a frequency of 15.5 ± 0.05 kc. The receiver output amplitude modulates the appropriate telemetry channel. The transmitter is an existing unit transmitting keyed CW at a carrier frequency of 15.5 kc. A receiver bandwidth of 100 cps is used to give time resolution of approximately 10 milliseconds for measurement of group delay. The telemetered information is compared with the outputs of 15.5-kc receivers located at the STL tracking stations. Observations of the whistler-mode are also made from a Stanford University ground station at the point conjugate to the transmitter location, *i.e.*, from the southern tip of South America. Both the VLF airborne equipment and the VLF ground station equipment at the tracking stations have been provided by Stanford University.

A comparison of the time at which a code group is transmitted with the times at which it is received in the satellite and at the ground conjugate point makes it possible to determine the transmission times over two parts of the whistler-mode path. Such information is directly related to the average group velocity over the path, which in turn is dependent upon the electron-density distribution along the path. Also, in the course of the experiment, the amplitude of the received waveform is included in the telemetered information so that the experiment provides information concerning the attenuation of signals propagated via the whistler mode. The antenna used with the airborne receiver is the vehicle telemetry antenna to which the VLF receiver is multiplexed.

When the digital telemetry is operating, the payload becomes a phase-preserving receiver that permits measurement of phase velocity. Since the calibration includes measurement of antenna capacitance, some information pertaining to the dielectric constant of the medium may be possible.

This experiment on the propagation via the whistler mode is directly applicable to the interpretation of radiation and magnetic field data obtained by the other experiments. Any large-scale disturbance in the magnetic field structure of the earth due to magnetic storms is likely to exert an influence on the whistler-mode propagation. The experiment should also provide measurement of the physical size of propagation ducts for VLF signals, the coupling loss in propagating through the ionosphere, the magneto-ionic duct propagation cutoff in the region where the gyromagnetic frequency equals the signal frequency, and an over-all survey of VLF noise above the ionosphere.

The measurement of noise intensity is an important part of the VLF experiment. When analyzed in conjunction with the simultaneous data received from the corpuscular radiation, electron density, and magnetic field vector measurements, it may be possible to identify the mechanism which generates VLF energy.

IV. Electron Density Above the Ionosphere

A. Introduction

The determination of the contents of solar space has proved to be a puzzling and controversial problem, primarily for lack of good experimental data. The data on which to base an estimate of solar space electron densities are especially meager.

One could, for example, begin with data from the solar corona. Using polarization measurements and surface brightness of the K-corona, an interpolation formula for the electron density, $N(r)$, has been determined:

$$N(r) = 10^8(3r^{-16} + \tfrac{3}{2}r^{-6} + \tfrac{3}{2}r^{-3/2})$$

where $N(r)$ is electrons/cm^3 and r is in solar radii. This equation holds only in the plane of the solar equator and only to the vicinity of the orbit of Mercury, since presumably the solar corona should terminate there. However, by extrapolating r to the earth's orbit even though one should not expect continuity between the corona proper and the interplanetary gas, a value for the electron density of $N \approx 500$ cm^{-3} is obtained. This procedure, of course, is speculative since we are extrapolating over a range of r of nearly a hundredfold, and there is no theoretical reason for believing that N should be a function of r at this distance. Nevertheless, this result is approximately the same as results obtained by other means.

Another effect which gives a measure of the electron density above the ionosphere is atmospheric whistlers (Section III). Theoretically, to support this type of propagation requires a minimum electron density of about 500 cm^{-3} at the crest of the propagation path. Since whistlers have been observed where propagation paths apparently extend out many earth radii, electron densities of at least 500 cm^{-3} presumably exist in interplanetary space close to the earth's orbit.

Using Doppler measurements with very high altitude missiles and satellites, observers have obtained measurements of electron densities several hundred kilometers above the maximum of the ionosphere. The data indicate that the electron density decreases much more slowly beyond the maximum than it increases below the maximum. Using satellite data and extrapolating the model, $N \approx N_{\max}C^{-Mr}$, Russian experimeners[1] find that the number of electrons above the ionosphere maximum is about 3.6 times that below the maximum (a result consistent with Faraday

[1] I. L. Al'pert, F. F. Dobriakova, E. F. Chudesenko, and B. S. Shapiro, "Electrons concentrated in the upper ionosphere as determined from radio signals of the first earth satellite," *Doklady Akad. Nauk. SSSR*, vol. 120, pp. 743-746; 1958.

rotation experiments described below) and, that at altitudes of about 2000 to 3000 km, the electron density is on the order of 200 to 300 cm^{-3}. They also express the supposition that this is the altitude where the earth's atmosphere is continuous with interplanetary gas.

Faraday polarization rotation measurements have been made with radio echoes from the moon.[2] These results are in agreement with the missile and satellite measurements mentioned above; *i.e.*, there is apparently a very gradual tapering off of the earth's ionosphere; they show that about 75 per cent of the electron content between the earth and the moon lies beyond the ionospheric maximum.

Finally, the observed polarization of the zodiacal light has been interpreted as due to scattering of sunlight by electrons and dust particles in the neighborhood of the earth's orbit. Since light scattered by both electrons and dust particles will be polarized, it is extremely difficult to separate the two. Van de Hulst[3] estimates that if the polarization due to dust scattering were negligible, the electron density near the earth's orbit would be about 600 cm^{-3}. Taking into account polarization due to dust he obtains values of 200 cm^{-3} and 800 cm^{-3} under two extreme assumptions. Russian experimenters claim that, based on their measurements of zodiacal light over the Libyan desert, there is essentially no polarization due to interplanetary electrons. Their supposition is that the electrons in space near the earth's orbit are due to corpuscular radiation from the sun. Zodiacal light measurements should then be symmetrical about the plane of the solar equator and should vary in intensity in accordance with the sun's activity. Since they did not observe these effects, they conclude that sun-earth space is composed primarily of dust particles and has a negligible electron component. Blackwell argues, on the other hand, that the above results would tend to prove that there is a stationary interplanetary gas (electrons and protons) independent of the corpuscular radiation from the sun.

B. Doppler Difference Frequency Measurement

The method used to determine the electron density above the ionosphere for Able-3 is similar to that employed by Seddon[4] for electron density measurements in the ionosphere. It is based upon measuring the difference between two Doppler frequencies transmitted from the satellite. A CW signal transmitted from the ground at a frequency of $f_o = 401.8$ mc is multiplied in the satellite by two factors p' and q' and these two coherent signals, f_1 and f_2, are then retransmitted to the ground. The two multiplication factors are $p' = p' = 16/17$ and $q' = pq$, where $q = 2/7$. Hence, the two frequencies transmitted from the satellite are $f_1 = f_o p = 378.2$ mc and $f_2 = f_o pq = 108.06$ mc.

The frequencies of the two received signals at the ground tracking station are then essentially

$$R_1 = (f_0 - \Delta f_0)p - \Delta f_1, \tag{1}$$

$$R_2 = (f_0 - \Delta f_0)pq - \Delta f_2 \tag{2}$$

where Δf_o, Δf_1, and Δf_2 are the three Doppler frequencies. The Doppler frequency Δf_o is

$$\Delta f_0 = \frac{f_0}{c}\frac{d}{dt}\int_{S_0} n dS_0 = \frac{f_0}{c}\left[n_M \dot{S}_0 + \int_{S_0}\frac{\partial n_0}{\partial t}\, dS_0\right] \tag{3}$$

where the integration is taken along the ray path, S_o, from the ground station to the satellite. $\dot{S}_o$ is the component of the satellite velocity along the tangent to the ray path at the satellite, n_o is the index of refraction along the ray path, and n_M is the index of refraction at the satellite. At these high frequencies the index of refraction may be approximated by

$$n \cong 1 - \frac{KN}{f_0^2} \tag{4}$$

where N is the electron density in m^{-3}, $K = 40$, and f_o is given in cps. Using this approximation, the Doppler frequency Δf_o becomes

$$\Delta f_0 = \frac{f_0}{c}\dot{S}_0 - \frac{K}{f_0 c}\left[N_M \dot{S}_0 + \int_{S_0}\frac{\partial N}{\partial t}\, dS_0\right]. \tag{5}$$

Similar expressions hold essentially for Δf_1 and Δf_2. However, the ray paths S_o, S_1, and S_2 and the tangential components of the satellite velocity $\dot{S}_o$, $\dot{S}_1$, $\dot{S}_2$ differ because the index or refraction is slightly different for the three frequencies transmitted. At the high frequencies being considered here, the ray paths are sufficiently close that we may to a very good approximation use $S_o = S_1 = S_2$ and $\dot{S}_o = \dot{S}_1 = \dot{S}_2$. With this approximation, the two received signals [(1) and (2)] become (after R_2 is multiplied by $1/q$):

$$R_1 = f_0 p - \Delta f_0 p - \Delta f_1$$
$$= pf_0 - \frac{2f_0 \dot{S} p}{c} + \frac{Kp}{f_0 c}\left[N_M S + E\right]\left(1 + \frac{1}{p^2}\right) \tag{6}$$

$$\frac{R_2}{q} = f_0 p - \Delta f_0 p - \frac{\Delta f_2}{q}$$
$$= pf_0 - \frac{2f_0 \dot{S} p}{c} + \frac{Kp}{f_0 c}\left[N_M \dot{S} + E\right]\left(1 + \frac{1}{p^2 q^2}\right) \tag{7}$$

where

$$E = \int_S \frac{\partial N}{\partial t}\, dS. \tag{8}$$

Hence, we have a system of two equations with two unknowns. $\dot{S}$ and $(N_M + E/\dot{S})$, where $E/\dot{S}$ is to be considered

[2] J. V. Evans, "The electron content of the ionosphere," *J. Atmos. & Terrest. Phys.*, vol. 11, pp. 259-271; 1957.
[3] H. C. Van de Hulst, "Vistas in Astronomy," London, Eng., vol. 2; 1956.
[4] J. C. Seddon, "Propagation measurements in the ionosphere with the aid of rockets," *J. Geophys. Res.*, vol. 58, pp. 323-335; September, 1953.

an error term. Solving (6) and (7) for the electron density, N_M, yields

$$N_M = \frac{f_0^2}{K}\left[\frac{W}{W\left(1+\frac{1}{p^2}\right)+U\left(\frac{1}{p^2q^2}-\frac{1}{p^2}\right)}\right]-\frac{E}{\dot{S}} \quad (9)$$

where the two measured quantities are the difference between the Doppler frequencies.

$$W = \frac{R_2}{q} - R_1 = \Delta f_1 - \frac{\Delta f_2}{q} \quad (10)$$

and the Doppler frequency at 378.2 mc,

$$U = pf_0 - R_1 = p\Delta f_0 - \Delta f_1. \quad (11)$$

It is not necessary to measure the Doppler frequency U since it can be computed from trajectory data. However, measuring U is slightly more accurate and makes the system completely self-contained. The error term $(E/\dot{S})$ is a fictitious electron content along the ray path. It is shown in the next section that at certain times this term can introduce a significant error in the electron density measurement. To help us correct for this, we are making a Faraday polarization rotation measurement simultaneously with the Doppler measurement.

The values of the parameters entering into (9) depend upon the frequencies being used, the electron densities expected, and the orbit of the satellite. From nominal trajectory data, estimates can be obtained on the minimum and maximum range rates $(\dot{S})$ which will prevail while making electron density measurements. These rates will vary from a minimum of about 10^3 feet per second to a maximum of about 3×10^4 feet per second. As noted above, the best available evidence indicates that the electron density will vary from a maximum of about 10^6 cm^{-3} near perigee (200 miles) to densities of about 10^3 cm^{-3} at altitudes greater than a few thousand miles, although the minimum density is extremely uncertain since the available evidence is meager. The Doppler frequency shifts corresponding to the range rates being considered are, for a 400-mc signal, about 8×10^2 cps at minimum range rates and about 2×10^4 cps at maximum range rates. For this experiment, the most critical parameter is the difference between the two Doppler frequency shifts, W (10). For minimum range rates and an electron density of 10^3 cm^{-3}, the minimum Doppler difference, W, is about 10^{-3} cps. It is the value for W under conditions of solar space where electron densities are low, range rates are low, but where measurement times can be long.

The ground equipment used to measure the Doppler frequency difference is quite simple. It is designed to work with two Able-3 Microlock receivers at 378 and 108 mc. The inputs to the equipment are the VCO outputs which contain the Doppler frequencies from the receivers. After suitable multiplication and mixing, the difference in phase between these two signals is measured and recorded on a Sanborn chart. This gives W. A separate measurement of the Doppler frequency U at 378 mc is made and recorded. (The range rate, $\dot{S}$, is also known from trajectory data.) With these two quantities known, the electron density can be computed from (9).

C. Faraday Rotation Measurement

The error term $(E/\dot{S})$ entering (9) is due to the time change of the electron content along the radio path from the satellite to the tracking station. The change in electron content is caused by changes in the sun's ionizing radiation during every 24-hour period due to the earth's rotation, and to ionospheric scintillation caused by the drift of electron patches across the propagation path. Since the satellite is many thousands of miles from the tracking station during electron density measurements, its angular position with respect to the earth changes by only a few degrees during the time of measurement, and the propagation path through the ionosphere is essentially constant. The effect of the growth and decay of the electron content can be estimated from Faraday polarization rotation measurements of moon echoes. These show that during major portions of every 24-hour period, a fictitious electron density on the order of 10^3 cm^{-3} can be introduced. This is approximately the same as the expected electron density in solar space. During other parts of the day, especially just before dawn when the ionosphere is relatively unchanging, the error term is negligible.

An indication of the error introduced by ionospheric scintillation can be deduced from radio star scintillation measurements. These data are still quite sketchy, but indications are again that ionospheric scintillation can introduce a fictitious electron density comparable with the expected actual density. However, the scintillation phase fluctuations presumably have a mean of zero; *i.e.*, sometimes they add and other times subtract a fictitious electron density. Consequently, over a long enough measurement time, this error can be "averaged" out.

To obtain further quantitative data on this error term and thus correct the electron density measurements, the time rate of change of the Faraday polarization rotation is made at 108 mc simultaneously with Doppler difference measurements. At this high frequency, the Faraday polarization rotation angle for quasi-longitudinal propagation is

$$\phi = \frac{2.3 \times 10^4}{f^2}\int_S H \cos\theta N ds \quad (12)$$

where H is the earth's magnetic field in gauss along the path and θ is the angle between the direction of propagation and the magnetic field. At the great distances that electron densities are measured, the time rate of change of the Faraday rotation is approximately (the term due to

satellite motion is negligible at great distances)

$$\phi = \frac{2.3 \times 10^4}{f^2} (\overline{H \cos \theta}) \int_s \frac{\partial N}{\partial t} ds \qquad (13)$$

where $(\overline{H \cos \theta})$ is a suitable average of this quantity through the ionosphere. This gives a measure of the error term (E/S), contained in (9). The rotation, ϕ, is measured both manually and by recording the phase difference of the two circularly polarized components of the 108-mc signal from the satellite.

V. Search-Coil and Flux-Gate Magnetometers

The magnetic field of the earth is usually represented by a model consisting of an eccentric dipole plus higher order multipoles. Up to the present time, the data used in the establishment of this model have been obtained from surface measurements and a few isolated rocket measurements. More recently, the extraterrestrial magnetic field has been sampled by the Pioneer I space probe, the telemetered data from which have indicated departures from the rate of variation to be expected from a spherical harmonics expansion of the surface measurements. These departures originate in extraterrestrial phenomena, such as the controversial ring current, or the magnetic field of the solar corona.

A satellite is inherently well adapted to map the earth's magnetic field at high altitudes. A measurement of the vector magnetic field from a high-altitude satellite has the advantage of being unaffected by local surface anomalies on the earth. In addition to the mapping of the steady-state magnetic field, the field observations from the Able-3 vehicle permit the direct investigation of the ring current, of transient phenomena such as auroral current, and of various hydromagnetic effects.

One such hydromagnetic effect is the hypothesized propagation of hydromagnetic waves along magnetic field lines. Turbulence at the transition between the coronal wind and the geomagnetic field, or turbulence in the coronal wind itself, may provide a mechanism for the generation of such waves in the geomagnetic field. Such effects may have been observed in the Able-1 program. Although the effects of interest occurred at a distance of about 10 earth radii from the earth's center on the Pioneer I flight, magnetic conditions were exceptionally quiet on that day. On a magnetically disturbed day, the transition between the geomagnetic and solar magnetic fields is expected to occur at about 5 earth radii, thus making the effect observable from the Able-3 orbit, which has an expected apogee of about 7 radii. For several reasons, therefore, a continuous monitoring of the extraterrestrial geomagnetic field, during a period of time extended enough to include a variety of forms of solar activity, is of great fundamental value.

The two magnetometers carried in the vehicle operate on different principles. A search coil mounted near the periphery of the vehicle measures the component of the magnetic field perpendicular to the vehicle spin axis, and a flux gate also near the periphery, oriented parallel to the spin axis, measures the component of the magnetic field along this axis. By using the output of the television sensor to indicate the vehicle rotational position at the time of maximum search-coil output, the direction and magnitude of the component of the magnetic field normal to the vehicle spin axis is determined. This information, combined with the output of the flux-gate magnetometer, determines the magnitude and direction of the vector magnetic field provided that the orientation of the vehicle spin axis is known.

The search-coil magnetometer is similar to that used in the Able-1 program. Its sensing element consists of a mumetal core wound with 5000 turns of number 40 copper wire. The output of the coil is coupled to a transistorized amplifier tuned to the nominal spin rate of the vehicle. In a steady magnetic field, the amplifier output is a sinusoid at a frequency equal to the spin rate. This output is applied to a subcarrier oscillator to modulate a telemetry channel. In the Able-1 program, the greatest possible sensitivity and dynamic range were desired. To attain this objective, a very large amount of AGC feedback was employed in the amplifier to extend the dynamic range. Such extension was obtained at the expense of the high-frequency response of the system. In the Able-3 program, on the other hand, the amplifier is modified to reduce the dynamic range to a value of approximately 300 to 400. This reduced dynamic range provides precise measurements over a range from about 1 milligauss, the smallest expected field for the Able-3 orbit, up to 300 to 500 milligauss, the surface value of the geomagnetic field. The reduction in dynamic range results in an improvement in the transient response of the search-coil magnetometer.

The flux-gate magnetometer, purchased from the Schonstedt Engineering Company, has a high-frequency cutoff of about 10 cps and, as a consequence, relatively rapid changes in the magnetic field amplitude can be followed. The flux-gate magnetometer is, however, subject to dc drifts, and is temperature sensitive. The search-coil magnetometer, on the other hand, being an ac device, is essentially independent of temperature and other causes of drift.

In addition to providing a complete description of the vector magnetic field, the two devices complement one another in other respects. In particular, the flux-gate magnetometer, and thus the flux-gate output, is more useful in the study of rapid transient variations in the magnetic field. On the other hand, the insensitivity of the search-coil magnetometer to drifts makes it the better device for the observation of possible secular variations.

Although neither the flux-gate nor the search-coil magnetometer possesses the accuracy offered by the proton precession magnetometer, the search-coil and flux-gate magnetometers each measure the magnetic field continuously, while the proton precession magnetometer samples

at intervals of about 10 seconds. Furthermore, the power requirements for the proton magnetometer are severe. Since hydromagnetic phenomena constitute a very important class of magnetic phenomena, a continuously-reading magnetometer is of the greatest utility.

VI. Radio Scintillation Experiment[5]

The object of the radio scintillation experiment is to gain information about the size, shape, orientation, motions, and stability of ionospheric irregularities which cause amplitude and phase scintillations in radio waves. Almost all information has been derived from measurements in the field of radio astronomy using radio stars as sources, which have input signal-to-noise ratios of approximately 13 db. Therefore, the expected signal-to-noise ratios of order 25 to 30 db offered an excellent opportunity for studying the important physical parameters of the ionospheric irregularities.

A. Equipment

The two 40-foot diameter radio telescopes on the present 1500-foot east-west base line at Table Mesa, Colo., are used as the two elements of the phase-lock, phase-sweep interferometer system. Two STL receivers of the phase-lock type are used. Each receiver consists of four superheterodyne stages. The first, second, and fourth stage local oscillators of the two receivers are locked together, with the first receiver phase-locked to the incoming signal. The third stage local oscillators will be maintainend 1000 cps apart by means of a 1000-cps local oscillator, so that the RF phase difference of the incoming signals at the two antennas show up as phase modulation on a 1000-cps carrier. It is for this reason that the term "phase-sweep" is applied to the detection scheme. The bandwidth of this 1000-cps signal is 100 cps. This 1000-cps signal is phase-compared with the 1000-cps oscillator to obtain the desired angular scintillations out to 100 cps. The amplitude of the 1000-cps signal is also continuously recorded to obtain a continuous record of the signal power received by the system.

As explained below, two such phase-lock, phase-sweep interferometers permit simultaneous observations over various baseline lengths and orientations. The second unit utilizes one of the 40-foot paraboloids and a portable Yagi antenna, but otherwise is identical to that described above.

B. Expected Signal-to-Noise Ratio

The signal-to-noise ratio to be expected at the input of a single paraboloid receiver system of appropriate polarization is given by

$$\left(\frac{S}{N}\right)_{\text{in}} = P\left(\frac{1}{4\pi R^2}\right)(N\pi r^2)\left(\frac{1}{kT_e B_{\text{in}}}\right)$$

where P is the effective transmitted power, the second term is the space transmission loss factor, the third is the effective area of the paraboloid of radius, r, and the last term is the effective noise power (receiver plus sky noise) in the input bandwidth, B_{in}.

At the output of the receiver, the signal-to-noise ratio of such a system is

$$\left(\frac{S}{N}\right)_{\text{out}} \cong \left(\frac{S}{N}\right)_{\text{in}}\left(\frac{B_{\text{in}}}{B_{\text{out}}}\right)^{1/2}.$$

If two such antenna-receiver systems are coupled to form a phase-sweep interferometer whose input and output bandwidths are both equal to B, the signal-to-noise ratio at the output is

$$\left(\frac{S}{N}\right)_{\text{out}} \cong \left(\frac{S}{N}\right)_{\text{in}} \cdot \frac{2}{\pi}.$$

In this experiment, the radiated signal is linearly polarized. To avoid periods of loss of signal due to Faraday rotation, circularly polarized antennas will be used, with a resultant loss of receiving efficiency of a factor of two. Thus

$$\left(\frac{S}{N}\right)_{\text{out}} \cong \left(\frac{S}{N}\right)_{\text{in}} \cdot \frac{1}{\pi}. \tag{14}$$

The signal-to-noise ratio on the proposed phase-sweep interferometer system is therefore a factor $\pi(\cong 5$ db) worse than that obtained by a single-antenna, total-power system of correct linear polarization. This loss of signal-to-noise ratio is, however, more than compensated for by the improved stability of the phase-sweep system, whose output is relatively insensitive to variations in sky noise, receiver noise, or receiver gain.

Substituting $P = 500$ mw, $R = 36 \times 10^6$ meters (apogee), $N\pi R^2 = 60\,\text{m}^2$, $T_e = 1000°\text{K}$, $B = 100$ cps in (14), we obtain an output signal-to-noise ratio of approximately 26 db. This compares with an output signal-to-noise ratio of about 14 db for the Cygnus source when using the same antennas in a phase-sweep interferometer system at an output bandwidth of 0.5 cps.

C. Use of Portable Yagi Antenna

In the case of where the effective spacing, D, of the antennas of an interferometer is small compared with the 0.5 correlation distance in the incident diffraction pattern of radio energy, one can assume that the phase gradient is uniform between the two antennas. Under such circumstances, the rms angular scintillation observed on a single antenna is given by

$$\theta_{\text{rms}} = \Phi_{\text{rms}} \cdot \frac{\lambda}{2\pi D} \tag{15}$$

[5] This experiment is part of a continuing BMD-STL weapon systems effort.

where Φ_{rms} is the root mean square value of the irregular deviations in relative phase of the signal at the two antennas.

In the case where the amplitude and phase scintillation are *not* well correlated at the two antennas, the actual irregular angular deviation of the incident wave front would be significantly greater than that predicted by (15).

While it is probable that (15) can be used on the present radio-star data without great error, any search for high-speed scintillations, implying structure that is small compared with 1500 feet, means that (15) cannot be used. To overcome this difficulty (by actually determining the scale of the structure in the diffraction pattern), measurements are made at various antenna *separations,* using a simple portable Yagi antenna and one of the 40-foot paraboloids as the two elements of an interferometer. Since there is high probability that the scale of the diffraction pattern across the ground is a function of direction, observations are being made with variable *orientation* of baseline, as well as with variable baseline length. (For example, such observations could, under certain circumstances, permit the simultaneous measurement of the angular scintillations in azimuth and in elevation.)

The signal-to-noise ratio of the Yagi-paraboloid combination is some 4 db worse than for the two-paraboloid interferometer; if necessary, this deterioration in signal-to-noise ratio can be overcome by using a narrower tracking bandwidth ($\backsim$ 25 cps).

D. Expected Capabilities of System

1) Measurements of Relative Phase:

a) Effect of finite signal-to-noise ratio: The expected signal-to-noise ratio of about 26 db (400:1) at apogee results in an rms phase jitter of approximately 1/400 radian or 0.2° or relative phase, for an input-output bandwith of 100 cps.

b) Phase stability of electronics: Brief tests with the electronics of the existing ratio-star interferometers suggest that the minute-to-minute relative phase stability of the electronics is significantly better than 0.2°, and therefore is not a limiting factor.

c) Stability of electrical centers of paraboloids: The phase-centers of the dishes vary irregularly by one or two orders of magnitude more than 0.2° under extreme wind conditions. Only during calm conditions is it likely that phase stabilities of 0.2° are possible; a median value is probably about 1.0°.

d) Tropospheric limitations: Discussions with Dr. M. C. Thompson of CRPL suggest that at low angles of elevation ($< 10°$) the median relative rms phase shift due to the troposphere is of the order 0.1°. At higher elevation angles the effect should be less.

e) Frequency stability of system: In general, the satellite signals at the point where they mix will have traveled several wavelengths further via one antenna than via the effects upon the relative phase of the signals; however, for a 10-wavelength difference, the relative phase would change by less than 0.1° provided the stability of transmitter was better than 1 part in 3.6×10^4 (say 3 in 10^5). Minute-to-minute frequency stability of this order is available.

f) Conclusions: While under typical conditions the relative phase measurements are limited by mechanical distortion of the paraboloids due to fluctuating wind loading, under very favorable conditions it should be possible to reach a sensitivity of 0.2° rms phase shift. For large-scale irregularities, this corresponds to a rms angular glint of about 0.4 second of arc.

2) Measurement of Amplitude Scintillations:

a) Effect of finite signal-to-noise ratio: The expected signal-to-noise ratio at apogee is 26 db for a 100-cps input-output bandwidth. This implies that the limiting sensitivity to amplitude scintillations (without additional integration) is 1 part in 400 ($\cong$ 0.01 db).

b) Effect of fluctuations in receiver gain: While minute-to-minute rms stability of the order 0.01 db can be obtained on sensitive radio astronomy equipment, it is by no means certain that this can be achieved using the proposed phase-lock, phase-sweep interferometer system. However, it is possible that a figure of 0.03 db rms (0.6 per cent) can be obtained.

c) Effect of satellite rotation: Satellite rotation can introduce changes in received signal by varying the polarization and/or the power radiated towards the receivers. The former effect is minimized by the use of circularly polarized feeds; the effect of the latter depends upon the axis of rotation of the satellite relative to the axis of the dipole antenna. Any effect of satellite rotation should be periodic in nature, and can therefore (to a first order) be allowed for.

d) Conclusion: Given adequate stability of the effective transmitted power, it should be possible to measure the moment-to-moment fluctuations in received signal strength to a limiting sensitivity of about 0.03 db.

VII. Image Transmission System

The present knowledge of the solar spectrum, together with the photo response characteristics of an image scanning device, allows for the determination of reflection characteristics of planetary or lunar surface. These data, accumulated over a broad band ranging from the infrared through the vacuum ultraviolet, can reveal information concerning the composition of planetary atmospheres, cloud cover, and general physical characteristics of the surface. There an image transmission system capable of operating under the weight, power, and bandwidth limitations of the Able-3 vehicle has been included in these payloads.

The optical unit is a Newtonian telescope incorporating a General Transistor Corporation type 2N469 phototransistor mounted behind a stop with a pinhole aperture. The

plane of the stop is located at the focus of a two-inch aperture spherical mirror which looks out through a hole in the payload shell. The output voltage of the phototransistor is amplified, stretched in time, and telemetered in analog form to the ground stations. The transmitted output is a quantized function of the phototransistor output giving eight possible brightness levels.

The 2N469 phototransistor is sensitive to wavelengths between 2000 and 17,000 A. Its response peak is in the 8000 and 16,000 A region and consequently is primarily a near-infrared detector.

The angular field of view of the instrument is 0.5°. Unless a portion of a planet lies within the field of view, the output signal of the phototransistor is zero.

The spin axis of the vehicle is roughly in the plane of its orbit. Therefore, it is possible to make use of the orbital motion and the vehicle spin to obtain a two-dimensional scan of the brightness of a planetary disk. When a planet lies within the line of sight of the system, a strip of the planetary disk of 0.5° angular width is scanned by the system. The brightness of this disk is measured by the voltage output of the phototransistor as it scans the disk. The system is designed to telemeter this voltage output pattern to a ground station, where the original intensity pattern can then be reproduced.

Due to limitations introduced by the narrow information bandwidth available for telemetered data, it is impossible to transmit the intensity pattern from a complete scan during a single spin cycle of the vehicle. Therefore, it is necessary to rescan the same area many times and measure and telemeter one portion of the information during each spin cycle.

In practice each scan line is divided into 62 spots of 0.5° angular diameter. The scan line starts at the limb of the planet and covers 31° of the spin motion of the vehicle. No data are transmitted until the system first sees the limb of the planet. Then the brightness of the first spot of the scan line is measured and transmitted during the remainder of the spin cycle. Each time the limb of the planet comes into view, a timer is started which selects the portion of the scan line whose intensity is to be measured. For example, on the tenth spin revolution after the planet has come into view the timer instructs the system to wait until the vehicle rotates through $9 \times 0.5°$ or 4.5° after seeing the limb of the planet before measuring and transmitting the brightness. The timer is then advanced and the process repeated for 62 spin revolutions. Then the timer is reset to zero and for two spin revolutions, a sync signal is transmitted to show that this has been done. Thus, it takes a total of 64 spin revolutions to scan a single scan line.

During the time required to scan one line, the orbital motion of the vehicle changes the portion of the planet in the field of view of the image transmission system. Thus, when the scan of a single line is completed the next strip of the disk scanned is shifted slightly from the original strip. In addition, the first strip is inclined at an angle since all the intensity points are measured at different times. Thus, it is seen that the reproduced image consists of a series of strips. each of which covers a portion of the disk of the planet. Since each strip has the same angular length, they may include only a portion of the planetary disk or extend beyond it.

Under ideal conditions these strips are exactly adjacent, but for a satellite moving in an elliptic orbit about a planet, it is impossible to obtain a scan of the planetary surface in which all scan lines are exactly adjacent. In the case of the Able-3 vehicle, the image transmission system is oriented in such a way that the gaps and overlaps are never greater than half a scan line width. The scan lines will always cover the complete disk of the planet. The overlap of gap between lines can be calculated from the orbital parameters of the actual satellite orbit and may be taken into account when reducing the data.

The nominal spin rate of the vehicles is 2.8 rps. At this spin rate, there is no overlap between 62 spots of a single scan line. However, if the spin rate is slower or faster than this nominal value, there will be overlap or gaps, respectively. If the vehicle precesses, the scan lines will be greatly distorted. This would lead to a major data reduction problem in attempting to reconstruct the image of the planetary disk. A mercury damper ring is installed in the payload to minimize precessional motion.

VIII. Micrometeorite Momentum Spectrometer

Visual and radio observations of sporadic meteor trails in the earth's atmosphere have established the presence in space of small grains of matter ranging in size from a few grams down to the order of 10^{-5} gram. The results of many measurements have indicated that the density of these grains in space is approximately inversely proportional to their mass; that is, in any volume of space the average total mass of particles of a given size is the same for all sizes of grains. It is not known, however, whether this empirical law can be extended to dust particles whose masses are much smaller than 10^{-5} gram since such minute particles produce insufficient ionization in the atmosphere to be studied by radio or optical means.

It is of considerable interest to determine the properties of the micrometeoritic material, not only to extrapolate the mass distribution to the millimicrogram region but to provide a more substantial basis of fact for theoretical interpretation of other, related, astrophysical phenomena. There are considerable data available as a result of many precise astronomical observations which depend for their interpretation on assumptions regarding the nature of the interplanetary and interstellar medium, assumptions which are further reflected in the form of theories of galactic structure and evolution. Clearly, direct measurements of the physical properties of the interplanetary dust particles will be scientifically invaluable.

Although a complete set of measurements (charge, mass, velocity, composition, magnetic moment, etc.) is precluded by present payload restrictions, an initial step in such a study has already been made with the successful operation of the micrometeoritic spectrometer in the Able-1 program, and will be continued with the Able-3 flight. The relatively low density of the micrometeorite population requires a long sampling time in order to make statistically reliable conclusions concerning the interplanetary medium. In this respect, Able-3 should provide considerably more valuable data than did Able-1. Furthermore, because of the long observation time available, one can reasonably expect to obtain information on the spatial and temporal distribution of micrometeorites of both high and low momentum, indicating whether the particles in each momentum range are uniformly distributed or occur predominantly in localized regions of space and whether or not fluctuations in the density of particles are correlated with the occurrence of meteor showers as observed on the earth. Moreover, if an enhanced flux can be correlated with sporadic E layer ionization, this will furnish valuable information concerning cosmic dust as a mechanism for ion production in the E region.

This experiment, performed under the direction of the Air Force Cambridge Research Center, separates the micrometeorite flux into high and low momentum components in a simple way by having two levels of sensitivity of the detector. A particle striking the diaphragm of the spectrometer will transfer its entire momentum inelastically to the diaphragm, and the 100-kc component of the resulting impulse is picked up by a microphone containing a piezoelectric crystal which rings at this frequency; the pulse is then amplified and the envelope detected. A two-way channel (corresponding to two momentum thresholds) pulse height analyzer classifies the pulse according to whether it was produced by a low momentum ($> \backsim 5 \times 10^{-4}$ gm-cm/second) or a high momentum ($> \backsim 5 \times 10^{-3}$ gm-cm/second) particle. The spectrometer has been calibrated with both low-velocity and high-velocity grains; however, since the highest velocity of the calibration particles obtainable in the laboratory (4 km/second) is considerably smaller than the probable velocities (11 to 70 km/second) of micrometeorites impacting on the satellite, the response of the detector to the momentum of actual micrometeorites is somewhat uncertain. The necessity of extrapolating the momentum calibration to high velocities together with the fact that the detector does not respond uniformly to particles striking at different points of the diaphragm results in an estimated uncertainty of at least a factor of three in the momentum measurement. Any inferences made about the masses of the micrometeorites will be subject to even larger errors since the velocities of the particles can only be estimated. In spite of the relatively large uncertainties expected in the measurements, the experiment remains sufficiently accurate to contribute significantly to our knowledge of the properties of micrometeorites.

Able-3 Payload Design*

JOHN E. TABER†

Summary—**This paper discusses the Able-3 payload instrumentation. The design parameters and functional characteristics of this instrumentation are discussed in terms of the two goals of this program: to build a payload which gathers as much scientific information as possible concerning the space environment about the earth, and to develop and check out communications, power supply, and temperature control systems suitable for subsequent interplanetary space probes. The basic electronics of the satellite and their relationship with the experimental equipment as well as with structural and other aspects of the satellite are discussed in some detail. Particular emphasis is placed on the communications system, and, in particular, on the new digital telemetry system and its value to deep space exploration.**

* Manuscript received by the PGMIL, July 21, 1959.
† Space Technology Labs., P.O. Box 95001, Los Angeles 45, Calif.

Introduction

BY THE TIME this paper appears in print, the Able-3 launch will have taken place, and other related vehicles will follow shortly. At the date of writing, the payload has been sufficiently well defined to warrant its description nearly two months before scheduled launch.

The Able-3 payload, an earth satellite in a highly elliptical orbit, has two purposes—that of studying the space environment about the earth, and that of providing a test vehicle to evaluate components and techniques developed for use in interplanetary space probes. The four-stage Able-3 vehicle consists of a Thor first stage, an Aerojet 10-101 second stage, an ABL 248 solid propellant spin-

stabilized third stage, and a spin-stabilized fourth stage or payload weighing about 140 pounds. The first three stages are used to place the payload in a large geocentric elliptical orbit whose apogee is about 20,000 nautical miles and whose perigee is about 150 nautical miles. A five-pound solid propellant injection rocket in the payload can be used, if necessary, to increase perigee and thereby increase the payload's lifetime.

Had the design of a Thor-Able launched payload been concerned solely with studying the space environment about the earth, it could have proceeded in a rather straightforward manner and, with the exception of the number and complexity of the experiments carried, would have incorporated many features found in payloads already orbiting the earth. An already developed FM-PM telemetry system would have been used, power supply design would have been conventional, and heat control could have been handled be proven techniques. The additional requirements that the payload serve as a "flying laboratory" for the evaluation of components and techniques useful in interplanetary space probes, however, has supplemented the usual design requirements with a new and unusual group of problems. Most of the new problems which arise can be associated either directly or indirectly with the need to transmit intelligence over multimillion miles, or with the severity and duration of both changing and static environmental conditions.

The range equation,

$$P_R = P_T \frac{G_T G_R \lambda^2}{(4\pi R)^2 L} \tag{1}$$

expresses the functional relationship between the power received on the ground and the power transmitted in the payload, the payload and ground antenna gains, the wavelength used, range, and losses due to polarization, diplexers and cables. A second equation,

$$P_N = k[T_s + T_0(n-1)]B, \tag{2}$$

expresses the noise that will be superimposed upon the received signal as a function of Boltzmann's constant, the temperature of outer space and at the receiver, the receiver's noise figure, and the bandwidth of the receiving system. The final relationships which complete the specification of the communication problem are the required signal-to-noise ratio at the receiving site as determined by the quality of data desired and the bandwidth needed as a function of the desired rate of information transmission. Moreover, this latter functional relationship varies with the degree of sophistication employed in choosing a modulation method.

Any attempt to substitute realistic values of the parameters into this system of equations quickly demonstrates that a conflict of interests exists. For instance, by choosing the largest ground antennas available (*i.e.*, the 250-foot radio telescope of the University of Manchester), the most sensitive receivers in existence today, a payload antenna gain consistent with the present state of the art, and a frequency which minimizes extraneous losses, it is apparent that only a few bits of information per second can be conveyed over interplanetary distances using a payload transmitter whose output power is as small as 100 watts. From this example two things become clear: first, the system designer must accept the need for a payload transmitter of relatively large power, together with its attendant power supply problems; and, second, any improvement in the modulation efficiency or in elimination of pretransmission redundancy will provide a better utilization of the limited transmission rate capability.

The high transmitted powers required, coupled with the duration of interplanetary flights, precludes the development of a payload whose power is derived solely from conventional batteries. Since the state of the development of atomic power supplies does not permit their serious consideration at this time, the payload designer must turn to solar cells as a necessary choice for the source of primary power. The solar cell configuration discussed later in this paper approaches the greatest solar cell surface area which could be accommodated. It is capable of delivering between 15 and 20 watts continuously to the payload.

Early in the initial system design a value of 150 watts of payload transmiter power was specified for use in interplanetary probes because on the one hand the largest transmitter and power supply which could be carried was limited to this value; and at the same time using existing techniques and components it was sufficient to provide reliable communications over distances up to 55 million miles. After taking into account the efficiency of the power amplifier and of the static converters needed to develop the high voltages required, it was found that a primary power supply capable of delivering peak powers of 500 watts would be required.

It is thus immediately clear that the transmitter must operate at a reduced duty cycle. This, in turn, implies that a power storage system capable of accumulating power over extended periods of time and discharging it at very high rates must be carried. The payload weight which is available for a storage battery determines the maximum storage capacity and therefore the maximum ON time for the transmitter.

The problem of how to obtain maximum information from the scientific experiments is a consideration which arises from the transmitter duty cycle limitations. Fortunately many of the data obtained are most meaningful in the form of events-per-unit-time. Micrometeorite impacts and radiation particle impingements are of this type. While it is desirable to keep the unit of time at some reasonably small value, information is obtained, though with greater smoothing, even when the unit of time is the several hours between successive transmissions. Hence there is a need for accumulating the number of events as they occur and later transmitting the total to the earth.

The information content explicit in analog data, however, is so great as to preclude its storage in the payload for later transmission. Therefore experimenter must content himself with periodic spot checks of such quantities as magnetic field strength and direction and payload temperature.

Another factor implicit in the use of a low duty cycle transmitter is the need for an automatic controller or a command system capable of turning the transmitter on and off. Inasmuch as a Doppler transponder was to be carried aboard the payload for tracking purposes, it was logical to decide to use the greater flexibility inherent in a command system. The command system is also used to fire the injection rocket, to change the rate of transmission of telemetered information, to turn on a simplified television system, and other functions.

Using the vehicle capabilities existing today, it can be anticipated that interplanetary distances will require months to traverse. Thus, equipment designed for interplanetary space probes must have the reliability to endure unattended through the launching and for several months, or even years, in an airless environment while maintaining reasonable equilibrium temperature.

The Able-3 payload incorporates in its design solutions which are felt to be adequate for all of these problems. While these solutions will not be evaluated under actual interplanetary travel conditions, it is believed that enough information will be obtained to increase greatly our confidence in the success of later launchings of truly interplanetary probes. Two photographs of the interior of the payload are given in Fig. 1.

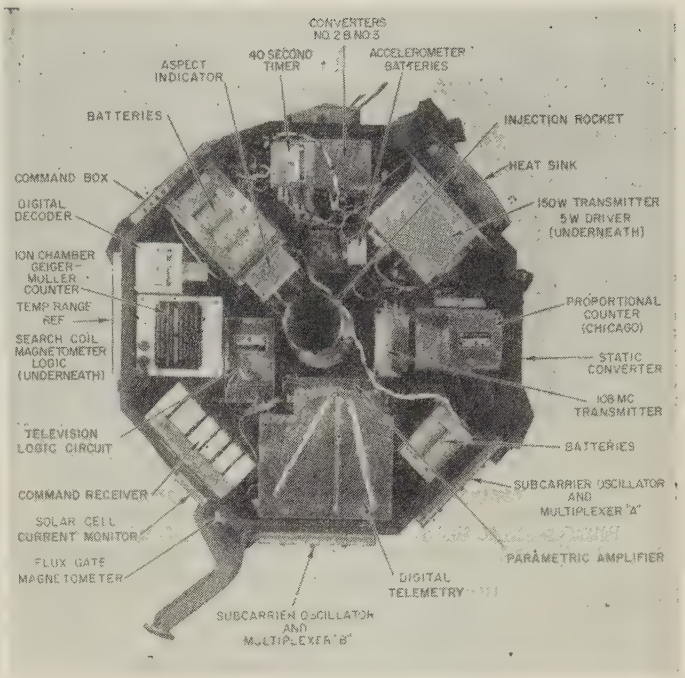

(a)

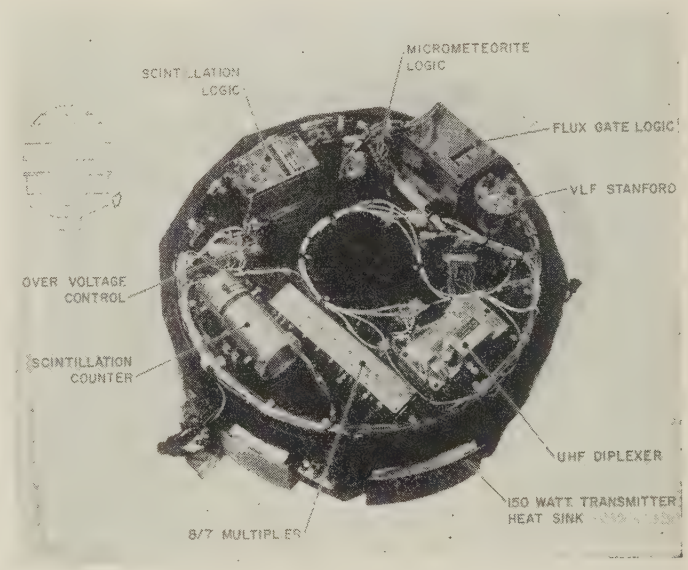

(b)

Fig. 1—(a) Able-3 payload (top view). (b) Able-3 payload (bottom view).

Communications and Tracking

Transmitting and receiving equipment within the payload permits two-way communication. Payload transmitters convey telemetry information to the earth and a payload receiver permits the reception of earth-transmitted commands. When interconnected coherently, the payload receiver and one of the transmitters form a transponder capable of providing both range and range rate information as an aid in tracking the payload.

For communication to the earth, three transmitters are employed. One transmitter accepts an RF signal from the payload receiver, multiplies it eight times in frequency, and amplifies it to a 5-watt level. In the process the resultant signal, whose frequency is 378 mc, has been modulated with a 1024-cps subcarrier containing the time-multiplexed pulse-code-modulated output of a digital telemetry system. Biphase modulation is employed to impress the telemetry output on the subcarrier. This system, when supplemented with a 150-watt power amplifier, whose development was not included for the Able-3 program, forms the basic vehicle-to-earth portion of the interplanetary communication system. The transmitter, about 3 by 6 by 1.6 inches, weighs about a pound, and has an efficiency of about 15 per cent.

Each of two transmitters conveys analog data by means of a six-subcarrier FM-PM telemetry system operating at a carrier power of 100 milliwatts and a frequency near 108 mc. The transmitters together weigh one pound and consume about 1.5 watts of power.

Except for some vehicle performance inputs, both telemeters convey the same information, and thus the older and more proven FM-PM system can be used to monitor the performance of the new digital telemetry system.

The payload command receiver is a transistorized double-conversion, phase-lock-loop receiver which produces a coherent output at 2/17 of the received frequency. It can be operated with either a 250-cps or a 40-cps bandwidth. The receiver operates continuously and, since its band-width is considerably less than the frequency uncertainty of the received signal, it repeatedly sweeps over a range of 30 kc searching for a carrier. The sweep period is 10 seconds for the wide band and three minutes for the narrow band. When the receiver acquires and locks on a signal from the earth the sweeping stops and the receiver can then accept any of 30 possible commands. A list of the 14 commands employed in the Able-3 payload is given in Table I.

TABLE I
COMMANDS TO PAYLOAD

1) Digital Telemetry, 64 pps
2) Digital Telemetry, 8 pps
3) Television On
4) 378-mc Transmitter Off
5) 5-watt Transmitter On
6) Accelerometer On
7) 108-mc Transmitter Off
8) 108-mc Transmitter On
9) Over-Voltage
10) Receiver Wide Band
11) Receiver Narrow Band
12) Clear Rocket
13) Arm Injection Rocket
14) Fire Rocket

Note: When command 4 is given, command 6 is negated and the digital telemetry is restored to 1 pps.

The digital command demodulator was developed after an extensive examination of various time and frequency multiplexed command systems. Investigation indicated that excessive weight and/or unreliability characterized each of the multiple-tone command systems capable of meeting the required bandwidth and frequency stability. The development of the digital decoder, however, required only one narrow-band filter and made use of many of the components already existing in the digital telemetry system.

In the narrow-band position, the receiver exhibits a sensitivity (based on a 12-db noise figure) of -140 dbm. At the present state of development, commands can be given down to a sensitivity of only -133 dbm.

Signals from the earth to the payload are transmitted by using a high-power carrier, phase-modulated with a 512-cps subcarrier. Amplitude modulation of the subcarrier using a train of 13 pulses permits the transmission of a synchronizing pulse, a simple address code, and a 5-bit command together with its complement.

The receiver weighs four pounds, occupies 1300 cubic inches, and draws 1.5 watts at 16 volts. The command decoder used with the Doppler-command receiver is shown in Fig. 2.

In its role as a transponder the payload receiver accepts a CW signal from the ground and after suitable processing delivers it to the 5-watt transmitter for retransmission to the ground at 16/17 of the received frequency.

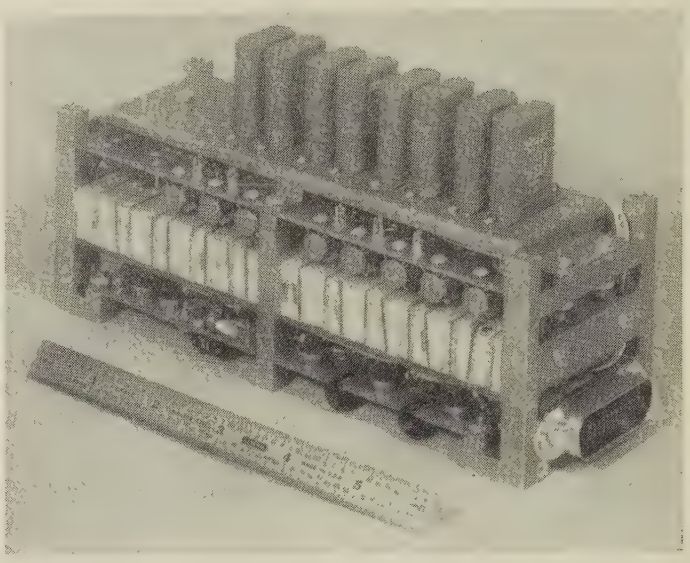

Fig. 2—Command decoder.

Range rate is measured on the ground to accuracies of one foot per second by extracting the Doppler frequency shift between the transmitted and received signal after correcting for the frequency offset introduced by the vehicle transponder. Range is measured by frequency modulating the ground transmitter by low-frequency sinusoids. A modulating frequency of 2 cps provide a range resolution of better than 500 miles when adequate smoothing exists. A second modulating frequency of 0.25 cps is used to resolve the phase ambiguities in the 2-cps signal. Further ambiguities are resolved by measuring the time delay between the start of modulation on the ground and the beginning of modulation in the return signal. Tracking in angle is performed by nodding the ground antenna alternately in elevation and azimuth. Angular accuracies of about 0.2° are possible.

TELEMETRY

The analog telemetry system carried aboard the Able-3 payload is essentially a double-scale version of the system carried aboard the Pioneer I and II payloads. Eleven input signals are applied to two groups of subcarrier oscillators occupying the lowest five and the lowest six IRIG channels respectively. A twelfth signal, a VLF propagation experiment occurs directly as a subcarrier. Two multiplexers sum the two groups of subcarrier oscillator outputs and the VLF experiment and deliver the resultant composite signals to two low-power VHF transmitters. One transmitter delivers a signal whose frequency is 108.06 mc, while the other delivers a signal whose frequency is 108.09 mc.

The digital telemetry system is carried aboard the Able-3 payload principally to evaluate its usefulness in interplanetary probes. However, the automatic data handling techniques which are available for digital information give it a definite purpose for use in an earth satellite. It is anticipated that digital techniques will prove to be better suited to the transmission of information over interplanetary distances than are analog techniques because of the nature

of the thresholding characteristics of the analog system.[1]

The digital telemetry unit developed by STL, the Telebit system, is shown in block diagram in Fig. 3. A photograph of the unit is shown in Fig. 4. This system accepts both analog and digital inputs from various experiments. The converted information at its output appears as a binary coded subcarrier (1024 cps) which then phase modulates the signal of the 5-watt transmitter.

The binary output of the Telebit system occurs at a synchronous rate and is composed of repeating sets of frames of words. For Able-3, 11 words per frame are used. One word of each frame is used as a frame sync and is read out as all zeros, while the balance of the words are coded with the digital representation of the input information. Each word contains 12 pulses. The first two pulses (for information words) are always coded the same (zero, one) and define the start of a word; *i.e.*, these two pulses provide a word sync. The other 10 pulses may take on any combination of binary values to represent a number from zero to 1023.

Another advantage of the digital telemetry system over the analog system is that the rate of transmission of information can be adjusted as a function of range. Provision is made for the transmission of information at the rate of one, eight, or 64 pulses per second. This flexibility of information rate will be found to have its greatest usefulness during the transit of interplanetary distances where large changes in range are encountered. At 55 million miles, using 150 watts of power, information can be conveyed only at one pulse per second; while at less than 500,000 miles, five watts are sufficient to transmit at 64 pulses per second.

A 12-bit combination binary counter and shift register, referred to as a shifting accumulator, is provided for each word. Pulses from a digital-type experiment are applied directly to the counting input of a shifting accumulator while an analog input is applied to an analog-to-digital converter whose output is then applied to a shifting accumulator. An electronic commutator running synchronously at the word rate gates 12 shift pulses to each shifting accumulator during one word interval each frame.

These shift pulses cause the information in the shifting accumulator to be delivered to the biphase modulator and at the same time the output of the digital shifting accumulators is returned to the input so that after 12 shift pulses the state of the shifting accumulators is exactly as it began. The outputs of all of the shifting accumulators are connected together but since only one is shifting at a time no interference results.

The conversion of analog to digital information is accomplished with the aid of a digital ramp and a voltage comparison circuit. In essence conversion results from counting the number of steps in the ramp below the level of the analog input. The counting is actually done in a

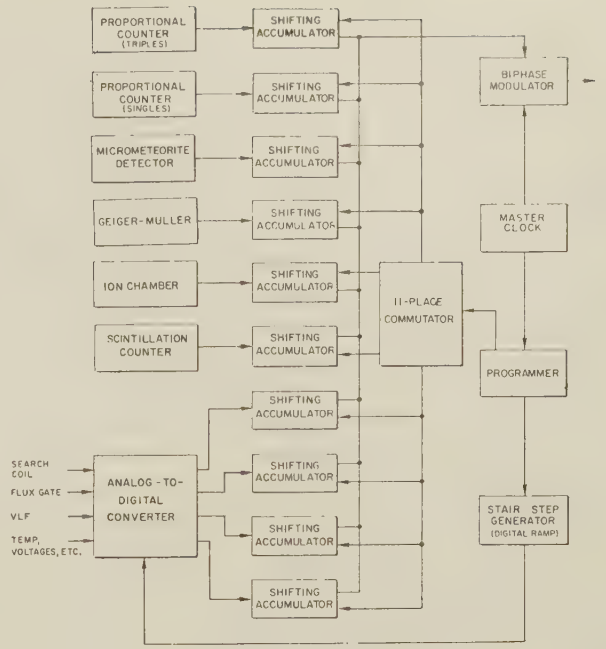

Fig. 3—Block diagram of telebit system.

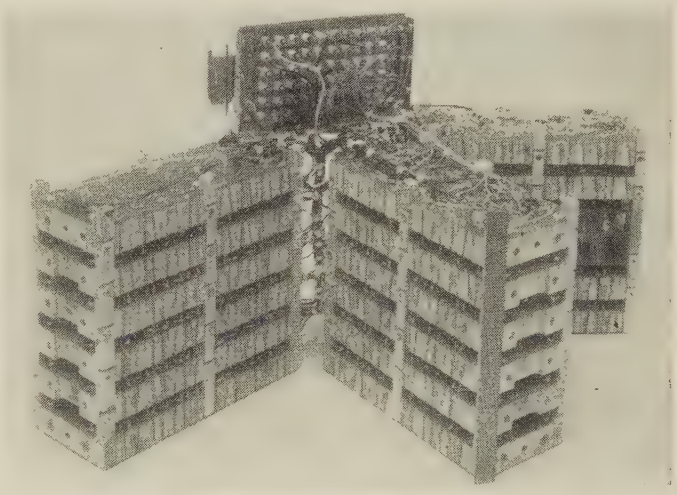

Fig. 4—STL telebit unit.

shifting accumulator just as for digital experiments. The Able-3 payload has six digital and four analog shifting accumulators.

The biphase modulator accepts the pulses emerging sequentially from the shifting accumulators and produces a subcarrier whose phase shifts by 180° each time there is a "one" to be transmitted and retains its phase each time a "zero" is to be transmitted. This biphase modulated subcarrier is then delivered to the transmitter for phase modulation upon the carrier.

The pulses which cause the electronic commutator to step and the shift registers to shift originate in the programmer, and the programmer in turn receives its excitation from the master clock. The programmer is equipped such that application of an outside signal derived from the digital command decoder causes the pulse rate of the digital telemetry system to change.

[1] G. E. Mueller and J. E. Taber, "An interplanetary communication system," 1959 WESCON Convention Record, pt. 5, pp. 68-75.

Antennas

The Able-3 payload uses both VHF and UHF for data transmission and UHF for guidance functions. The VHF transmission circuit from the two transmitters consists of a coaxial ring hybrid for coupling both transmitters to the single antenna system, a shunt tuning stub to match the antenna system to the hybrid, a diplexer for diverting signals for the VLF whistler mode experiment, and two monopole antennas.

The VHF diplexer consists of a resonant circuit tuned to 15 kc for the whistler experiment and is shunted by a band-pass filter employing a helical transmission line. The VHF monopole antennas are conventional in design and operate against the payload shell as the ground plane. Although the resultant radiation pattern is perturbed by the nonplanar ground plane and the solar cell paddles, pattern coverage and gain are adequate for the mission requirements. The UHF antennas, similar in design to the VHF radiators but appropriately scaled in length, are two monopoles operating against the payload shell located on the opposite end of the payload from the VHF antennas. Both the antenna systems are symmetrically located with respect to the spin axis of the payload.

Power Supply

Placing solar cells directly on the surface of the payload presented two difficulties: 1) the surface area of the payload was too small to permit adequate solar energy interception; and 2) inasmuch as the solar cells also absorb large quantities of heat, the payload temperature would be intolerably high. An early decision was made to locate the solar cells on paddles extending essentially radially from the payload. These paddles fold within the nose fairing during launch but when fairing is jettisoned they spring out and latch into place. The paddles extend radially 22.5° from the payload equatorial plane as shown in Fig. 5. Approximately 8000 silicon solar cells are carried on the Able-3 satellite. Because of attitude and spin considerations, however, only about 2000 of the solar cells are receiving solar energy at one time. A prototype paddle with solar cells mounted on it is shown in Fig. 6.

The payload storage battery possesses a 50-watt-hour capacity at 16.8 volts. A type of battery which would have been lighter for the same capacity, such as silver zinc, was not chosen because of doubtful reliability. Part of the power developed in the solar cells is immediately consumed in experiments and the receiver, and the charging rate of the battery is thus lessened by this amount. It is anticipated that between six and ten hours will be required to completely recharge the battery.

An over-voltage control operated on command from the ground can be used to reduce the charging rate if it appears that the battery is being consistently overcharged. An under-voltage control is provided which automatically removes the 5-watt transmitter from the load on the batteries in case battery discharge goes so far as to disable the receiver and thus prevent commanding off the transmitter from the ground.

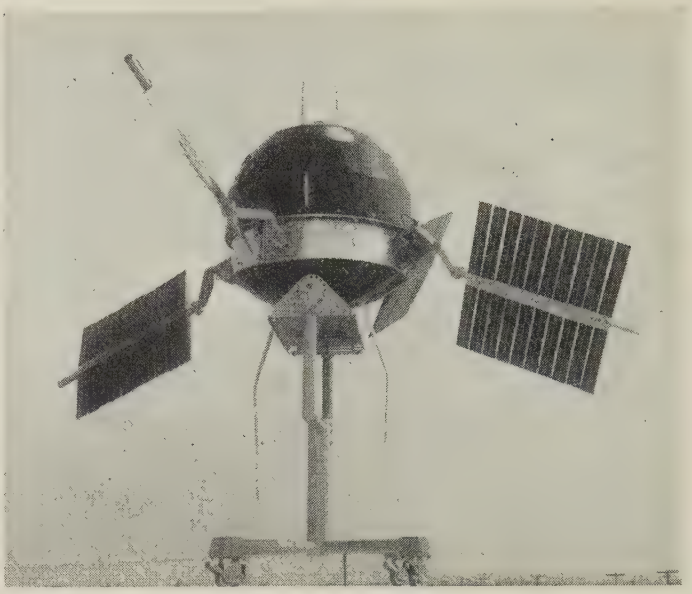

Fig. 5—Able-3 payload with paddles latched in position.

Fig. 6—Solar cells mounted on paddle.

The batteries operate at 16.8 volts. Since this voltage is inadequate for all of the electronics, a series of static converters is employed to provide a variety of voltage levels.

Temperature Control

Temperature control of the payload is achieved by arranging the thermal balance between input solar radiation and infrared emission so that it occurs at a temperature within the desired operating range. This is done by select-

ing a surface coating that will give a value of the ratio of solar absorptivity to long wavelength emissivity (α/ε) in the range of about 1.0 to 1.3.

A similar problem exists in the solar cell paddles but there is less freedom of solution. Furthermore, the solar cells are quite temperature-sensitive and their conversion efficiency drops off about 0.6 per cent per degree Centigrade above a nominal value of 25°C.

Because the absorptivity-to-emissivity ratio of a silicon cell is about 3, the cells will run excessively hot unless their surfaces are coated to alter the long wavelength emissivity. Thus glass plates, 0.0003-inch thick, cemented individually to each cell, are used to increase the long wavelength emissivity without appreciably altering the cells' conversion efficiency. To protect the cement from ultraviolet radiation and to reduce the cell temperature even more by eliminating a part of the solar spectrum to which the solar cells are functionally insensitive, an ultraviolet reflective coating is applied to the glass before it is cemented to the cell. For the glass plates to reduce the temperature successfully, it is essential that the glass be bonded to the cell over the whole surface so that there is no gap to cause a greenhouse effect.

The large thermal capacity of the payload prevents large drops in its internal temperature for eclipses expected during the first 1000 days of flight. Temperature drops of 15 to 20°F are the most severe that are expected during this time. After about 1000 days, however, long eclipses (about 2½ hours duration) will occur; the payload temperature drop by the end of such eclipse will be the order of 50°F.

Temperatures of the solar cells, on the other hand, drop rapidly during an eclipse. While there is, of course, no operating requirement for the solar cells during an eclipse, they must be able to survive the low temperatures. For a one-half hour eclipse, the lowest temperature on the solar cell paddle should be about −50°F, and about −175 to −200°F for a 2½-hour eclipse.

Conclusion

Considerable effort has gone into the solutions briefly outlined here. The component and system designs represented by the payload are felt to be sound and laboratory environmental testing has indicated their reliability. However, long-term operation in space can provide the only adequate test and the results of this test are bound to indicate areas requiring further development. In any event, future space probe vehicles necessitating considerably more sophisticated instrumentation at considerably further ranges will be able to profit from this experience.

Three-Dimensional Interplanetary Trajectories*

A. B. MICKELWAIT†, E. H. TOMPKINS, JR.†, AND R. A. PARK†

Summary—**Developments in guided missiles and related scientific areas have reached a state where ballistic flights to the planets Venus and Mars are feasible and imminent with existing hardware. This paper discusses considerations involved in making actual ballistic flight to Venus. Conventional two-dimensional analysis is compared to the actual three-dimensional case. Burnout conditions required to minimize the problems of guidance, payload, range safety, booster aerodynamics, midcourse guidance, and capture are established. Problems relating to launch times, launch latitude, and interplanetary communications are also discussed.**

Introduction

ALL significant design criteria for interplanetary vehicles come directly from the interaction between the gross properties of interplanetary ballistic trajectories and their sensitivities to small initial disturbances. In other words, the dynamic and geometric problems must be considered simultaneously with the accuracy requirements. In fact, the two subjects are so interrelated that propulsion and guidance requirements, the engineering counterparts of orbital analysis, must be regarded as inseparable in interplanetary vehicle design in order to adequately resolve the often conflicting demands of payload needs and high accuracy.

It is commonplace to consider the effects of the relative orientation of the earth's rotational axis, the earth's orbital plane, and the orbital plane of the other planets as niceties that can be relegated to the final high-precision orbit determination. For earth-bound satellites this is largely true. Indeed, although for lunar missions three-dimensional considerations cannot be neglected, they do not usually contribute decisive vehicle design factors. However, even a preliminary analysis of interplanetary flights indicates that they can miss their goals by an order of magnitude, from the point of view of both payload and accuracy, if an oversimplified two-dimensional analysis is relied upon.

Because Venus has an almost optimum orientation in its orbital plane with respect to the earth's orbital plane

* Manuscript received by the PGMIL, July 21, 1959.
† Space Technology Labs., Inc., Los Angeles, Calif.

in 1959, the trajectory design problem for a flight to Venus in 1959 will be analyzed in the most detail. The characteristics of this trajectory will be contrasted with the problems of flights to Mars in 1960 and Venus in early 1961. To keep the paper a reasonable length, primary attention will be given to purely ballistic flights, that is, flights with no orbit corrections after leaving the earth's vicinity. Furthermore, the paper will be limited to the range of propulsion and guidance capabilities available at the present time. However, it will become apparent that no interplanetary mission even with the crudest requirements would have a reasonable probability of success unless some midcourse or terminal guidance is carried out; therefore some trajectory characteristics directly pertinent to these problems will be introduced.

Two-Dimensional Kinematics

First, we will assume that the earth and target planet move in circular orbits in the same plane and that the earth's equator is in this plane. Let us assume further that the vehicle is launched and flies in this common equatorial plane. To handle the analytically intractable multiforce problem posed by the attraction of the sun and all the planets simultaneously, we will assume that the vehicle's orbit consists of three phases (see Fig. 1): first, escape hyperbola centered at and determined solely by the earth's gravitational field; second, the sun-centered ellipse controlled only by sun's gravity and using injection conditions taken from the escape hyperbola leaving the earth; and third, a reverse of the first phase, the approach hyperbola centered at the target planet and controlled entirely by its gravity.

When leaving the earth, the vehicle is launched from a platform (the earth) moving about 100,000 feet per second around the sun. For most practical trajectories to Venus or Mars, the vehicle leaves the earth with a velocity of about 36,000 to 40,000 feet per second relative to the earth. By the time it has left essentially all of the earth's gravity along the escape hyperbola relative to the earth, it either adds (going to Mars) or subtracts (going to Venus) only about 10,000 feet per second to the earth's much larger orbital velocity. Although, in principle, it is possible that a significant spatial error at injection into the sun's field could occur (that is, in two dimensions, an error in the radial distance from the sun) other constraints upon launch and burnout conditions, which will be discussed later, make this possibility negligible. Therefore, this source of error will not be discussed. The guidance problem is then simply that of achieving those conditions at burnout which will give the vehicle the correct velocity when it enters the sun's field. If the mission requirements are made sufficiently stringent—say, for example, that one wishes to impact at a particular point on Venus—position variables at injection into the sun's field would need to be considered, but midcourse corrective maneuvers could be used to reduce this source of error.

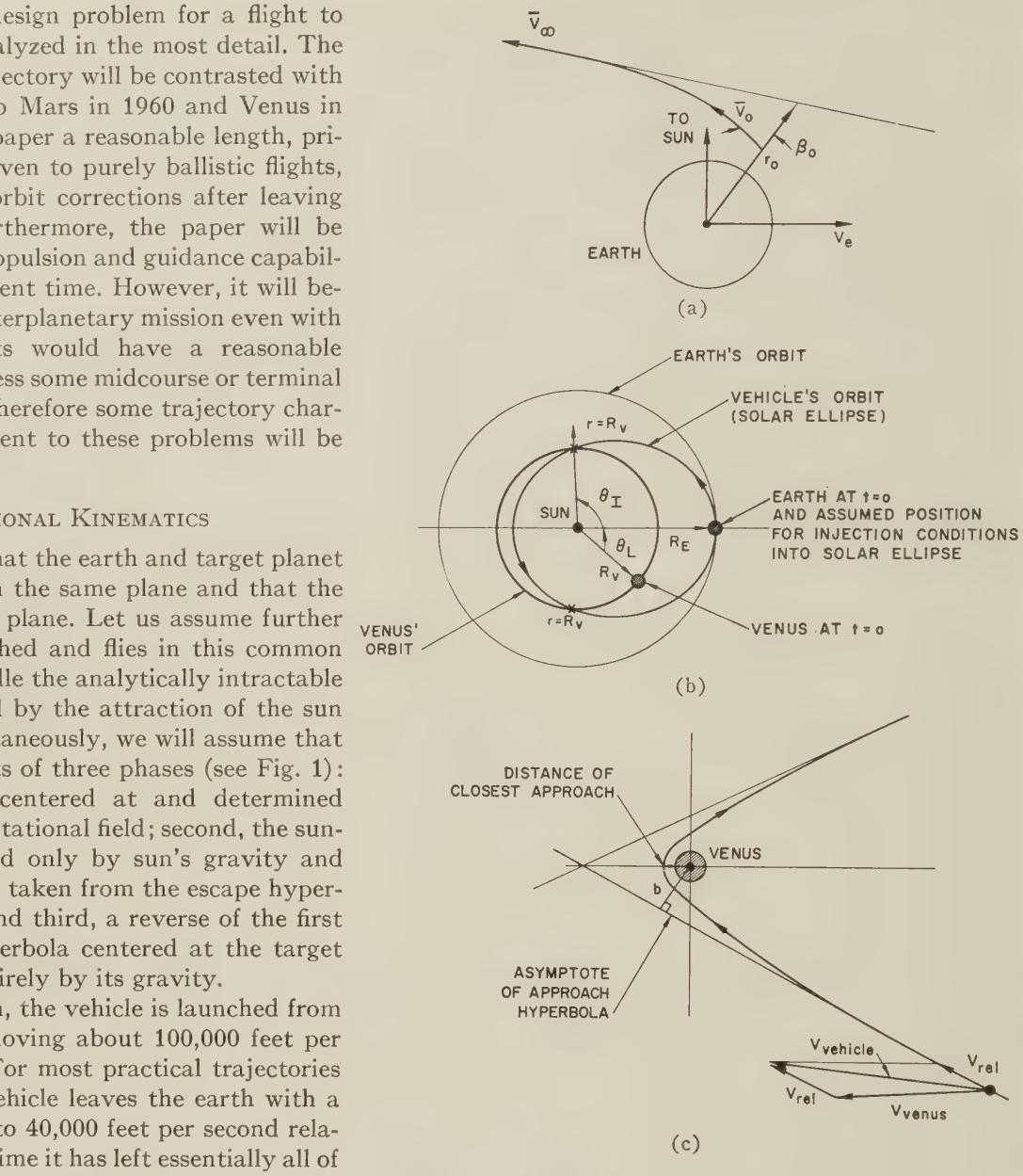

Fig. 1—Two-dimensional coordinate systems for the three flight phases. (a) Escape hyperbola relative to the earth; (b) solar ellipse; (c) approach hyperbola relative to Venus.

At this point it should be noted that our lack of knowledge of certain physical constants, especially the relevant dimensions of the solar system, will introduce their own uncertainties in position and velocity. However, the most recent estimates of the error contributed by our lack of exact knowledge of the astronomical unit indicates that it can be safely ignored when compared with other sources of error, even if the present estimate of experimental uncertainty is doubled.

Fig. 1(a)-1(c) shows the coordinate systems used and the relative orientation of earth and Venus at take-off. It is apparent from the geometrical relationships shown in this figure that the conditions in the sun's frame of reference for a successful flight are given by

$$\theta_I(V_s, \beta_s) = \omega_v T(V_s, \beta_s) - \theta_L(t_o) \qquad (1)$$

when

$$r = R_v$$

where

θ_I = the angle in the sun's frame of reference turned by the vehicle between injection and impact
ω_v = mean angular velocity of Venus
T = total flight time
θ_L = initial lead angle of earth relative to Venus
r = vehicle distance from the sun
R_v = Venus' mean orbital radius.

Eq. (1) says that the properties of the trajectory after injection are determined entirely by the magnitude of the velocity at injection into the sun's frame, $|V_s|$, and the angle between $\boldsymbol{V}_s$ and the radius from the sun, β_s. It follows that if the launch day is fixed, that is, if θ_L is fixed, then there exists a functional relation between $|V_s|$ and β_s. Referring to Fig. 1(b), we see that this relation may not be one to one; that is, there may be two sets of $|V_s|$ and β_s allowable on a given launch day, one set (Class I orbits) corresponding to an impact when $r = R_v$ as the vehicle crosses the Venus orbit the first time and the other set (Class II orbits) to that trajectory when the vehicle impacts as it crosses the Venus orbit the second time.

The classification of orbits into classes is useful for several reasons. One important system consideration, communication transmission distance, depends strongly on the orbit class. Class II orbits generally involve longer times of flight than the minimum energy orbits (~147 days to Venus and 260 days to Mars). Since the target planet is moving away from the earth at the end of a minimum energy trajectory at the rate of about 10 nautical miles per second, relatively small changes in flight time can radically increase or decrease the transmission distance. In fact, only several hundred feet per second change in take-off velocity can vary the transmission distance by as much as 30 million miles.

It is clear that the most efficient use of $\boldsymbol{V}_\infty$ is made when it is collinear with the velocity vector of the earth, $\boldsymbol{V}_e$, and when $\beta_s = 90°$. If the magnitude of $\boldsymbol{V}_\infty$ is fixed and its direction changed, $\boldsymbol{V}_s$ rotates so that β_s does not equal 90° and a larger $|V_s|$ results (Fig. 2). A larger $|V_s|$ implies, of course, a shallower penetration into Venus orbit. When $\beta_s = 90°$, reducing $|V_\infty|$ increases $|V_s|$ until the two points where the vehicle crosses Venus' orbit coalesce. The vehicle's trajectory is then tangent to Venus' orbit at $r = R_v$, and the vehicle travels exactly 180° from launch to impact as measured relative to the sun (the "Hohmann" transfer ellipse). A smaller $|V_\infty|$ and therefore a smaller take-off energy will give an orbit around the sun that falls inside of the earth's orbit but does not touch Venus' orbit.

Recalling that (1) related θ_L, $|V_s|$, and β_s, we see that if β_s and $|V_s|$ are adjusted for a minimum energy orbit, then a unique launch day is determined. For other values of θ_L (varying roughly one-half degree per day for the earth and Venus) and for the most efficient $\beta_s = 90°$, smaller values of $|V_s|$ will be required since the two points of intersection must move away from $\theta_I = 180°$, implying a deeper penetration inside of Venus' orbit than the Hohmann ellipse and, therefore, greater reduction of the original $|V_e|$.

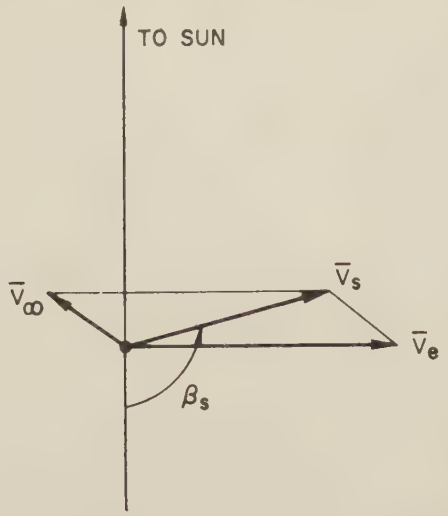

Fig. 2—Relation of the earth's velocity, V_e, and vehicle's velocity with respect to the earth after escape, V_∞, to vehicle velocity in the sun's frame, V_s.

Fig. 3 shows the increase in velocity requirements over and above that required for the two-dimensional Hohmann ellipse as the angle θ_L is increased or decreased away from 54°. The system implication of the velocity increase is that there is a definite period of days during which launching to another planet is feasible with limited propulsion capabilities. On the other hand, since the angular velocities of Venus, earth, and Mars are quite different,[1] the required relative angular orientation will reoccur periodically with the so-called "synodic" period; for Venus every 584 days, for Mars every 780 days. As we shall see, however, when the inclination of the various orbit planes are taken into account, the time between reoccurrence of identical launching conditions becomes much larger. The key dates to be kept in mind for planetary probes are June 7, 1959 to Venus, October 11, 1960 to Mars, and January 7, 1961 to Venus again. On these days, at least with a two-dimensional analysis, the minimum energy θ_L occurs.

In addition to conserving energy, the minimum energy trajectory is also desirable for another reason. Most missions attempt either to maximize the length of time spent in the target planet's vicinity or enter the target planet's atmosphere as slowly as possible to diminish deceleration and heating. In any case, the slowest possible relative approach velocity is desirable. From Fig. 1(c), and recalling that the inertial velocities of target and vehicle are of the order of 100,000 feet per second,

[1] Earth, $\omega_E = 0.986°$/mean solar day,
Venus, $\omega_V = 1.600°$/mean solar day,
Mars, $\omega_M = 0.524°$/mean solar day.

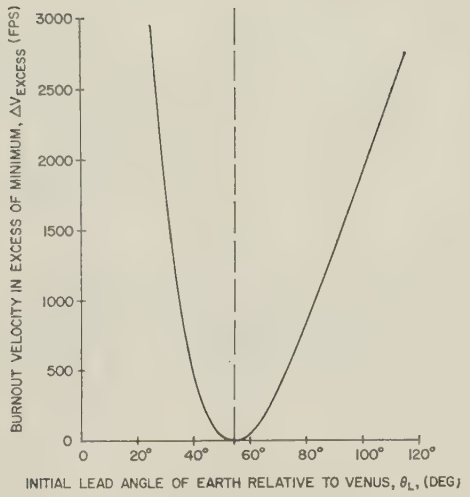

Fig. 3—Burnout velocity in excess of minimum as a function of lead angle, θ_L.

we see that even a small inclination of the vehicle's velocity, V_{veh}, to that of the target planet, V_v, can greatly increase the relative velocity, V_{rel}. Therefore, the tangential approach afforded by the two-dimensional Hohmann ellipse provides the desired minimum approach velocity.

Considerations concerning the approach phase of the trajectory may be made more quantitative by relating the injection conditions into the approach hyperbola to the distance of closest approach. By utilizing one-body formulas expressing conservation of energy and angular momentum relative to the target planet, we arrive at a relationship between the impact parameter, b, approach velocity, V_{rel}, and distance of closest approach, D:

$$b = D\sqrt{1 + \frac{2GM_v}{DV_{rel}^2}}. \tag{2}$$

The impact parameter is simply the distance the vehicle would miss the target in the absence of any attraction by the target planet. The quantity (GM_v) is the universal gravitational constant times the mass of the target planet. For an impact, D would, of course, be set equal to the target radius.[2] For the lowest possible approach velocity to Venus, ~9000 feet per second the maximum allowable impact parameter is about twice D; that is, the gravity field of Venus has effectively doubled the geometrical size. Clearly, then, from this standpoint alone it is desirable to keep V_{rel} as low as possible.

Two-Dimensional Guidance Analysis

The first approach to studying sensitivity (of the trajectory to errors at burnout) is to look at the sun-frame ellipse by itself. From (1) we see the expressions

$$\Delta S_v = R_v\left(\frac{\partial(\theta_I - \omega T)}{\partial V_s}\right)\Delta V_s$$

and

$$\Delta S_\beta = R_v\left(\frac{\partial(\theta_I - \omega T)}{\partial \beta_s}\right)\Delta \beta_s$$

give the distance from the target planet when the vehicle crosses the target orbit due to injection errors ΔV_s and $\Delta\beta_s$. However, this is not the actual miss distance due to injection dispersions since the vehicle is usually closer to the target either before or after crossing the target orbit. Either the variation of distance of closest approach, D, or variation of impact parameter, b, are more suitable measures of orbit sensitivity. The impact parameter is often used extensively since its sensitivity is easier to calculate. If the approach velocity is kept within a small range, the maximum allowable dispersion in b for the success of a given mission may be established. Then

$$\Delta b_{max} = \left[\left(\frac{\partial b}{\partial V_s}\Delta V_s\right)^2 + \left(\frac{\partial b}{\partial \beta_s}\Delta\beta_s\right)^2\right]^{1/2} \tag{3}$$

determines the allowable dispersions in β_s and V_s over this range of approach velocities. Eq. (3) assumes implicitly that ΔV_s and $\Delta\beta_s$ are random, independently distributed quantities. In Figs. 4 and 5, we see the variation of the impact parameter miss coefficients $\partial b/\partial V_s$ and $\partial b/\partial\beta_s$ over a range of injection conditions. The important behavior to note here is the vanishing of β_s sensitivity at minimum energy and the vanishing of V_s sensitivity at velocities slightly above minimum energy. Although not shown in Figs. 4 and 5 (the curves are for Class I orbits only), Class II orbits do not possess the zero in velocity sensitivity.

The two-dimensional analysis presented so far is deficient for two important reasons. First, the effect of escape phase has not been included in the analysis. Referring to Fig. 1, we see that a change in β_0 at burnout varies the orientation of $\boldsymbol{V}_\infty$ although not its magnitude. But changing the orientation of $\boldsymbol{V}_\infty$ changes both β_s and $|V_s|$. Likewise, a change in $|V_0|$ will change $|V_\infty|$ and therefore change both β_s and $|V_s|$ simultaneously. Only when $\boldsymbol{V}_\infty$ becomes collinear with $\boldsymbol{V}_e$ do β_0 and V_0 interact directly with their counterparts in the sun's frame of reference. However, as will be shown in the next section, when the complete three-dimensional situation is taken into account, it is very difficult to have $\boldsymbol{V}_\infty$ parallel to $\boldsymbol{V}_e$ except for a unique orientation of the earth relative to Venus. Furthermore, when the third degree of freedom is introduced, the relations between burnout conditions and injection conditions become more complex. The net result is that the strong mimina in sensitivity are flattened out and in fact will vanish altogether except for isolated situations. In the light of the failure of the two-dimensional analysis to carry over into three dimensions, it is not fruitful here to carry out the com-

[2] Radius of Venus ≅ 3410 naut mi, radius of Mars ≅ 1820 naut mi.

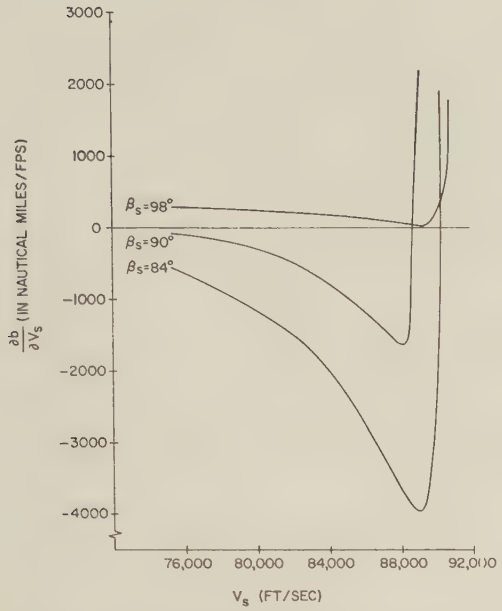

Fig. 4—Two-dimensional velocity miss coefficient, $\partial b/\partial V_s$, as a function of the vehicle velocity in the sun's frame, V_s, for three flight path angles in the sun's frame, β_s.

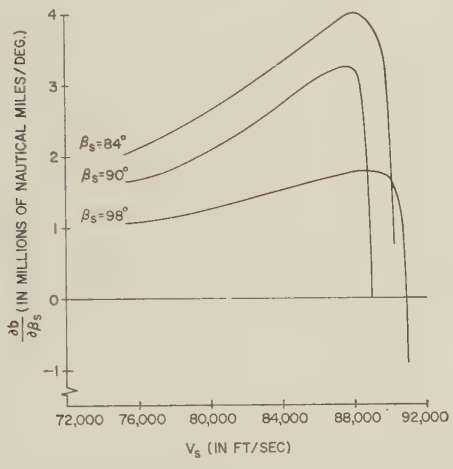

Fig. 5—Two-dimensional angular miss coefficient, $\partial b/\partial \beta_s$, as a function of vehicle velocity in the sun's frame, V_s, for three flight path angles in the sun's frame, β_s.

plete analytical treatment of connecting burnout dispersions to solar injection dispersions and then to impact dispersions; rather we will present in the next section some results of the exact computer analysis of orbit sensitivities.[3]

Three-Dimensional Considerations

Although the orbital planes of the earth and Venus are inclined to each other by only a small angle (~3.4°), the three-dimensional aspects of their relationship has a strong influence on the energy, guidance, and target

[3] A complete two-dimensional analysis is presented in T. A. Magness, J. B. McGuire, and O. K. Smith, "Accuracy Requirements for Interplanetary Ballistic Trajectories," Space Technology Labs., Rept. TR-59-0000-00682, May 18, 1959; presented at the Ninth Annual Congress of the International Astronautical Federation, Amsterdam, The Netherlands, August 25-30, 1958.

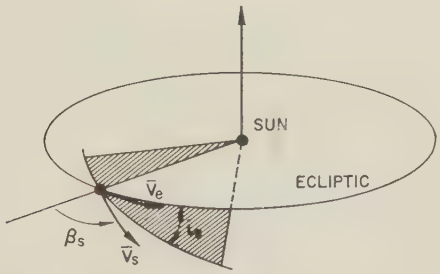

Fig. 6—Three-dimensional coordinate system in the sun's frame.

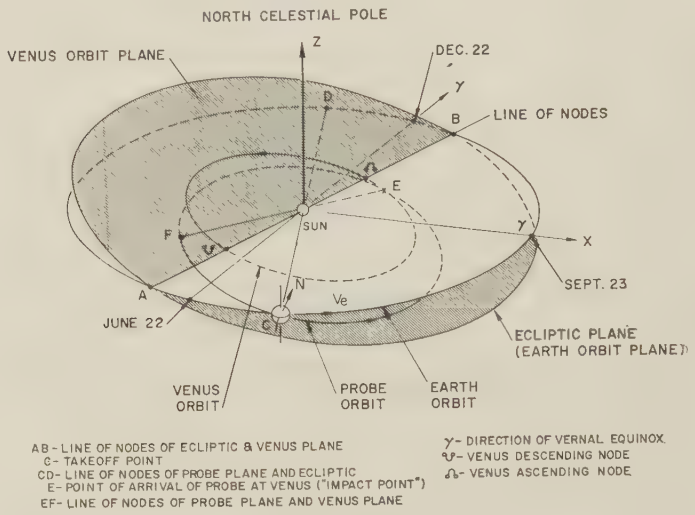

Fig. 7—Three-dimensional aspects of the orbits of Venus, earth, and the probe.

approach of the free-flight trajectory. We shall consider first the energy relations for the three-dimensional situation.

A. Energy Considerations

Let a probe be launched with a burnout velocity, V_0, in a coordinate frame, S_e, fixed at the center of the earth (but not rotating with the earth). As the probe leaves the vicinity of the earth it travels along a hyperbolic escape orbit with its velocity vector gradually approaching the asymptote of the hyperbola, and its magnitude gradually approaching a constant value, V_∞. As before, the velocity of the earth with respect to the sun is $\boldsymbol{V}_e$. The vector sum of $\boldsymbol{V}_\infty$ and $\boldsymbol{V}_e$ is again $\boldsymbol{V}_s$, which is the velocity of the probe in the sun's reference. To a close approximation, the probe's orbit will lie in a plane through $\boldsymbol{V}_s$ and the center of the sun. Finally, the angle between the ecliptic (the plane of the earth's orbit) and the probe's orbit plane is i_s and the angle between $\boldsymbol{V}_s$ and a radius vector from the probe to the sun is β_s, as shown in Fig. 6. The quantities V_s, i_s, and β_s are the three-dimensional "injection conditions" for the probe orbit about the sun.

Fig. 7 shows the inclined orbital planes of the earth and Venus intersecting in the line AB (the line of "nodes"). Imagine first that the inclination is set equal to zero so that both orbits lie in the same plane. This case is identical to the two-dimensional case described in the

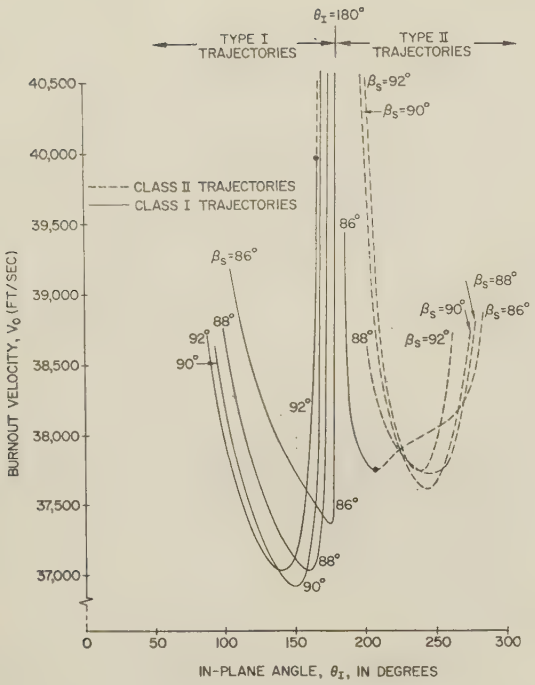

Fig. 8—Burnout velocity, V_0, as a function of the in-plane angle, θ_I, for various flight path angles in the sun's frame, β_s (Venus flight' 1961 era).

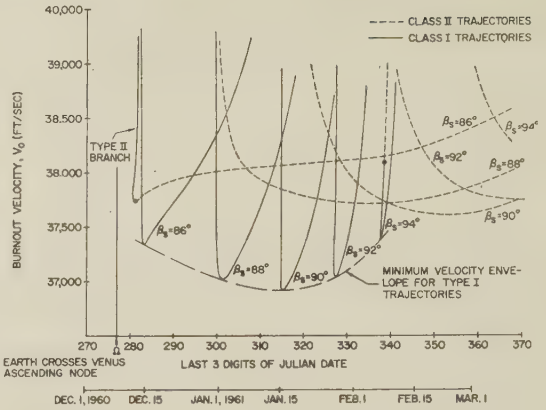

Fig. 9—Burnout velocity, V_0, as a function of launch dates for various flight path angles in the sun's frame, β_s (Venus flight, 1961 era)

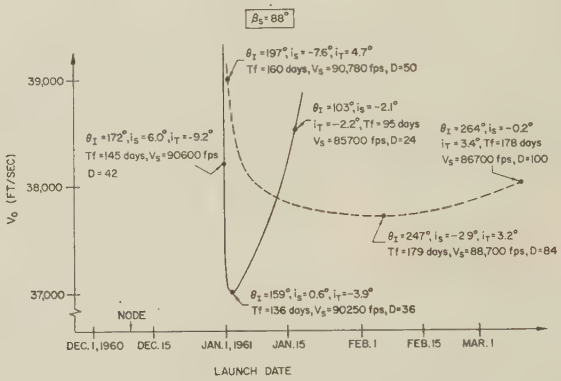

Fig. 10—Detailed analysis of one curve, flight path angle, $\beta_s = 88°$, of burnout velocity, V_0, as a function of launch date (from Fig. 9). In-plane angle, θ_I, angle between the plane of the ecliptic and the probe's plane, i_s, angle between the probe's plane and Venus plane, i_T, time of flight, t_f, velocity of the probe in the sun's frame, V_s, and distance between the earth and Venus when the probe reaches Venus, D, (in millions of nautical miles) are given at various points on the curves.

previous sections, and the Hohmann transfer ellipse to Venus will occur when $\theta_Z = 54°$. For the real solar system, the inclination of Venus' plane is not zero, and in each synodic period the two-dimensional minimum energy lead angle of $\theta_L = 54°$ will occur at varying places on the earth's orbit. Suppose $\theta_z = 54°$ when the earth is in the position shown in Fig. 7. If a probe is launched then with $i_s = 0°$, that is, in the ecliptic, it can reach Venus *only* at a point such as the ascending node, Ω, where Venus crosses the ecliptic plane. However, for this trajectory θ_I is much less than 180°, implying a quicker trip and expenditure of more energy (by changing V_s or β_s) than in the two-dimensional case. One might take a longer trip and reach Venus at the descending node, $\mho$, but this would also require more energy. Consider now the situation when i_s is changed from zero. In the two-dimensional case, the minimum energy flight traveled 180° around the sun. Study of Fig. 7 will show that a value of $\theta_I = 180°$ in three dimensions is possible only for the case when the trajectory travels almost over the ecliptic pole ($i_s \sim 90°$), a maneuver which would require an extremely large burnout velocity (>100,000 feet/sec). Let us look at some of the details on realistic energy requirements.

Fig. 8 shows the burnout velocity, V_0, on earth as a function of the in-plane angle, θ_I, for constant values of β_s for flights to Venus in the 1960–1961 era. Each point on the curves corresponds to a certain $\{V_s, i_s\}$ set and thus to a certain launch date and flight time. In this figure, the following orbit classification is used:

Type I trajectory—has a flight angle $\theta_I \leq 180°$,

Type II trajectory—has a flight angle $\theta_I \geq 180°$,

Class I trajectory—arrives at Venus on first crossing Venus' orbit,

Class II trajectory—arrives at Venus on the second crossing of Venus' orbit.

Fig. 9 shows V_0 as a function of launch date for constant values of β_s. From Figs. 8 and 9, it can be seen that the three-dimensional minimum energy flight to Venus in the 1960–1961 era occurs about January 15, 1961 (over a month after the earth crosses Venus' line of nodes) with $\beta_s = 90°$ and $\theta_I = 150°$. For this flight, $V_0 = 36{,}920$ feet per second (about 300 feet per second above the two-dimensional absolute minimum velocity), $i_s = 1.1°$, $V_s = 90{,}000$ feet per second, and flight time $t_f = 126$ days. The probe orbit makes an angle of $\sim 4.3°$ with the Venus plane, and, on the launch date, the earth leads Venus by $\sim 36°$ rather than the 54° predicted by two-dimensional analysis. Figs. 8 and 9 also show, as was concluded from Fig. 7, that considerable additional velocity in excess of the minimum must be expended to obtain an in-plane angle near 180°. Fig. 10 shows in detail the parameters corresponding to several points on the $\beta_s = 88°$ curve of Fig. 9. Considering such points, one

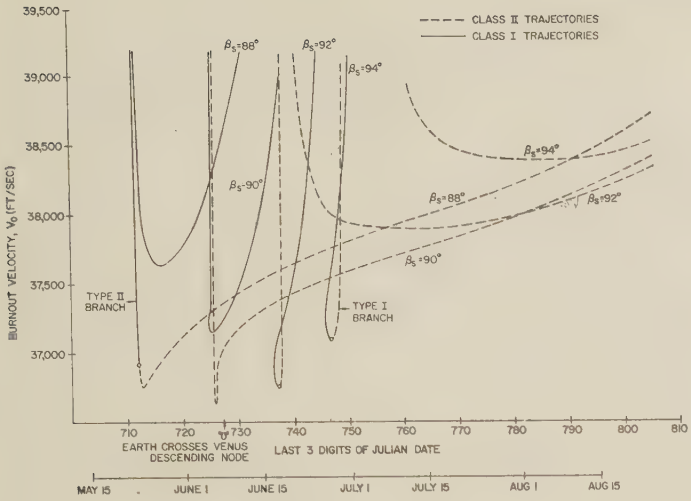

Fig. 11—Burnout velocity, V_0, as a function of launch dates for various flight path angles in the sun's frame, β_s (Venus flight, 1959 era).

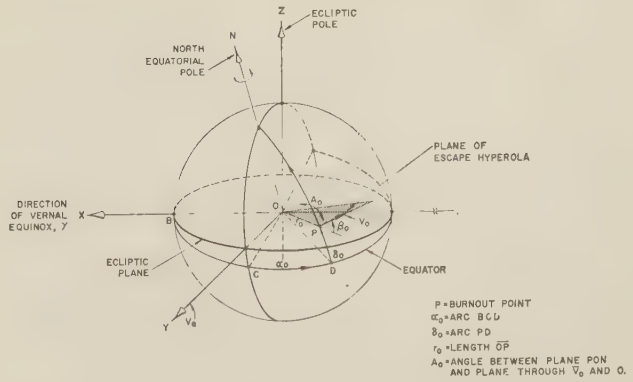

Fig. 12—Coordinate system at burnout in the earth's frame.

may begin a systems analysis of a Venus flight by examining such factors as the following:

1) Each operating point on the curves determines a particular out-of-plane angle, i_T, and in-plane angle (through θ_I) at the crossing of Venus' orbit. These angles have a strong effect on the guidance sensitivity of the trajectory and hence on the probability of success of the flight. They also affect the relative approach velocity in Venus' frame and hence the capture, impact, or landing requirements.
2) Similarly, each point implies a certain transmission distance at the time of arrival of the probe. The fact that this transmission distance may vary from 23 to 138 million nautical miles will have a strong influence on communication capability in the early years of interplanetary flight and will, in large measure, determine the actual trajectory flown.
3) Each point implies a particular set of burnout angles for a given launch site. As will be shown in a later section, these angles may be quite unacceptable either because they affect the efficient operation of the powered flight part of the trajectory or because they may result in the booster stages impacting in inhabited areas.

In contrast to Fig. 9, Fig. 11 shows V_0 as a function of launch date with a constant β_s for Venus flights in the 1959 era. It should be noticed that the 1959 flights present a very special set of characteristics resulting from the fact that the three-dimensional minimum energy trajectory occurs very close to the time of the earth's crossing of Venus' line of nodes; which is to say that the three-dimensional trajectory is almost identical with the two-dimensional trajectory. It was therefore possible to fly with near absolute minimum velocities on essentially two-dimensional trajectories which entered Venus' plane at the descending node-crossing and arrived nearly tangential to Venus' orbit at the ascending node. This coincidence will occur every eight years, but there will be a gradual secular change away from the exact two-dimensional conditions. Once the conditions become a few weeks apart, the two-dimensional analogy is no longer relevant; therefore, the 1959 case should be regarded as essentially illustrative.

One should also note that by increasing burnout velocity only a relatively small amount above the minimum, flights to Venus in each era are possible over a period of several months and that a wide variety of types of trajectories is possible during each period. These problems related to energy considerations are only one factor to be balanced against others in the complete systems analysis.

B. The Three-Dimensional Escape Trajectory

We shall now define the variables used to specify completely the burnout conditions of the powered flight on earth and show how these variables are constrained by the conditions V_s, β_s, and i_s of the sun-frame transfer orbit.

It is convenient to employ the following set of initial conditions in studying the powered flight, specified at a burnout time t_0 (t_0 = date + time of day):

α_0 = right ascension[4] of burnout point
δ_0 = declination[5] of burnout point
r_0 = geocentric radius of burnout point
V_0 = magnitude of inertial burnout velocity
β_0 = angle between inertial velocity vector, $\boldsymbol{V}_0$, and geocentric radial line ("velocity path angle")
A_0 = azimuth of $\boldsymbol{V}_0$ from North, measured in a plane perpendicular to the geocentric radius at the burnout point.

These definitions are illustrated in Fig. 12. In reality, the escape hyperbola will blend into the elliptical orbit around the sun and no clear-cut place will exist which one can speak of as the injection point into a central force orbit about the sun. Thus, one must ultimately

[4] Right ascension is the astronomical measure of longitude from the vernal equinox, which is the ascending node of the sun in its apparent motion around the earth.

[5] Declination is the astronomical measure of latitude from the equatorial plane.

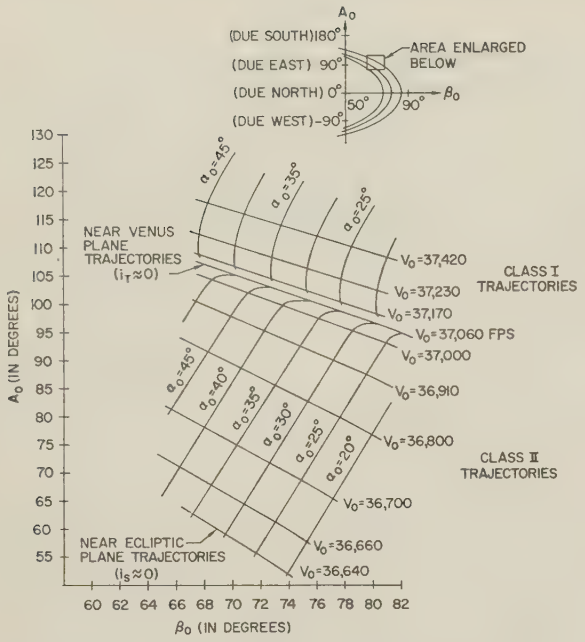

Fig. 13—Azimuth, A_0, as a function of flight path angle, β_0, for various burnout velocities, V_0 (Venus flight, June 6, 1959, Cape Canaveral launch, burnout altitude 22,000,000 feet from center of the earth).

determine α_0, δ_0, r_0, V_0, β_0, and A_0 at t_0 as initial conditions of a system of differential equations of the probe's motion such that the probe reaches a specified point on or near Venus. These equations must include the effects of the earth's oblateness and the attraction of the moon, Venus, etc. We shall now follow this approach. The sun-frame conditions V_s, β_s, and i_s, will remain useful guides, however.

Let us hold r_0 fixed at a reference altitude of 22,000,000 feet ($\sim$177 nautical miles above the earth's surface). The powered flight will normally lie approximately in a plane through the launch site at lift-off and the burnout point at t_0. To conserve energy, it is desirable that the free-flight continue in this same plane. Therefore, δ_0 and the longitude of the burnout point are determined once the range of the powered flight arc over the earth, the location of the launch site, and the azimuth, A_o, are chosen. From the longitude of the burnout point and the burnout time, t_0, the right ascension, α_0, may be computed. Three parameters, azimuth, A_0, flight path angle, β_0, and burnout velocity, V_0, remain to be chosen. Fig. 13 shows A_0 as a function of β_0 with curves of constant burnout velocity, V_0, for a flight to Venus launched from Cape Canaveral, Fla. on June 6, 1959. The curves were obtained by integration of the full equations of motion in a computer program which iterated the initial conditions to obtain a probe impact at Venus. Different points on the constant V_0 curve correspond to different α_0 values, and hence to different burnout (and launch) times.[6] The curves of constant V_0 correspond roughly to curves of constant i_s.

[6] The right ascension of a fixed point on the earth's surface varies as the earth rotates since it is referred to the vernal equinox which is a fixed line in inertial space.

For a given mission and launch site, the range of "possible" flight azimuths is tied closely to the sun-frame orbit and the planet geometry. The curves in Fig. 13 permit powered flight azimuths well within the bounds of the Cape Canaveral test range. However, the "possible" azimuths for any given mission may be at odds with range safety problems. But using "safe" azimuths may have adverse effects upon the other system factors such as energy, guidance, communication distance, etc. This problem can be clearly illustrated utilizing the reasonable launch time to Mars of September 23, 1960 when the earth is at the autumnal equinox, as shown in Fig. 12.

A flight to Mars on this date can be made a simple geometric problem for illustration since i_s is equal to 0° and $\beta_s = 90°$ at a reasonable velocity. To achieve these values for i_s and β_s, we must make $\boldsymbol{V}_\infty$ and the asymptote of the escape hyperbola be parallel to the earth's velocity vector. $\boldsymbol{V}_\infty$ must also *add* to $\boldsymbol{V}_e$, carrying the probe out towards Mars' orbit. One way in which this may be accomplished is to fly *due north* (azimuth, A_o, equals 0°) from the launch site at the instant when Cape Canaveral passes through the plane containing the earth's axis and $\boldsymbol{V}_e$. The escape geometry then lies in a plane as shown in Fig. 14. If the powered flight is assumed to cover a 15° arc over the earth's surface, the escape hyperbola must turn through an in-plane angle, $\theta_h = 113°$, to bring $\boldsymbol{V}_\infty$ parallel to $\boldsymbol{V}_e$. Analysis shows that a Class II flight to Mars with a V_0 of $\sim$37,600 feet per second at $r_0 = 22{,}000{,}000$ feet can achieve $i_s \sim 0°$ and $\beta_s \sim 90°$ (approximately the minimum three-dimensional V_0 for a 1960 Mars flight). Given V_0, r_0, and β_0, the angle θ_h may be computed from simple two-body formulas. Conversely, if V_0, r_0, and θ_h are known, the burnout velocity path angle, β_0, is determined. Fig. 15 shows θ_h vs V_0 for various values of β_0 with $r_0 = 22{,}000{,}000$ feet. From this figure, we see that our Mars flight requires a β_0 of $\sim$72°.

However, suppose it is necessary to increase azimuth A from 0° to, say, between 100° to 125° for reasons of range safety. This may be done by delaying launch until the launch site has rotated farther east which inclines the escape hyperbola plane (Fig. 16). However, this will decrease θ_h and, as is seen in Fig. 15 for a fixed V_0, decrease β_0. This generates curves of β_0 vs A_0 similar to those of Fig. 13. In fact, however, for an efficient powered flight, β_0 is limited to a practical range of 65° to 90°. Thus, a practical limit on the azimuth which can be followed is reached when β_0 goes below 65°. For the case shown, it appears that the hypothetical range safety considerations make the flight impossible on the assumed launch date. However, there are several alternatives:

1) Change the initial conditions at injection into the sun's frame, and/or the launch date so that $\boldsymbol{V}_\infty$ will have a more satisfactory direction. This will usually involve the expenditure of additional

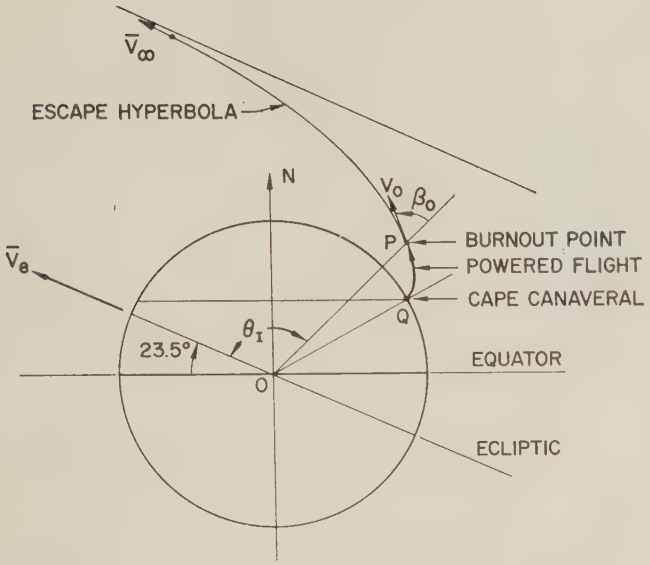

Fig. 14—Geometry of escape hyperbola which lies in a plane including the earth's velocity vector.

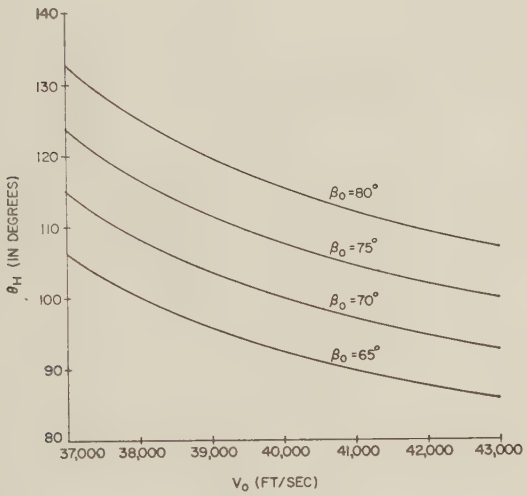

Fig. 15—In-plane angle of escape hyperbola, θ_h, as a function of burnout velocity, β_0, for various flight path angles at burnout, β_0.

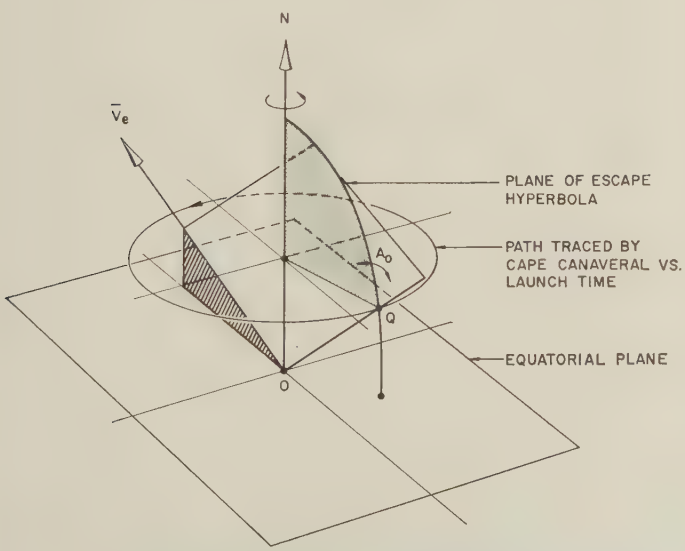

Fig. 16—Rotation of escape hyperbola with change in launch time.

energy to increase V_0, and also this may produce trajectories which have undesirable guidance or communication properties.

2) Launch at an earlier time when the trajectory plane through the launch site is inclined in a northwest-southeast orientation, launching in the *southeast* direction. This would also be incompatible with a reasonable β_0 since θ_h would be too large. Now, however, the probe may be placed in a satellite orbit and allowed to coast approximately halfway around the earth until the proper θ_h can be obtained after a final stage has been fired to inject into the escape hyperbola.
3) Relocate the launch site.

Some or all of these alternatives may be undesirable. This example merely emphasizes that launch azimuth considerations may have a very strong effect on the systems analysis of interplanetary flights in the early years of such flights.[7]

C. Three-Dimensional Guidance Requirements

After nominal interplanetary trajectories have been determined, the next step is to study the effect of dispersions of the nominal produced by variations in the initial conditions (burnout conditions of the powered flight). Such a study will establish the requirements which must be met by a guidance system acting during the powered flight parts of the trajectory. But, as mentioned earlier, the guidance requirements themselves will have a strong bearing on the choice of a nominal trajectory since specific "good guidance" trajectories exist which are less sensitive to errors by a factor of 10 or more than neighboring trajectories.

The terminal (or impact) portion of a three-dimensional interplanetary trajectory may be described in a manner analogous to the two-dimensional discussion. The approach hyperbola centered at the target planet may be characterized by the velocity relative to the target planet at a great distance from it, $V_{\text{rel } T}$, and the impact parameter, b. The magnitude of the impact parameter, now a vector quantity, is still defined as the distance of closest approach which would occur if the target has no gravity. (More precisely, $\boldsymbol{b}$ is the vector from the center of target planet that is perpendicular to the asymptote of the approach hyperbola.) $\boldsymbol{b}$ then shows the direction and is a measure of the distance of closest approach without gravity (not the actual miss with gravity) of the probe at the target planet. The sensitivity of the miss to changes in the initial conditions (α_0, δ_0, β_0, A_0, V_0, r_0) back on earth may be measured by defining the *vector miss coefficients*:

$$\mathcal{B}_m = \frac{\partial \boldsymbol{b}}{\partial \beta_0}, \qquad \boldsymbol{V}_m = \frac{\partial \boldsymbol{b}}{\partial V_0}, \qquad \text{etc.},$$

[7] The problem will change from era to era; for example, azimuths required for the 1960–1961 Venus flights are much more in a northerly direction than for the 1959 Venus flights.

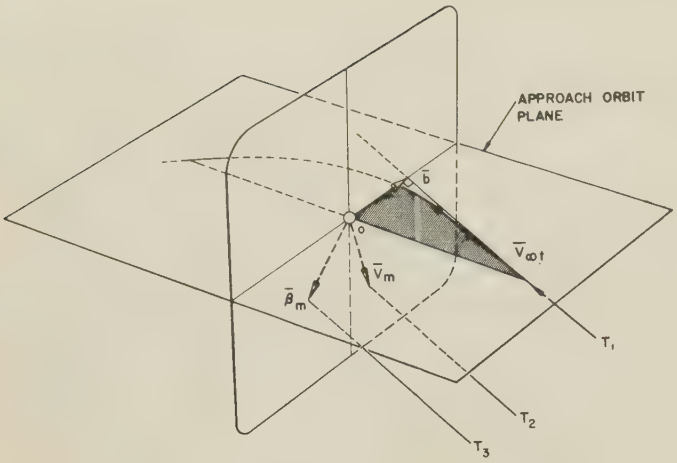

Fig. 17—Geometry of approach phase to target planet.

where $\mathfrak{B}_m$ is the miss coefficient of the flight path angle, $\boldsymbol{A}_m$ of the azimuth and $\boldsymbol{V}_m$ of the velocity. Suppose, for example, a nominal trajectory has been obtained whose asymptote passes through zero (Fig. 17) providing a "dead-center" impact on the planet. A change of 1° in the β_0 of the nominal will move the trajectory away from zero, say to the trajectory T_3. $\mathfrak{B}_m$ will be a directional measure of the resulting miss in nautical miles per degree.

Let us now return to the β_0 vs A_0 curves of Fig. 13 and examine how the miss coefficients $\boldsymbol{V}_m$, $\mathfrak{B}_m$, and $\boldsymbol{A}_m$ vary with the operating point on these curves and with launch date. Figs. 18 and 19 show curves of V_m, β_m, and A_m as a function of V_0 for two launch dates for Venus probes in June, 1959.[8] These velocity profiles correspond to A_0 and β_0 values along a constant α_0 (~launch time) curve on the β_0 vs A_0 plots. Machine computations show that ordinarily the miss coefficients along a constant V_0 curve vary only slightly as compared to the variations which occur with changes in V_0. Therefore, since points on a constant V_0 curve correspond to changes in launch time, it follows that the miss coefficients with constant V_0 vary only slightly if launch time is varied by an hour or so.

Figs. 18 and 19 indicate the guidance accuracy required for interplanetary ballistic flights—angular error sensitivities of 40,000 to 500,000 nautical miles miss per degree and velocity sensitivities of 1000 to 20,000 nautical miles per feet per second being typical. The sensitivities vary strongly with the class of orbit, the launch velocity (~i_s), and the relation of the launch date to the earth's crossing of the target planet node. Furthermore, the "good guidance" points for V_0, β_0, and A_0 will ordinarily not occur at the same operating point on the β_0 vs A_0 curves so that optimization procedure must include a knowledge of the magnitudes of each of the errors at burnout that the guidance system cannot eliminate.

[8] These miss coefficient curves were obtained with a computer program which solved a system of variational equations along with the normal equations of motion of the probe.

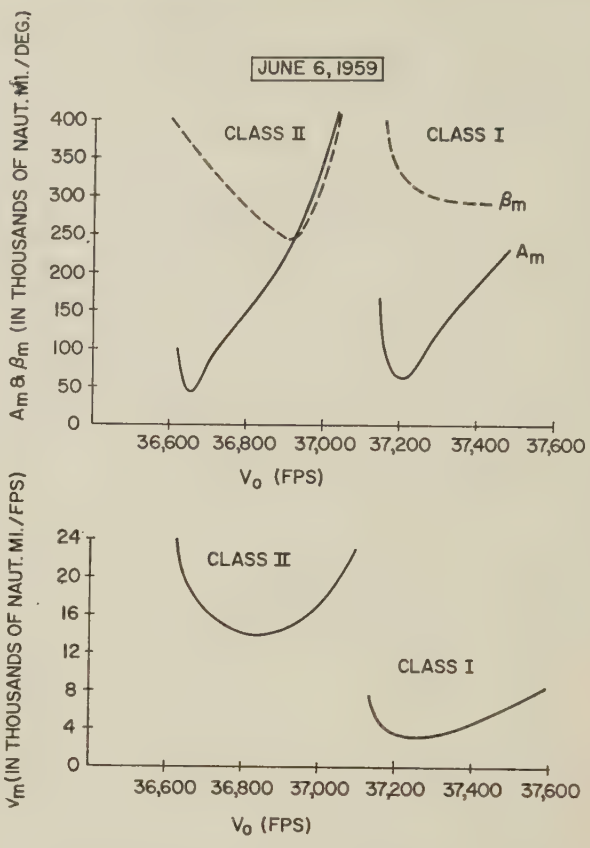

Fig. 18—Velocity, flight path angle, and azimuth miss coefficients V_m, β_m, and A_m, as a function of burnout velocity, V_0, for Venus flight, June 6, 1959 (before the earth crosses line of nodes).

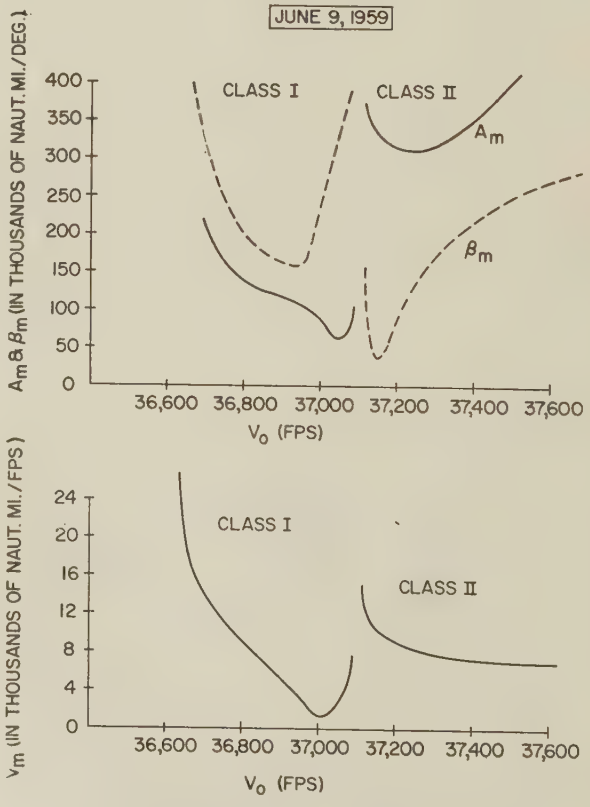

Fig. 19—Velocity, flight path angle, and azimuth miss coefficients, V_m, β_m, and A_m, as a function of burnout velocity, V_0, for Venus flight, June 9, 1959 (after the earth crosses line of nodes).

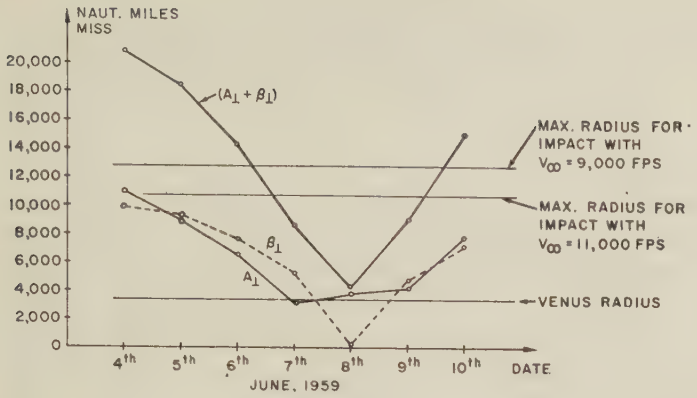

Fig. 20—Residual miss components, azimuth perpendicular, $A_\perp$, and flight path angle perpendicular, $\beta_\perp$, and their sum for $\frac{1}{3}°$ errors in A_0 and β_0. The parallel components have been removed at vernier correction (Venus flight, June 1959).

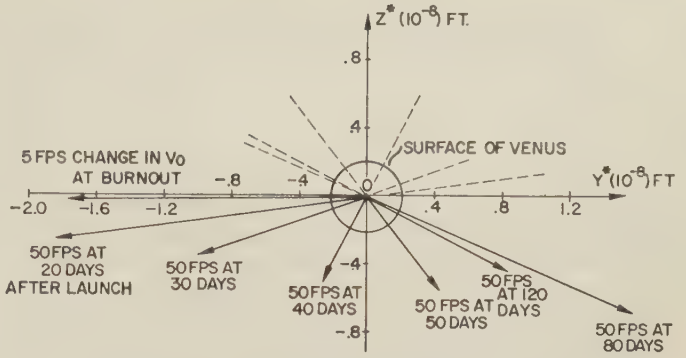

Fig. 21—Change in magnitude and direction of vector impact parameter resulting from midcourse correction as a function of time of correction (Venus flight, June 8, 1959, $V_0 = 37{,}050$ feet/sec). y^* axis approximately parallel to the ecliptic plane; z^* axis is perpendicular to the asymptotic velocity vector.

These extreme burnout tolerances required for interplanetary ballistic flights may be met if a very high degree of accuracy is attained at burnout or if vernier corrections are made in the first few hours of flight. For vernier correction, tracking data obtained in the first hour or so of the free-flight may be used to compute the actual burnout conditions accurately. The required correction can then be determined and sent to the probe by radio command.

Study of the angular orientation of the miss coefficient vectors has shown that for certain take-off days and burnout conditions, these vectors are almost collinear. The angular errors then appear equivalent to velocity errors and may be corrected with vernier velocity corrections on the probe. The closeness with which collinearity can be achieved will vary sharply with launch date. Consider that the β_m vector is resolved into components $\beta_{||}$ and $\beta_\perp$, parallel and perpendicular to the vector $\boldsymbol{V}_m$, and let $\beta_{||}$ be eliminated by vernier velocity correction. Fig. 20 shows the variation of the residual miss $A_\perp$ and $\beta_\perp$ after early vernier correction (per $\frac{1}{3}° A_0$ and β_0 error) as a function of launch date for 1959 Venus flights. The points shown correspond to the most collinear operating region on each day.

In addition to an early vernier correction, midcourse guidance corrections using long-term tracking data and commanded by radio can also be easily done. Suppose that the probe axis is stabilized in its flight on the sun-frame orbit at the attitude the axis had near burnout, which would be the case if the vehicle is spin stabilized. Then the vector Δb_k representing the change in vector impact parameter from the nominal caused by a midcourse velocity impulse or "kick" will rotate in the miss vector plane as a function of the time of kick (Fig. 21). We may in effect resolve effects of burnout errors into components parallel and perpendicular to $\boldsymbol{V}_m$, remove parallel components with an early vernier and perpendicular components with midcourse vernier rocket firing at the proper time. The midcourse corrections may also remove residual parallel components, taking advantage of the much more precise knowledge of the orbit gained by tracking in the early months of the flight. Such correction schemes have the advantage of requiring minimal equipment in the payload since computation and decision functions will be carried out on earth using computers and communications equipment already required for tracking and telemetry.

Conclusions

This brief review of interplanetary ballistic trajectories shows their extreme complexity, but it also indicates that a satisfactory method of analysis has been developed. The three-dimensional analysis of the problems associated with these trajectories shows that conventional two-dimensional analysis is inadequate to understand the basic problems. If Figs. 4 and 5 are extrapolated back to burnout conditions in the earth's field and then compared with Figs. 18 and 19, it is apparent that the two-dimensional miss coefficients are inaccurate by a factor of 5 to 10. Moreover, of course, two-dimensional analysis is wholly misleading in that it cannot consider the many practical problems, such as powered flight considerations, range safety, target approach velocity, etc., which are essential to a successful mission.

What this paper attempts to show is that if a proper trajectory analysis is carried out and ingeniously exploited, existing propulsion systems, unsophisticated stabilization techniques such as spin, and relatively crude guidance systems are satisfactory for sending vehicles on interplanetary missions near each minimum energy time. However, if target approach velocity is not a central consideration, as in an impact case, or if communication transmission distance is not considered, then six to eight months each synodic period are available for launch to Venus and similar periods for launches to Mars. But such trajectories require an even more sophisticated combination of trajectory analysis and guidance techniques at burnout, post-burnout, and midcourse. The point is that whatever the accuracy guidance system adopted, or whatever the capability of the propulsion system, interplanetary flight can only be successfully achieved if the realistic dynamics of the trajectory problem are fully examined and understood.

Detection and Evaluation of Space Radiations*

DEPAUL T. CORKHILL† AND R. A. HOFFMAN†

Summary—**In the very near future man will escape from his terrestrial environment and venture into space. The first flights will be limited space voyages circling the earth only one or several times at altitudes from 100 to 500 miles. As technological advances permit, these space journeys will become longer in duration and farther from earth until travel between planets in our solar system is accomplished. Ultimately of course, travel outside our solar system is envisioned.**

The hazards of space flight are numerous. An environment paralleling that of the earth's must be simulated as closely as possible inside the space capsule. In providing such an environment, those problems of air regeneration, temperature control, pressure control, etc., are overcome. One potential hazard from which man in space cannot be effectively protected is radiation. Therefore, the intensity of space radiations and their biological effects must be evaluated prior to prolonged space journeys if such journeys are to be accomplished without undue risk.

The aeromedical field laboratory is now studying a space radiation detection system which would be capable of detecting and identifying the several forms of space radiation and the intensity of each form. Once the types and intensities of radiation prevalent in space are ascertained, it will be possible to study, in earth laboratories, the biological effects of most of these radiations. Radiobiological studies should lead to realistic RBE (relative biological effectiveness) values for these radiations, and thus biological dose rates (rem/hr) can be established.

A radiation survey system such as described will be a very intricate electronic assembly. The biological studies to determine RBE values will require careful study. The unit must be compact, rugged, and lightweight if it is to be adaptable to satellite flights.

Presently, a feasibility study is underway to determine the most practical and efficient electronic assembly. Then follows the fabrication of the complete detection system. Orbital flights of this system must then be made to evaluate the types and intensities of space radiations. Biological studies of these radiations must then be made so that biological dose rates may be established. Once the biological studies have been completed, the RBE factors can be incorporated in the radiation detection system, *i.e.*, a system which will be capable of giving the space passenger a biological dose rate in rem/hr on a dial type instrument as well as his total accumulated radiation dosage during the flight. Admittedly, such a system may not be a prerequisite for the first toddling steps of man into space, but it must certainly form an integral part of future space vehicles when bolder journeys farther from earth are made.

MAN is presently at the threshold of escaping his terrestrial confines and venturing into space. Many problems have evolved and have been solved in approaching this new era of space flight; many are yet to be solved and undoubtedly others will be presented after man has made his first orbital flights. Yet we remain undaunted, and certainly interplanetary flights within our solar system will become a reality in the not too distant future with space voyages to other solar systems following as technological advances permit.

Technical advances in rocket design, propellants, electronics, etc., have made possible the launching of artificial earth satellites, moon rockets, and tiny artificial planets circling our sun. The hostile environment of space presents additional problems to biological systems. These problems are now under study and must be solved prior to man's initial venture into space. On earth, man is surrounded by an atmosphere to which he is adapted. Proper concentrations of oxygen, nitrogen, and carbon dioxide are present, and atmospheric pressure is such that gaseous exchanges can take place within our biological system. Also, our bodies are adapted to this pressure and any marked deviation will present serious consequences. The thin blanket of atmosphere surrounding the earth provides us with protection against harmful components of solar radiation, cosmic radiation, and meteorites, besides serving as a buffer against sudden severe temperature fluctuations. Earth's gravity provides us with a sense of weight which allows us to orient ourselves with our surroundings. These comprise only a few of the comforts which we enjoy on earth, and which are lacking in space. Design of a space vehicle in which the earth's environment can be closely simulated is the ultimate goal. This is not impossible, but for at least two factors—one of providing weight, and second, of providing protection against space radiations—it is extremely difficult. This paper is concerned with space radiations and will be limited primarily to this subject.

The types of radiation prevalent in space are not thought to differ appreciably from terrestrial forms except for one type—heavy primary cosmic particles ($Z > 6$). These interact with our atmosphere and are broken into smaller secondary fragments before reaching earth. The primary cosmic radiation is composed of nuclei of elements ranging from hydrogen through iron in approximately the following proportions—80-85 per cent protons, 14-17 per cent alpha particles and approximately one per cent heavier elements. When these primary particles interact with the space atoms and molecules or are influenced by strong magnetic fields, they produce the other types of radiations found in space such as gamma rays, beta particles, positrons, π and μ mesons, secondary protons, neutrons, neutrinos and secondary alpha particles. It is obvious, then, that the types of space radiations are similar to those found on earth except for these heavier primary cosmic particles. The energies of space radiation is quite another matter. While the energy of terrestrial produced radiations is limited in most instances to MEV

* Manuscript received by the PGMIL, July 21, 1959.
† Operations Sec., Aeromedical Field Lab., AF Missile Dev. Center, Holloman AFB, N.Mex.

or a few BEV, the space radiations may possess energies of many BEV. The maximum energy levels are as yet unknown. It is presently thought that these high energy levels will appreciably affect the biological damage caused by these radiations. This will be discussed in more detail in another section of this paper.

Detection of space radiation and determination of the intensities of the various components present still another problem. Certainly detection instruments are now available which are capable of detecting most of these radiations. However, it is desirable to have one detection system, lightweight, rugged, and compact, which, when exposed to a field of mixed radiation, such as in space, is capable of detecting the various types, separating each type into subgroups according to energy, and finally determining the intensity of each subgroup. Obviously, this differs greatly from laboratory conditions where the type of radiation and even the energy distribution may usually be known. A study of a detection system with the capabilities listed, which would be adaptable to satellite use, is now in progress.

The biological damage caused by ionizing radiation is generally attributed to the formation of ion pairs as the ionizing particle or photon traverses matter. One possible exception to this mode of action would be the damage produced by the heavy primary cosmic particles. These may produce minute damaged areas per particle as these particles terminate in tissue. More study must be done in this area of radiobiology to determine if such an effect exists rather than the general toxic effect of free radicals as is the case with other radiations. Further, the damaging characteristics of one radiation relative to another (relative biological effectiveness, RBE) is thought to be related to the ionization density or linear energy transfer (LET) as the particle passes through matter. The greater the LET, the greater the biological damage which is due to a greater concentration of ion pairs per unit volume of tissue.

The LET of ionizing radiation is influenced by the energy of the radiation and even more by the charge of the particle. For example, an electron of 500 kv energy has a greater LET than one of 5 MEV and an alpha particle ($Z = 2$) has a much greater LET than an electron. As was mentioned earlier, the types of space radiation may not differ appreciably from terrestrial forms except for the heavy primary cosmic particles, but it is expected that much more energetic radiation will be encountered. Since the energy of a radiation is related to LET and this, in turn, to biological damage, it is obvious that the damage produced by these very energetic space radiations may differ considerably from the same type of radiation, possessing less energy, which is found on earth. It is therefore necessary to ascertain the energy and intensity of the various space radiations and increase our studies of the biological effects of the most energetic radiations available in laboratories so that realistic RBE values may be formed for the very high energy space radiations. These RBE values would then be incorporated into the detection system allowing a biological dose rate in rem to be made. This is, of course, the ultimate goal—to have a radiation survey system which integrates the dosage attributable to each form of radiation into an over-all dose rate and total accumulated dose which could then be read on a dial similar to the speedometer of an automobile.

A study of a space radiation detection system is now underway by the Lockheed Missiles and Space Division under a contract with the Aeromedical Field Laboratory of the Air Force Missile Development Center, Holloman Air Force Base, N.M. Two approaches to a detection system were considered. One approach would provide a dose rate and accumulated dosage but would not identify the various radiations. The dose rate on such a system would automatically be based on the LET of the radiations as measured by the system. The second approach would be a system of detectors capable of analyzing the radiation spectrum into its various components and energy levels. Subsequent incorporation of RBE values would allow this type of system to provide a biological dose rate and total accumulated dosage. The first approach would probably prove simpler in design, and, after evaluation of ambient space radiation with respect to types and energy levels, this may prove the system of choice for future routine incorporation into space craft. It is felt that first the space radiations should be identified and the intensity and energy levels determined, and it was because of these factors that the second approach was chosen for the present study.

The system chosen to survey the forms and energy of ambient space radiations will undoubtedly prove to be an extremely complex electronic apparatus. As was stated before, this unit should be able to survey all the space radiations encountered, subgroup some of the forms according to energy, determine the intensity of each group, and telemeter and record these data. Such a system must ingeniously combine almost all of the presently known detection instruments plus some possible new ones. The equipment must be miniaturized to the maximum extent still maintaining excellent performance. It must be lightweight and yet sturdy enough to withstand the rigors required of space flight.

We have limited our discussion to the detection and evaluation of space radiation and the possible biological hazards posed by these radiations. This is by far the primary objective of the proposed radiation survey system; however, any radiation in the space cabin produced by nuclear propulsion methods may also be monitored. The proposed unit will be capable of including such radiation in its survey since these radiations will not be unique among those encountered in space. Therefore, all ionizing radiations present in the space cabin, and the dose rate and dosage from these radiations will be adequately monitored.

In summary, the primary objective of the radiation detection system now under study is to detect and analyze ambient space radiations. Information concerning types of

radiation encountered and energy levels obtained from initial flights should be used as the basis for additional laboratory studies on very energetic forms of radiation. Establishment of realistic RBE values from these studies and incorporation of these values into the detection system should provide a manner in which the dose rate and total accumulated dosage will be available to the space passenger at all times.

A radiation survey or monitoring system such as the one proposed will probably not be necessary for the initial manned space voyages at altitudes of 100 to 500 miles. As technological advances permit, man will journey farther into space—to other planets of our solar system and, eventually, beyond. Certainly the radiation hazard of such journeys must be evaluated, and constant monitoring during the flight accomplished, if undue risk is to be avoided.

High-Accuracy Electronic Tracking of Space Vehicles*

P. F. von HANDEL† and F. HOEHNDORF†

Summary—**It is the purpose of this paper to show that optical accuracies can be reached with electronic tracking if the refractive index is known at the site of the radar, as well as at the site of the target. This is the case in tracking space vehicles with microwaves. The index can be measured at the tracking site and it is unity beyond the denser atmosphere. Ionospheric influences can be neglected in the higher kilomegacycle range. It is also shown that the uncertainty of the course of any particular profile between the surface of the earth and the target has only minute effects on range and angular errors. Accuracy limits are determined and presented numerically. The inherent high precision of modern electronic tracking systems can be fully utilized under these conditions; this is not the case in tracking vehicles flying in the atmosphere.**

THE inherent angular precision of modern electronic guidance and tracking systems is basically given by the ratio of the baseline between system antennas to the wavelength. Using frequencies in the higher kilomegacycle range and long baselines, almost any desired precision can be reached.

The inherent range precision is given by the measurement of an electric phase at a certain frequency. The phase angle at this frequency can be expressed by a corresponding time interval, τ, which is the time an RF wave needs for a round trip from the illuminating radar to the target and back. The range to be measured is obtained by multiplying $\frac{\tau}{2}$ by the mean wave propagation velocity. The phase angle in conventional pulse radars, for instance, is measured at the pulse-repetition frequency (PRF). It also can be measured at an IF or at the RF. Assuming a given accuracy in phase measurement, the precision in measuring ranges is proportional to the frequency used. Going up from measuring phases in the PRF to an IF, or to the RF again, almost any desired inherent precision can be reached. With modern equipment an angular precision of a few seconds of arc and a range precision of a few feet can be achieved.

But the accuracy to be reached in actual tracking targets flying in the atmosphere is limited by wave propagation effects, that is, by refraction in the denser atmosphere. Errors in angle and range caused by the uncertainty of the refractive index profile exceeded the inherent precision of a system by up to two orders of magnitude. The system's precision, therefore, could never be fully used. In fact, it is unreasonable to build a system to the highest possible inherent precision, at considerable expenditure, when the accuracy of the final results is much inferior.

The purpose of this paper is to show that in tracking targets beyond the atmosphere this situation no longer exists. The refractive index profile, of course, is still uncertain. The index can be measured at the sites of the electronic system on the surface of the earth, as usual. But now that the index at the target site is also known, it can be shown that it approaches unity to less than 10^{-6} at altitudes beyond 200,000 feet. This is not the case for targets flying in the denser atmosphere. In that case, the refractive index at the target site normally has a high degree of uncertainty and this is the reason for the uncertainty in angular and range errors.

The refractive effects of the ionosphere will not be treated in this paper because it can be shown that these effects are negligible if frequencies in the kilomegacycle range are used. We shall confine our considerations to these higher frequencies because modern high-accuracy tracking systems will, for other reasons, use these frequencies exclusively.

The only other assumption we make is that of a spherically stratified atmosphere concentric with the earth, ne-

* Manuscript received by the PGMIL, July 21, 1959.
† Directorate of Advanced Technology, AF Missile Dev. Center, Holloman AFB, N.M.

glecting horizontal gradients of the refractive index. This assumption must be made, because such gradients along the path of a wave cannot be determined. The azimuthal error limits caused by such gradients will have to be determined by experiment. They are the same as those common to optical measurements in astronomy and are not likely to exceed a few seconds of arc.

The new situation, then, consists of the fact that we now know the refractive index on both ends of the wavepath, at its origin on the earth's surface and at its end on the site of the target. It will be shown that we now can define a family of standard refractive-index profiles, each member of the family starting at a certain index, n_0, on the earth's surface and approaching unity to less than 10^{-6} at 200,000 feet altitude. The errors in angle and range produced by these standard profiles will be computed. Proper correction terms, therefore, can be applied to the corresponding numbers as measured by the tracking radar; consequently we shall call these terms correctable errors or corrections. They do not impair the accuracy of the system; the corrections are based upon measurable data and precise calculations.

The crucial question now arises concerning the magnitude of the noncorrectable errors which originate in the uncertainty of the individual profiles between the known data at the beginning and at the end of the line. In Fig. 1 we see the site of the radar and three positions of a satellite. Of course, the scale of this picture is strongly distorted in order to make clear what we wish to show. It is easy to see that the refractive-index profiles cannot be measured from the radar at point O to all the points S_1, S_2, . . . S_i along a satellite path. The dashed lines indicate three of these propagation ways.

Meteorological measurements are made along a more or less vertical line and each measurement needs a finite time. But the index profile is subject to changes in time and space and therefore it is impossible to cover the entire profile-plane at the proper instants.

We then have to accept the uncertainty of individual profiles and herewith the neglecting of horizontal index gradients, and we have to find out the resulting uncorrectable errors.

In Fig. 2(a), two refractive index profiles have been drawn schematically, representing two extreme weather conditions. The index on the surface of the earth is the same in both cases and the index always approaches unity at 200,000 feet altitude to less than 10^{-6}. At profile 1, the air is almost saturated all the way up to higher altitudes, whereas at profile 2 the air is dry from high altitudes down to the lower atmosphere and the humidity increases rapidly from there to the surface. A similar profile will occur with a temperature inversion in the lower atmosphere. In Fig. 2(b) we see the two schematic wave paths corresponding to the two profiles. Path 1 has a slight curvature corresponding to an over-all low gradient of index vs altitude (profile 1), whereas path 2 has a greater curvature in the lower part

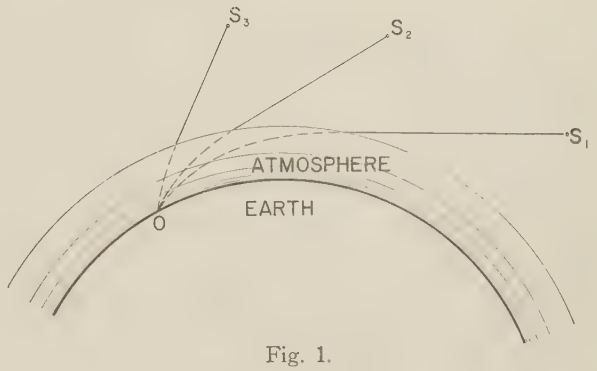

Fig. 1.

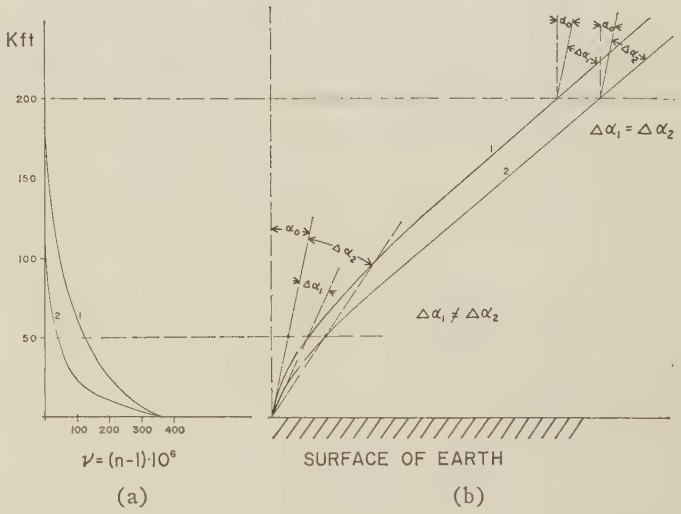

Fig. 2—(a) Refractive index profiles; (b) wave paths corresponding to profiles.

of the atmosphere corresponding to a high index gradient and a very low curvature in the upper atmosphere where the gradient of profile 2 is low. But note that both paths leave the atmosphere beyond 200,000 feet as parallel straight lines. This is the vital point in our investigation. No matter how the distribution of a stratified atmosphere might be, in other words, no matter how an individual profile might be, the wavepaths will always come out parallel beyond the atmosphere. We designate α_0 the zenith-angle measured by the radar. Then $\Delta\alpha_1$ and $\Delta\alpha_2$ at 200,000 feet are the correctable errors which can be precisely computed from information received only on the refractive index measured on the surface (n_0). Both wavepaths are parallel ($\Delta\alpha_1 = \Delta\alpha_2$), which means that the uncorrectable errors are zero for a target at infinity. A real target will not be at infinity but relatively far from an altitude of 200,000 feet. The computation, therefore, will show that the uncorrectable errors decrease with increasing range. It will be seen later that they do not exceed a few seconds of arc in angle and a few feet in range for all practical purposes.

The situation is quite different for targets inside the denser atmosphere (Fig. 2). Assume a target, say, at 50,000 feet altitude. We see that the error angle $\Delta\alpha_1$ is quite different from $\Delta\alpha_2$ for the two profile cases. But the point is that neither $\Delta\alpha_1$ nor $\Delta\alpha_2$ can be computed because the

profiles are not known. In the case of a target inside the atmosphere, therefore, $\Delta\alpha_1$ and $\Delta\alpha_2$ are not corrections, but uncorrectable errors of considerable magnitude. Modern electronic tracking and guidance systems reach an inherent system precision which goes far beyond these uncorrectable errors. The system's capacity, therefore, could not be fully utilized with targets in the atmosphere. But it can be used on targets beyond the denser atmosphere and there is no reason why it should not reach the known accuracy of optical instruments without being biased by their restrictions on clear weather conditions.

Refractive Index Profiles

The index of refraction, n, for microwaves penetrating the atmosphere, is a function of temperature, air pressure, and partial pressure of water vapor, according to:

$$\nu = (n - 1) \times 10^6 = \frac{c}{T}\left(p + \frac{be}{T}\right), \qquad (1)$$

where

$c = 79$ [°K/mb]
T = temp [°K]
p = air pressure [mb]
$b = 4800$ [°K]
e = partial pressure of water vapor [mb]
n = refractive index.

Figs. 3-5 show profiles of refractive index vs altitude (MSL) for medium, very low, and very high indexes at the surface. The very low case (Fig. 4) can only occur at the site of a high mountain. A meteorological sounding from Holloman Air Force Base has been used and the measured data were transferred to the Sacramento Peak (10,148 feet MSL), about ten miles east of Holloman AFB, N.M. The medium case (Fig. 3) was taken at Valparaiso, Fla.

A sounding for the very high case (Fig. 5) was not available. Therefore, its construction has been based upon meteorologically reasonable assumptions of the temperature gradient and the supposition of a very high humidity (75 ÷ 90 per cent) in all altitudes. These conditions may occur some time before the outburst of a tropical thunderstorm.

From measured data of pressure, temperature, water vapor content, and altitude, the profiles were calculated according to (1) and plotted in curves *a*, Figs. 3-5. In all three cases the relative humidity at the surface was 75 per cent, as measured in Valparaiso. In order to obtain profiles *b* and *c*, corresponding to somewhat extreme weather conditions at the same surface index, $\nu_0 = (n_0\text{-}1) \times 10^6$, we assume that at curves *b* the air is saturated at altitudes beyond 1000 feet above the surface while pressure and temperature distribution vs altitude remains the same. In curves *c*, to the contrary, the air is assumed to be extremely dry from high altitudes down to about 1000 feet and to become rapidly humid in a small transition layer from

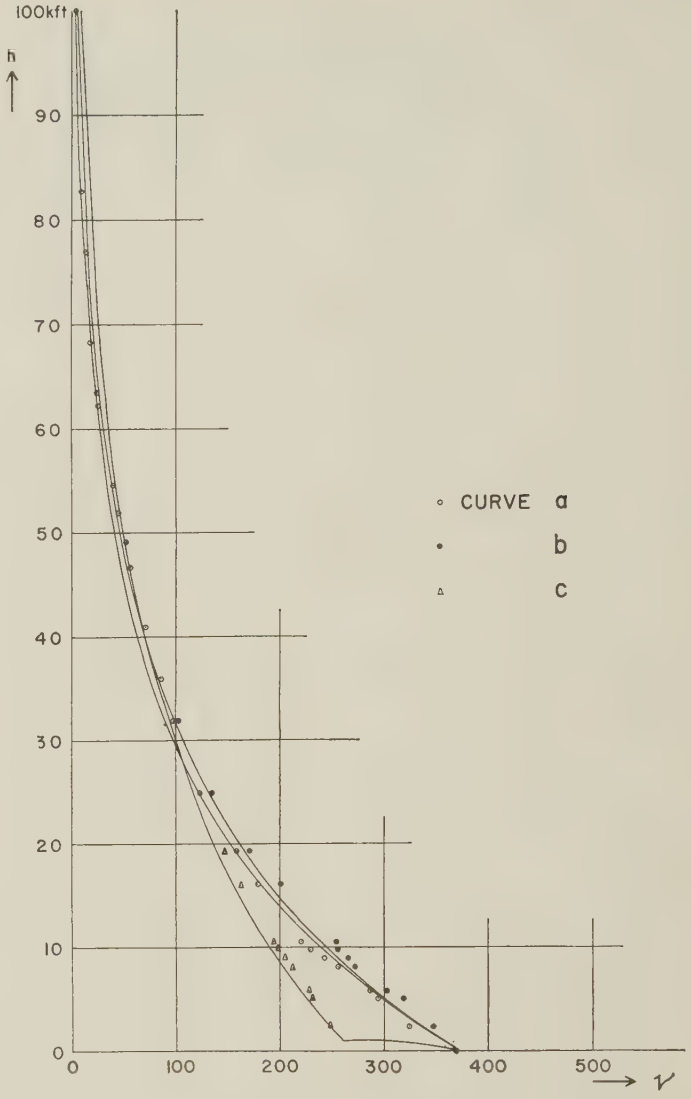

Fig. 3—Refractive index profiles vs altitude: the medium case.

there down, reaching 75 per cent relative humidity at the surface. The same conditions will also occur in case of a temperature inversion between zero and 1000 feet altitude, as shown by (1).

Eq. (1) also shows that at altitudes higher than 50,000 feet, for example, all the profiles n (or ν) vs h will almost coincide independently of time and location because p is small, e is practically zero, and T does not vary noticeably.

A ν profile, as shown in Fig. 5 curve *c*, with such a drastic reduction of humidity in a small transition layer of only 1000 feet near the surface, seems to be meteorologically unrealistic. However, it has been chosen intentionally in order to learn the uncorrectable errors in angle and range caused by two radically different profiles originating at the same surface index.

Curves *a* and *b* in Figs. 3-5 were approximated by exponential functions. Curves *c* were approximated by second-order parabolas in the lower part and by exponential functions in the upper part. The accuracy of these approximations can be seen in the figures.

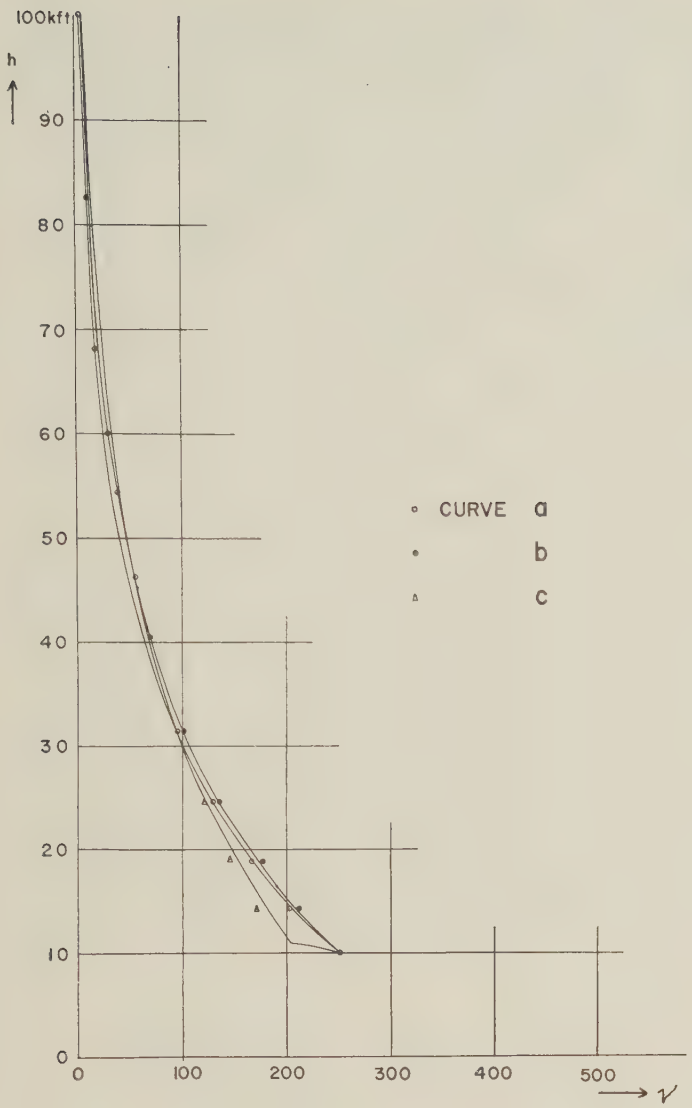

Fig. 4—Refractive index profiles vs altitude: the low case.

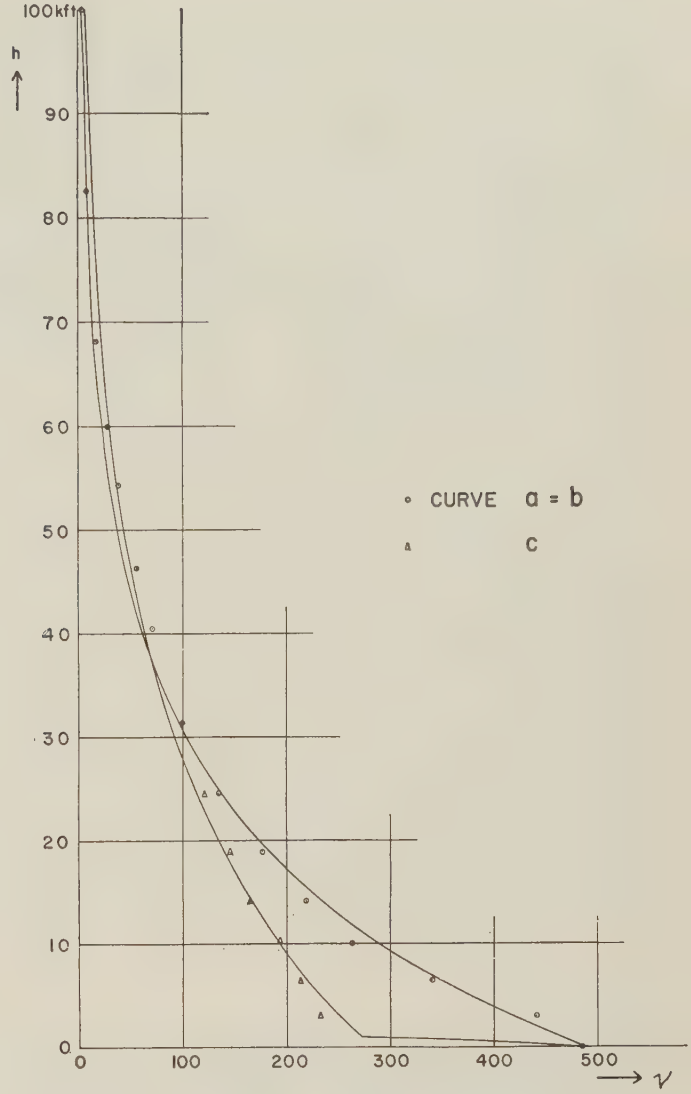

Fig. 5—Refractive index profiles vs altitude: the high case.

At this point, we have to anticipate the results of the computations of angle and range errors made for the eight profiles shown in Figs. 3-5. The theory of these computations will be treated in the next section. Table I shows the values in question (see Fig. 6).

α_a = apparent zenith-angle (81.75°)
s = geometrical range on the curved path
$\nu_0 = (n_0 - 1)10^6$
$\Delta\alpha$ = angle correction
d = real range to the target (4.864×10^6 feet)
s_a = apparent range as measured by the radar on the curved path with apparent velocity $v_a = 299{,}773.1$ [km sec^{-1}]
(propagation velocity in vacuum $c = 299{,}792.9$ [km sec^{-1}])
$\Delta s_a = d - s_a$ = range correction
$\Delta^2\alpha = \Delta\alpha_{(a\text{-curve})} - \Delta\alpha_{(b\text{- or }c\text{-curve})}$ = uncorrectable angle error
$\Delta^2 s_a = \Delta s_{a(a\text{-curve})} - \Delta s_{a(b\text{- or }c\text{-curve})}$ = uncorrectable range error.

Table I shows the uncorrectable angle and range errors ($\Delta^2\alpha$ and $\Delta^2 s_a$) which originate from the fact that since only ν_0 can be measured, it is not known which of the profiles, *a*, *b*, or *c*, may actually prevail. They are two orders of magnitude smaller than the correctable profiles $\Delta\alpha$ and Δs_a.

This fact clearly proves that there is no point in trying to fit meticulously the mathematical expressions, exponential functions and parabolas, to the measured profiles. In other words, the fitting accuracy seen in Figs. 3-5 is of very minor importance. This becomes clear if we note that the uncorrectable errors are very small even though they result from such extremely different profiles as *a*, *b*, and *c*, and are calculated for a zenith angle of almost 82°, *i.e.*, 8° above the horizon.

It is not the uncertainty of the individual profile which is important but the value of ν_0. This means that the way in which intermediate layers are stratified does not substantially affect deviation in angle and range. The important factor is the surface index of refraction, ν_0, and this value must and can be measured accurately at the very instant of

TABLE I

		Curve *a*		Curve *b*		Curve *c*	Curves *a*, *b*, *c*	
$\nu_0=250$ Fig. 4	$\Delta\alpha$	4′ 43.5″		4′ 42.6″		4′ 44.1″	*s-d*	3.8 feet
	$\Delta^2\alpha$		+0.9″		−0.6″			
	Δs_a	282 feet		281.1 feet		282.8 feet		
	$\Delta^2 s_a$		+1.5 feet		−0.2 feet			
$\nu_0=368$ Fig. 3	$\Delta\alpha$	8′ 7.4″		8′ 3.8″		8′10.2″	*s-d*	3.1 feet
	$\Delta^2\alpha$		+3.6″		−2.8″			
	Δs_a	265.4 feet		259.8 feet		268.2 feet		
	$\Delta^2 s_a$		+5.6 feet		−2.8 feet			
$\nu_0=486$ Fig. 5	$\Delta\alpha$	10′ 48.8″		Same as curve *a*		10′57.4″	*s-d*	3.1 feet
	$\Delta 2\alpha$				−8.6″			
	Δs_a	384.8 feet				374.2 feet		
	$\Delta^2 s_a$				+10.6 feet			

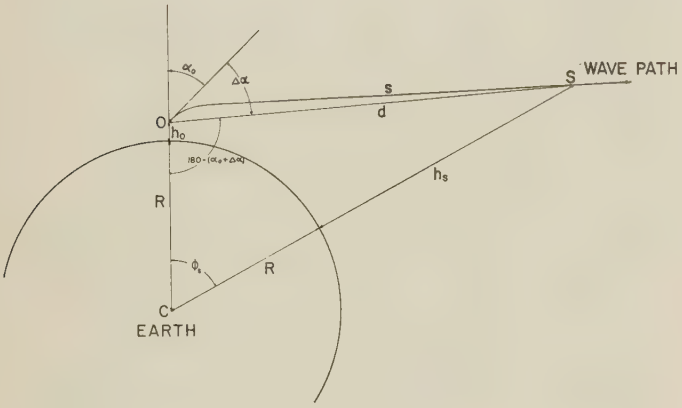

Fig. 6.

the tracking measurements and in the immediate vicinity of the radar.

The vital point of our investigation lies in this fact. It entitled us to introduce "standard" profiles.

Forty-four profiles which were taken at different altitudes (MSL) and seasons have been calculated according to (1). Among these were five individual soundings provided by the U. S. Weather Service. Ten profiles were taken from "Climatic Data for White Sands Missile Area," October, 1958. Twenty-two were taken from "Upper-Air Climatology of the United States," U. S. Department of Commerce, Weather Bureau, T.P. No. 32 (1957).

All profiles taken on the East Coast and in the Continental U.S. and Alaska could easily be approximated by an exponential function. All profiles taken from the coast of the Gulf of Mexico and the Caribbean islands showed a flatter slope of the curve at low altitudes. Nevertheless, in all cases there is a function,

$$\nu = \nu_0 \cdot e^{-h/H}, \text{ that fits the } \nu \text{ profiles.}$$

In plotting values of ν_0 the constant, H, for all the 44 profiles, it was noticed that all points from White Sands (altitude 4000-feet MSL) and all points from coastal locations (altitude 0 to 20 feet) were lying near straight lines, whereas all other points appeared to lie at random. This led to the attempt to reduce all values ν_0 to sea level according to the transformation:

$$\nu = \nu_0 \cdot e^{-(h-h_0)/H} \tag{2}$$

$$\nu = \left(\nu_0 \cdot e^{+h_0/H}\right) \cdot e^{-h/H},$$

$$\nu = \nu_{SL} \cdot e^{-h/H}, \tag{3}$$

$$\nu_0 = \nu_{SL} \cdot e^{-h_0/H} \tag{4}$$

where ν_{SL} is the refractive index reduced to *MSL*,

H = a constant [feet]
h = any altitude in feet above mean sea level (MSL)
h_0 = altitude (*MSL*) of the observation site.

The result is shown in Fig. 7. The dots represent values derived from factual soundings; the crosses are derived from profiles constructed for Figs. 3-5. A smooth curve was then drawn through the points. Five checks for the points farthest from the curve showed that the approximation with the H values given by the curve was better than the originally chosen H indicated by these five farthest points.

Let us define the H values given by the curve (Fig. 7) as "standard."

It will be noted that almost all points lie between the limits $H_{\text{standard}} \pm 1500$ feet. Later, therefore, we shall define the uncorrectable errors, $\Delta^2\alpha$ and $\Delta^2 S_a$, as those which result from a deviation of $\pm$ 1500 from the standard H_{st} value at the same measured ν_0.

From (4) a family of standard curves has been drawn in Fig. 8. For each ν_0 measured at a station of altitude h_0 (MSL) the proper H value can be found by interpolating between the curves of parameter H. ν_{S_L} is found in the intersection of the proper H curve with the axis of abscissa.

Computation of Angle and Range Correction

General Equations

The deviation of microwave propagation from a straight line in passing through the atmosphere can be calculated by Snell's law of refraction. In its original form it holds only for the special case of plane surfaces:

$$\frac{\sin\alpha}{\sin\alpha_0} = \frac{n_0}{n}. \tag{5}$$

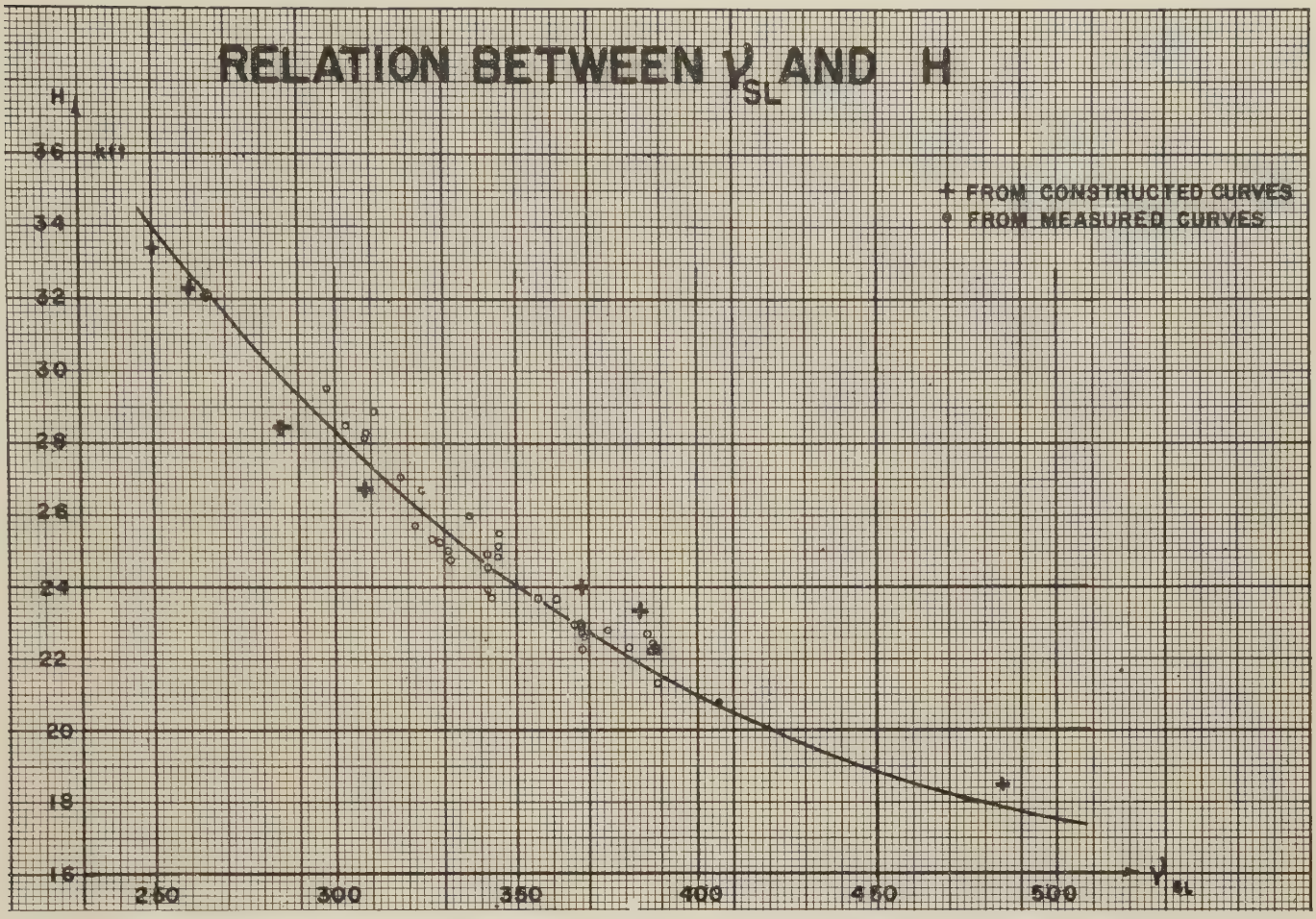

Fig. 7.

For our purposes it has to be generalized to apply to media with curved surfaces. This derivation has been made by Knothe,[1] and independently by Dixon,[2] who stated from Fermat's law and arrived at the same results:

$$\frac{\sin\alpha}{\sin\alpha_0} = \frac{R+h_0}{R+h}\cdot\frac{n_0}{n}\cdot \quad \text{(See Fig. 6.)} \qquad (6)$$

It can be seen immediately that the general law (6) reduces to (5) if the radii of curvature $R + h_0$ and $R + h$ approach infinity, their differences remaining finite, which means the plane case.

Any electronic range measurement between points O and S (Fig. 6) basically consists of the measurement of a phase; it may be an RF phase, an IF phase, or a PRF phase. In conventional pulse-radars, for instance, the electronic phase angle is the PRF, which occurs between the illuminating transmitter pulses and the pulses reflected from a target is measured. At a known frequency the phase angle can be expressed by a corresponding time interval, τ, which is the time for a round trip of a wavefront from the radar to the target and back. The one-way trip, therefore, needs $\frac{\tau}{2}$. The distance to be measured is obtained by multiplying $\frac{\tau}{2}$ by the mean signal propagation velocity, v. The propagation velocity v is not known exactly; it is a function of the refractive index along the path

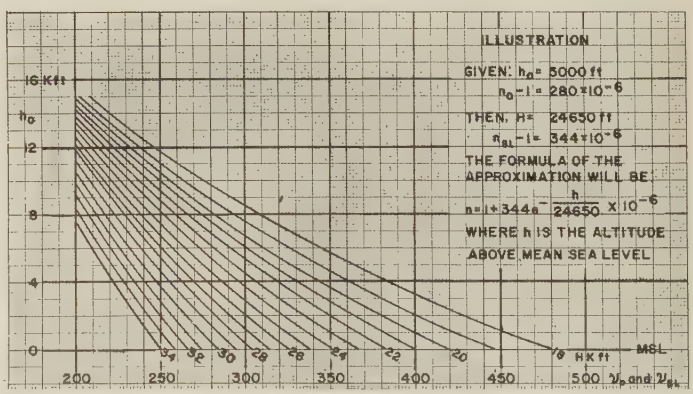

Fig. 8—Graph for the determination of V_{SL} and H for standardized curves if h_0 and Y_0 *are given.*

[1] P. von Handel and H. Knothe, "The Curvature of Microwave Propagation Through the Troposphere and the Ionospheric Layers," Holloman Air Dev. Center, Tech. Rept. No. 3; January, 1956.

[2] H. M. Dixon, "Study of Refraction Errors in Radar Propagation," White Sands Signal Corps Agency, Tech. Rept. 18A; April, 1956.

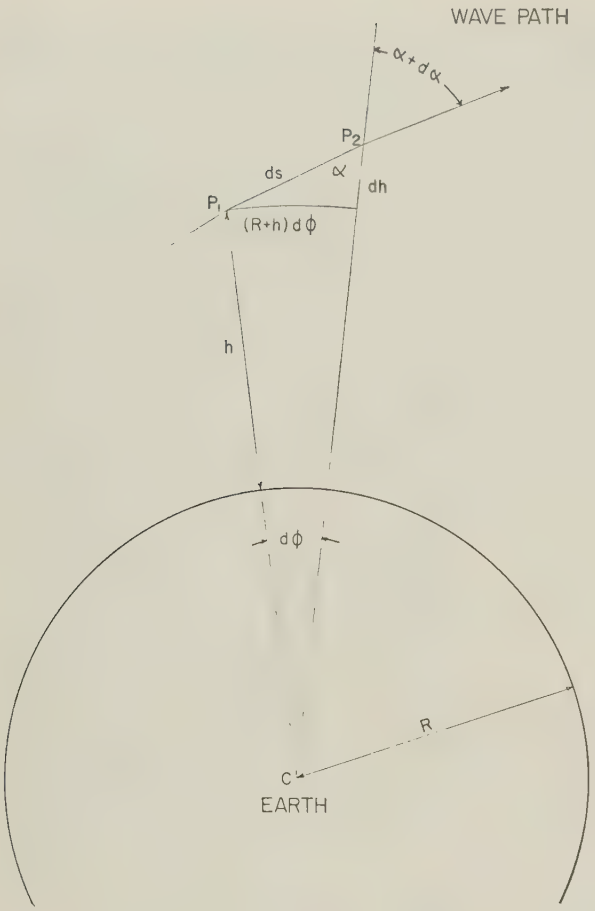

Fig. 9.

and is subject to our calculations. Each electronic system, therefore, has a certain apparent velocity, v_a, which is calibrated to the instrument as a constant. The measured value of range, indicated by the radar system, is an apparent range, s_a. It is a fictitious range which a wavefront would transverse if propagated with constant velocity, v_a, along a path s (Fig. 6).

$$s_a = \frac{\tau}{2} \cdot v_a. \tag{7}$$

With s_a measured and v_a known ($v_a = 299{,}773.1$ km), we have $\frac{\tau}{2}$.

Next, we have to determine the range s along the curved path. We note the well-known expression for the propagation velocity in a medium with refractive index, n:

$$v = \frac{c}{\sqrt{\epsilon\mu}} = \frac{c}{n}. \tag{8}$$

It follows from Fig. 9 that

$$ds = \frac{dh}{\cos\alpha}, \tag{9}$$

and we obtain from (6):

$$\cos\alpha = \left[1 - \sin^2\alpha_0 \left(\frac{R+h_0}{R+h}\right)^2 \left(\frac{n_0}{n}\right)^2\right]^{1/2}. \tag{10}$$

Substituting (10) in (9), we obtain:

$$s = \int_{h_0}^{h_s} \frac{n(R+h)}{[n^2(R+h)^2 - n_0^2(R+h_0)^2\sin^2\alpha_0]^{1/2}} \cdot dh, \tag{11}$$

s is the geometrical range on the curved path (see Fig. 6). The real range we are seeking is d, the path on a straight line. We shall calculate it later.

Meanwhile, we have to find a way to compute the altitude of the satellite, h_s, which is still unknown in (11).

According to (8), we have:

$$ds = v \cdot dt = \frac{c}{n}\, dt, \tag{12}$$

and combining (12) and (11), we find:

$$dt = \frac{n^2(R+h)}{c[n^2(R+h)^2 - n_0^2(R+h_0)^2\sin^2\alpha_0]^{1/2}} \cdot dh$$

and

$$\frac{\tau}{2} = \frac{1}{c}\int_{h_0}^{h_s} \frac{n^2(R+h)}{[n^2(R+h)^2 - n_0^2(R+h_0)^2\sin^2\alpha_0]^{1/2}} \cdot dh. \tag{13}$$

From (13) we find h_s by methods of numerical integration on an electronic computer.[3] All the other values are known: $\frac{\tau}{2}$ is measured [see (7)] and n can be found from (2) and (3):

$$n = 1 + (n_0 - 1)e^{-(h-h_0)/H},$$

where H is determined by Fig. 8 for a measured n_0 and a known h_0. With h_s now known, we find s from (11).

Next, we have to determine the geometrical distance, d, (Fig. 6) that is the real range to the target.

Applying the law of cosines of plane trigonometry, we find:

$$d = [(R+h_0)^2 + (R+h_s)^2 - 2(R+h_0)(R+h_s)\cos\phi_s]^{1/2}. \tag{14}$$

In this equation ϕ_s is still unknown. In order to find ϕ as a function of any altitude, h, we proceed as follows. It can be seen from Fig. 9 that

$$d\phi = \frac{\tan\alpha \cdot dh}{R+h}. \tag{15}$$

Eliminating α from (15) and (6), we obtain:

[3] All integrals have been calculated on a Remington Rand 1103A Univac Scientific.

$$|\phi_s| = \int_{h_0}^{h_s} \frac{n_0(R + h_0) \sin \alpha_0}{(R + h)\lfloor n^2(R + h)^2 - n_0^2(R + h_0)^2 \sin^2 \alpha_0 \rfloor^{1/2}} \cdot dh, \tag{16}$$

d can now be calculated from (14).

Finally, we want to determine the correction in range, Δs_a, which has to be added to the apparent range, s_a, measured on the radar in order to obtain the real range d. From (7) and (14), we find:

$$\Delta s_a = d - s_a = [(R + h_0)^2 + (R + h_s)^2 - 2(R + h_0)(R + h_s) \cos \phi_s]^{1/2} - \frac{\tau}{2} v_a. \tag{17}$$

The correction in angle, $\Delta\alpha$, can readily be found in applying the law of sines (see Fig. 6):

$$\sin (\alpha_0 + \Delta\alpha) = \frac{R + h_s}{d} \sin \phi_s$$

and

$$\Delta\alpha = \sin^{-1}\left(\frac{R + h_s}{d} \sin \alpha_s\right) - \alpha_0. \tag{18}$$

Computations

In all practical cases of tracking space vehicles, the following values are known from measurements:

v_a = the propagation velocity calibrated with the radar
h_0 = elevation of observation site [feet, MSL]
R = 20, 891, 110 [feet] radius of the earth (sphere of equal volume)
$n_0 = 1 + \nu_0 \times 10^{-6}$ = refractive index at the site of the radar antenna
α_0 = apparent zenith angle as measured by radar
s_a = apparent range as measured by radar
H and ν_{SL} from Fig. 9; ν from (3)
c = propagation velocity in vacuum.

According to (7), we obtain

$$\frac{\tau}{2} = \frac{s_a}{v_a}$$

and solving (13), we find h_s by methods of numerical integration. Next, we solve (16) obtaining ϕ_s and then (14) finding the true distance d. Finally, we determine the correction for range by (17) and the correction for angle by (18).

In fact, a somewhat different course of computation has been used. We assumed the values of

$$n_0 = \left(\frac{c}{v_a}\right),\ h_0,\ R,\ \alpha_0,\ H,\ \nu_{SL},\ \nu = \nu_{SL} \cdot e^{-h/H},$$

and s to be given. From these values, h_s was calculated from (11) and $c\frac{\tau}{2} = \sigma$ from (13), ϕ_s from (16), d from (14) and, finally, $\Delta\alpha$ and Δs_a from (18) and (17).

This procedure enabled us to make some checks on the computational results, such as the respective values of d, s, and σ, the magnitude of which must lie in this sequence whereas the difference s-d must be smaller than σ-s. Furthermore, for any set of ν_0 and α_0, σ-s is constant and s-d must increase with increasing s. The latter values must decrease with decreasing α_0.

Eq. (11) has been approximated by step-by-step integration according to Weddel's rule with steps of width $\Delta h = 2; 4; 8; 16; 32$; and 64 feet, and 1620 steps in each case. This led to an altitude $h_r = 204{,}120$ feet and a corresponding s_r. From here on $n = 1$ and the rest of the integral can be written explicitly; h_s can then be calculated from:

$$h_s = [(s - s_r)^2 + 2(s - s_r)\sqrt{A} + (R + h_r)^2]^{1/2} - R,$$

where

$$A = (R + h_r)^2 - n_0^2(R + h_0)^2 \sin^2 \alpha \doteq$$

Eq. (13) was rewritten:

$$c\frac{\tau}{2} = \sigma = \int_{h_0}^{h_s} \cdot$$

This integral was calculated by the same method as (11) and in the same sequence and width of steps. Analogously, we define σ_r to be the value of σ at altitude h_r, and we obtain $\sigma = \sigma_r + (s - s_r)$ because if $n = 1$, the integrals in (13) and (11) are identical.

Eq. (16) was also integrated with the same procedure up to $h_r = 204{,}120$ feet and the corresponding value ϕ_r at that altitude. The explicit integration gives:

$$\phi_s = \phi_r + \left[\cos^{-1}\frac{n_0(R + h_0) \sin \alpha_0}{R + h_s} - \cos^{-1}\frac{n_0(R + h_0) \sin \alpha_0}{R + h_r}\right].$$

Eqs. (14), (17), and (18) were calculated straightforwardly. No random errors could be found to an accuracy of 0.001 foot and 0.001 second of arc. However, systematical errors, originating in the computer capacity, may occur. Therefore, the values of Δs_a and $\Delta\alpha$ listed in Table II should be considered accurate to two units in the last decimal. These values were calculated for the following parameters:

$$\alpha_0 = 87.5°; 85°; 80°; 70°; 50° \text{ and } 10°$$
$$s \times 10^{-6}[\text{feet}] = 5; 4.5; 4; 3.5; 3.0; 2.5; 2.0; 1.5; 1.0$$
$$\nu_0 = 400; 370; 340; 310; 280$$
$$H[\text{feet}] = H_{st} - 1500; H_{st}; H_{st} + 1500$$
$$h_0[\text{feet}] = 0.$$

TABLE II(a)

ν_0	$s\times10^{-6}$ feet	$\alpha_0=87.5°$ $\Delta\alpha$ (min)	$\Delta\alpha$ (sec)	$\Delta^2\alpha$ (sec)	$\alpha_0=85°$ $\Delta\alpha$ (min)	$\Delta\alpha$ (sec)	$\Delta^2\alpha$ (sec)	$\alpha_0=80°$ $\Delta\alpha$ (min)	$\Delta\alpha$ (sec)	$\Delta^2\alpha$ (sec)	$\alpha_0=70°$ $\Delta\alpha$ (min)	$\Delta\alpha$ (sec)	$\Delta^2\alpha$ (sec)	$\alpha_0=50°$ $\Delta\alpha$ (min)	$\Delta\alpha$ (sec)	$\Delta^2\alpha$ (sec)	$\alpha_0=10°$ $\Delta\alpha$ (sec)	$\Delta^2\alpha$ (sec)
400	5	23	9.9	26.5	13	48.8	7.7	7	25.1	1.7	3	42.2	0.4	1	37.4	0.1	14.45	0.01
	4.5	22	59.2	27.0	13	41.2	7.9	7	24.0	1.8	3	41.8	0.4	1	37.3	0.1	14.45	0.01
	4	22	45.8	27.4	13	39.8	8.1	7	22.4	1.9	3	41.5	0.4	1	37.2	0.1	14.44	0.01
	3.5	22	28.4	28.0	13	33.2	8.5	7	20.4	1.9	3	40.7	0.4	1	37.1	0.1	14.42	0.01
	3	22	5.2	28.6	13	24.4	8.9	7	17.7	2.1	3	40.2	0.5	1	36.9	0.1	14.42	0.01
	2.5	21	32.3	30.0	13	12.0	9.6	7	14.0	2.3	3	39.1	0.6	1	36.6	0.2	14.39	0.01
	2	—	—	—	12	53.3	10.5	7	8.3	2.7	3	37.5	0.6	1	36.2	0.1	14.36	0.02
	1.5	—	—	—	—	—	—	6	58.7	3.3	3	34.9	0.8	1	35.5	0.2	14.30	0.02
	1	—	—	—	—	—	—	—	—	—	3	29.7	1.0	1	34.3	0.3	14.22	0.03
370	5	20	53.5	22.6	12	37.3	6.8	6	49.7	1.5	3	25.1	0.3	1	30.0	0.1	13.36	0.01
	4.5	20	43.3	22.9	12	33.3	7.0	6	48.5	1.6	3	24.8	0.3	1	29.9	0.1	13.36	0.01
	4	20	30.5	23.3	12	28.4	7.2	6	47.0	1.7	3	24.4	0.3	1	29.8	0.1	13.35	0.01
	3.5	20	13.9	23.8	12	22.0	7.5	6	45.0	1.8	3	23.9	0.4	1	29.7	0.1	13.33	0.01
	3	19	51.6	24.6	12	13.3	7.9	6	42.3	1.9	3	23.2	0.4	1	29.5	0.1	13.32	0.01
	2.5	19	20.1	25.6	12	1.1	8.5	6	38.6	2.1	3	22.1	0.5	1	29.3	0.1	13.30	0.01
	2	—	—	—	11	42.7	9.5	6	32.9	2.5	3	20.5	0.6	1	28.8	0.1	13.26	0.01
	1.5	—	—	—	—	—	—	6	23.4	3.0	3	17.8	0.7	1	28.2	0.2	13.21	0.01
	1	—	—	—	—	—	—	—	—	—	3	12.2	1.0	1	26.9	0.2	13.13	0.02
340	5	18	42.1	19.0	11	26.8	5.9	6	14.5	1.4	3	8.1	0.3	1	22.6	0.1	12.27	0.01
	4.5	18	32.4	19.3	11	22.9	6.2	6	13.3	1.4	3	7.8	0.3	1	22.6	0.1	12.27	0.01
	4	18	20.1	19.8	11	18.1	6.4	6	11.8	1.5	3	7.4	0.4	1	22.5	0.1	12.26	0.01
	3.5	18	4.4	20.1	11	11.8	6.7	6	9.8	1.6	3	6.8	0.4	1	22.4	0.1	12.24	0.01
	3	17	43.1	20.8	11	3.3	7.0	6	7.1	1.8	3	6.1	0.4	1	22.1	0.1	12.23	0.01
	2.5	17	13.2	21.7	10	51.5	7.5	6	3.4	2.0	3	5.1	0.5	1	21.9	0.1	12.21	0.01
	2	—	—	—	10	33.5	8.3	5	57.8	2.2	3	3.4	0.6	1	21.5	0.2	12.17	0.01
	1.5	—	—	—	—	—	—	5	48.4	2.7	3	0.8	0.6	1	20.8	0.2	12.12	0.02
	1	—	—	—	—	—	—	—	—	—	2	55.6	0.9	1	19.5	0.2	12.04	0.02
310	5	16	32.4	15.8	10	16.4	5.2	5	39.1	1.3	2	51.0	0.3	1	15.3	0.1	11.18	0.01
	4.5	16	23.2	16.0	10	12.7	5.3	5	38.0	1.3	2	50.7	0.3	1	15.2	0.1	11.17	0.01
	4	16	11.6	16.3	10	8.0	5.5	5	36.5	1.3	2	50.3	0.3	1	15.1	0.1	11.17	0.01
	3.5	15	56.6	16.7	10	1.8	5.8	5	34.5	1.5	2	49.8	0.3	1	15.0	0.1	11.15	0.01
	3	15	36.5	17.2	9	53.5	6.1	5	31.9	1.6	2	49.1	0.4	1	14.7	0.1	11.14	0.01
	2.5	15	8.1	17.9	9	41.9	6.5	5	28.2	1.7	2	48.0	0.4	1	14.5	0.1	11.12	0.01
	2	—	—	—	9	24.4	7.1	5	22.5	2.1	2	46.4	0.5	1	14.1	0.1	11.08	0.01
	1.5	—	—	—	—	—	—	5	13.2	2.4	2	43.7	0.6	1	13.4	0.1	11.02	0.02
	1	—	—	—	—	—	—	—	—	—	2	38.5	0.8	1	12.1	0.2	10.95	0.02
280	5	14	26.0	12.8	9	6.5	4.4	5	3.9	1.1	2	34.0	0.3	1	7.9	0.1	10.09	0.01
	4.5	14	17.3	13.0	9	2.9	4.5	5	2.7	1.1	2	33.6	0.3	1	7.8	0.1	10.08	0.01
	4	14	6.4	13.2	8	58.3	4.6	5	1.2	1.2	2	33.2	0.3	1	7.7	0.1	10.08	0.01
	3.5	13	52.2	13.6	8	52.3	4.9	4	59.2	1.3	2	32.7	0.3	1	7.6	0.1	10.06	0.01
	3	13	33.1	14.1	8	44.3	5.2	4	56.6	1.4	2	32.0	0.3	1	7.3	0.1	10.05	0.01
	2.5	13	6.3	14.6	8	33.0	5.5	4	52.9	1.6	2	30.9	0.4	1	7.1	0.1	10.03	0.01
	2	—	—	—	8	15.9	6.1	4	47.4	1.7	2	29.3	0.4	1	6.7	0.1	9.99	0.01
	1.5	—	—	—	—	—	—	4	38.0	2.2	2	26.7	0.6	1	6.0	0.1	9.93	0.01
	1	—	—	—	—	—	—	—	—	—	2	21.4	0.8	1	4.7	0.2	9.86	0.02

In all the calculations, it was required that $h_s \geqq 210{,}000$ feet in order to be sure that the target is outside the denser atmosphere.

The differences of the values $\Delta\alpha$ and Δs_a calculated for the three different values of H are denominated $\Delta^2\alpha$ and $\Delta^2 s_a$, respectively, and represent the uncorrectable errors caused by the uncertainty of an individual refractive index profile. These values are of considerably higher accuracy than $\Delta\alpha$ and Δs_a because the possible systematical errors are vanishing as well as the random ones. The values $\Delta^2\alpha$ and $\Delta^2 s_a$, listed in Table II, always represent the larger error in case the differences for $H_{st} \pm 1500$ feet should not be equal.

Accuracy Limits of Electronic Tracking

From Table II(a) it can be noted that considerable angular corrections, $\Delta\alpha$, must be applied specifically at large zenith angles, large distances, and large refractive indices. These corrections reach values up to more than twenty minutes of arc at an $\alpha_0 \cong 87°$. At zenith angles of $\alpha_0 = 85°$ they decrease to about ten minutes of arc, and around $\alpha_0 = 40°$ they diminish to less than one minute of arc. But even at $\alpha_0 = 10°$ from zenith they still amount to about 10 to 15 seconds of arc, which certainly is not negligible if the inherent accuracy of the system is better than two seconds.

The uncorrectable errors, $\Delta^2\alpha$, on the other hand, increase with decreasing range. The influence of α_0 and ν_0 on $\Delta^2\alpha$, however, is the same as on $\Delta\alpha$. These uncorrectable errors are of somewhat alarming magnitude (up to ½ minute of arc at $\alpha_0 = 87.5°$, $\nu_0 = 400$, and $s = 2.5 \times 10^6$ feet) for targets just appearing above the horizon. But $\Delta^2\alpha$ decreases rapidly from there and is down to about two or three seconds of arc at $\alpha_0 = 80°$, down to less

TABLE II(b)

ν_0	$s\times10^{-6}$ feet	$\alpha_0=87.5°$		$\alpha_0=85°$		$\alpha_0=80°$		$\alpha_0=70°$		$\alpha_0=50°$		$\alpha_0=10°$	
		Δs_a feet	$\Delta^2 s_a$ feet	Δs_a feet	$\Delta^2 s_a$ feet	Δs_a feet	$\Delta^2 s_a$ feet	Δs_a feet	$\Delta^2 s_a$ feet	Δs_a feet	$\Delta^2 s_a$ feet	Δs_a feet	$\Delta^2 s_a$ feet
400	5	168.6	8.7	235.5	5.8	278.3	3.3	302.0	1.7	314.7	0.9	321.1	0.6
	4.5	135.8	8.6	202.5	5.8	245.4	3.3	269.2	1.8	281.8	0.9	288.1	0.6
	4	103.1	8.6	169.6	5.8	212.6	3.3	236.3	1.8	249.1	1.0	255.2	0.6
	3.5	70.2	8.7	136.8	5.8	179.8	3.3	203.5	1.7	216.2	1.0	222.2	0.7
	3	37.4	8.7	104.1	5.8	147.0	3.3	170.7	1.7	183.3	1.0	189.1	0.6
	2.5	4.7	8.7	71.3	5.8	114.3	3.3	138.1	1.8	150.4	0.9	156.1	0.6
	2	—	—	38.8	5.8	81.7	3.3	105.3	1.8	117.5	1.0	123.1	0.6
	1.5	—	—	—	—	49.2	3.3	72.7	1.8	84.7	1.0	90.2	0.6
	1	—	—	—	—	—	—	40.3	1.7	52.2	1.0	57.3	0.7
370	5	171.7	7.8	235.0	5.3	278.3	3.0	301.9	1.6	314.6	0.9	321.1	0.6
	4.5	138.9	7.8	203.0	5.3	245.3	3.0	269.1	1.6	281.7	0.9	288.1	0.6
	4	106.1	7.8	170.1	5.3	212.5	3.0	236.2	1.6	249.0	0.9	255.1	0.6
	3.5	73.3	7.8	137.3	5.3	179.7	3.0	203.4	1.6	216.2	0.9	222.1	0.6
	3	40.4	7.8	104.6	5.3	147.0	3.0	170.6	1.6	183.3	0.9	189.1	0.6
	2.5	7.6	7.8	71.8	5.3	114.3	3.0	138.0	1.6	150.3	0.9	156.1	0.6
	2	—	—	39.3	5.3	81.6	3.1	105.3	1.6	117.4	0.9	123.1	0.6
	1.5	—	—	—	—	49.1	3.0	72.7	1.6	84.6	0.9	90.1	0.6
	1	—	—	—	—	—	—	40.2	1.6	52.1	0.9	57.3	0.6
340	5	175.5	6.9	236.9	4.8	278.4	2.8	301.9	1.5	314.6	0.8	321.1	0.5
	4.5	142.6	7.0	204.0	4.8	245.5	2.8	269.1	1.5	281.7	0.8	288.1	0.5
	4	109.8	7.0	171.1	4.8	212.7	2.8	236.2	1.5	249.0	0.8	255.1	0.6
	3.5	77.1	7.0	138.3	4.8	179.9	2.8	203.5	1.5	216.2	0.8	222.1	0.5
	3	44.2	6.9	105.4	4.8	147.0	2.8	170.6	1.5	183.3	0.8	189.1	0.5
	2.5	11.4	6.9	72.8	4.8	114.4	2.8	138.0	1.5	150.3	0.8	156.1	0.5
	2	—	—	40.3	4.8	81.9	2.8	105.3	1.5	117.4	0.8	123.1	0.6
	1.5	—	—	—	—	49.3	2.8	72.7	1.5	84.6	0.8	90.1	0.5
	1	—	—	—	—	—	—	40.2	1.5	52.1	0.8	57.3	0.5
310	5	178.8	6.1	237.5	4.3	278.5	2.5	301.8	1.3	314.5	0.7	321.0	0.5
	4.5	145.9	6.2	204.6	4.3	245.5	2.5	269.0	1.3	281.7	0.7	288.0	0.5
	4	113.2	6.2	171.7	4.3	212.6	2.5	236.1	1.4	249.0	0.8	255.1	0.5
	3.5	80.4	6.1	138.9	4.3	179.8	2.5	203.4	1.4	216.1	0.7	222.1	0.5
	3	47.6	6.1	106.0	4.3	147.1	2.5	170.5	1.4	183.2	0.7	189.1	0.5
	2.5	14.8	6.1	73.4	4.3	114.3	2.5	137.9	1.3	150.3	0.8	156.0	0.5
	2	—	—	40.9	4.3	81.8	2.5	105.2	1.3	117.4	0.8	123.0	0.5
	1.5	—	—	—	—	49.3	2.5	72.6	1.4	84.5	0.8	90.1	0.5
	1	—	—	—	—	—	—	40.1	1.4	52.0	0.7	57.3	0.5
280	5	182.3	5.3	238.2	3.8	278.3	2.3	301.7	1.2	314.5	0.7	321.0	0.4
	4.5	149.5	5.3	205.2	3.8	245.4	2.2	268.9	1.2	281.6	0.7	288.0	0.5
	4	116.7	5.3	172.3	3.8	212.6	2.2	235.9	1.2	248.9	0.7	255.0	0.5
	3.5	83.8	5.4	139.5	3.8	179.8	2.2	203.2	1.2	216.1	0.7	222.0	0.4
	3	51.0	5.4	106.7	3.8	147.0	2.3	170.4	1.2	183.1	0.7	189.0	0.4
	2.5	18.2	5.4	74.0	3.8	114.3	2.3	137.8	1.2	150.2	0.6	156.0	0.4
	2	—	—	41.4	3.8	81.7	2.2	105.0	1.2	117.3	0.7	122.9	0.5
	1.5	—	—	—	—	49.2	2.2	72.4	1.2	84.5	0.7	90.0	0.4
	1	—	—	—	—	—	—	40.0	1.2	51.9	0.7	57.2	0.4

than one second at $\alpha_0 = 70°$, and down to about one hundredth of a second at $\alpha_0 = 10°$. This means that we reach the inherent precision of high accurate radar systems already at angles $\alpha_0 \leq 80°$.

Table II(b) shows the range correction, Δs_a, and the uncorrectable range errors, $\Delta^2 s_a$. Let us first discuss the errors, $\Delta^2 s_a$. They depend only on α_0 and ν_0 and are independent of the range, s. At large zenith angles α_0 and large refractive indexes ν_0 they reach a magnitude of almost ten feet; at $\alpha_0 = 0°$ to $50°$ they amount to about one foot, and diminish to about one half foot at zenith.

The range corrections, Δs_a, on the other hand, increase with decreasing α_0. For angles $\alpha_0 \leq 80°$ the values are practically independent of ν_0. They increase with increasing range. At a first glance, it may be surprising that, contrary to the family of $\Delta\alpha$ curves (Fig. 10), the corrections Δs_a (Fig. 11) increase with decreasing α_0 and with increasing distance, d. This is because the apparent propagation velocity, v_a, calibrated to the radar as a constant, was 299,733.1 km in our case and all calculations in this paper have been based upon this figure. If another constant v_a had been calibrated into a specific radar, the respective number would have to be changed in (7) and (17). If, for instance, light velocity in vacuum ($c = 299{,}792.9$ km) had been used for v_a, then the family of curves on the left side of Fig. 11 would show increasing errors Δs_a with increasing α_0 and decreasing d.

Here again, it can be seen that the range corrections, Δs_a, are in the order of a few hundred feet and must be allowed for if accurate data are expected.

The exact results of our computations can only be seen from Table II(a) and (b). In order to enable a general survey on trends of $\Delta\alpha$, $\Delta^2\alpha$, Δs_a, and $\Delta^2 s_a$, the content of Table II(a) and (b) has been plotted in Figs. 10 and 11, respectively. Exact values, of course, cannot be determined from these figures because they lie below the drawing

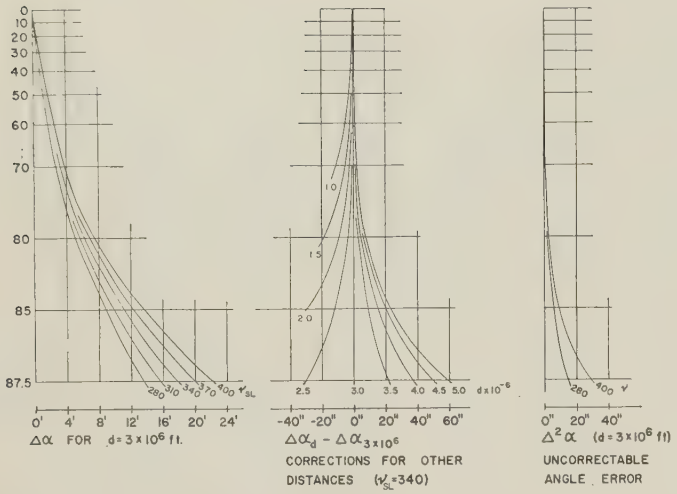

Fig. 10—Angle corrections.

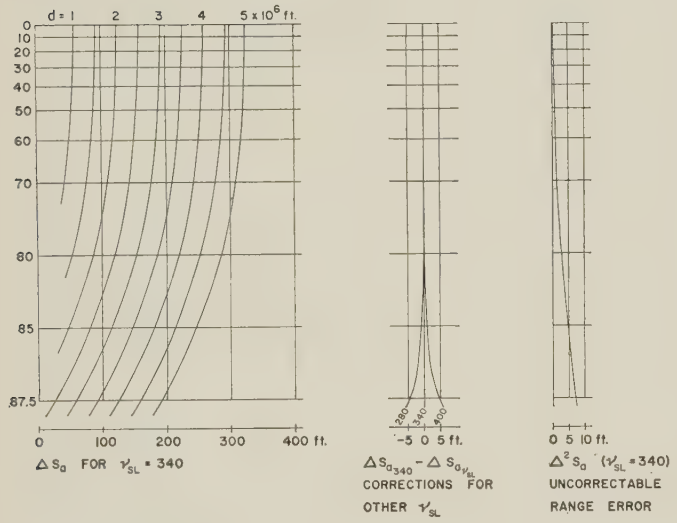

Fig. 11—Range corrections.

accuracy. The ordinate in both figures is α_0. Precisely, the curves in the middle of Fig. 10 split up appreciably in their lower part ($\alpha_0 > 80°$) for values of $\nu_{SL} \neq 340$, as can be seen by comparison with Table II(a). These divergences, however, have been omitted to keep the figure readable. The same is true for the right-hand part of Fig. 10, where the curves of $\Delta^2\alpha$ also diverge with d in the lower part. The same is true for the right-hand part of Fig. 11, where $\Delta^2 s_\alpha$ depends on ν_{SL}.

Remarks on Optical Tracking

From the previous paragraphs we have learned that range must be introduced to add further angular corrections. The same thing, of course, is true for optical tracking of satellities. In Fig. 12 the configuration is shown schematically. A satellite, S', appears in coincidence with a star, $\bigstar'$, under a zenith-angle α_0. The true position of the satellite is indicated at S and the true direction to the star is shown at $\bigstar$. It is easy to see that the correction angles $\Delta\alpha_s$ and $\Delta\alpha_\bigstar$, respectively, are not equal. They diverge

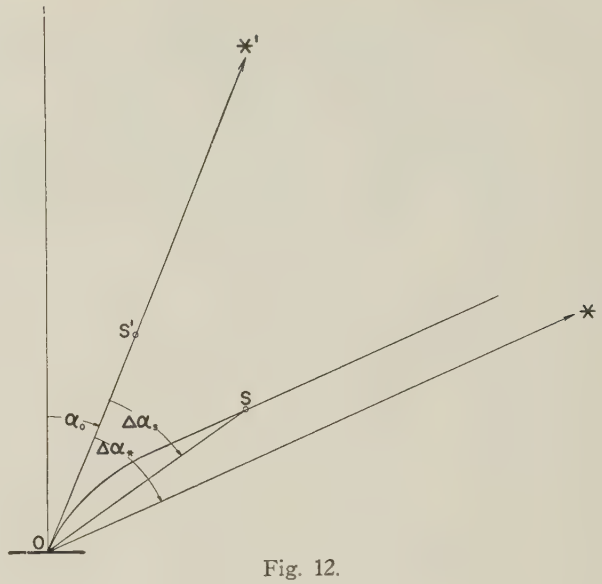

Fig. 12.

increasingly with decreasing range of the satellite. $\Delta\alpha_\bigstar$ is the normal astronomical refractive correction. In order to obtain a better correction, we have to subtract $(\Delta\alpha_\bigstar - \Delta\alpha_s)$ from $\Delta\alpha_\bigstar$. The remaining uncertainty caused by the uncertainty of individual profiles is characterized by $\Delta^2\alpha$ in Table II(a). It is the same as for electronic tracking.

Table III shows the necessary corrections $\Delta\alpha_\bigstar - \Delta\alpha_s$ dependent on α_0 and d.

TABLE III
Optical Corrections

d \ α_0	$\Delta\alpha\bigstar - \Delta\alpha_s$ in sec of arc 10°	50°	70°	80°
1.10^6 feet	0.33	4.0	17.1	—
2.10^6	0.20	2.2	9.3	39.9
3.10^6	0.14	1.5	6.6	30.6
4.10^6	0.11	1.1	5.3	25.9
5.10^6	0.10	1.0	4.6	23.2

Conclusions

We have found that angular accuracies of a few seconds of arc and range accuracies of less than ten feet can be reached in electronic tracking of satellites. This precision can be obtained by measuring only the refractive index at the radar site without any knowledge of the course of an individual index-profile along the way of propagation. The accuracy limits caused by wave propagation effects reach the inherent precision of high accurate radar systems already at 20° above horizon ($\alpha_0 \leq 80°$) if the range to the target is larger than 3 million feet. Therefore, it will now be profitable to put a new emphasis on developing electronic systems with high inherent precision. In both the electronic and the optical tracking procedures range must be known in order to introduce accurate angular corrections. In this case, the same accuracy limits are reached electronically and optically.

Some Reliability Aspects of Weapon and Other Space Systems Using Ballistic Missile Boosters*

HENRY TRIWUSH†

Summary—**This paper shows that there is a need to differentiate, at least on occasion, between weapon and nonweapon space systems where their reliability is concerned. Three criteria are offered as a means of determining whether this differentiation need be made in the case of any particular nonweapon space system. Where this differentiation should be made, possible reliability approaches for the nonweapon space system are suggested.**

Introduction

"RELIABILITY is everybody's business." This well-known platitude is often only the preamble to such witticisms as "And what's everybody's business turns out to be nobody's business." But let us consider it seriously. The fact is, where weapon and other space systems are concerned, reliability *is* everybody's business because of these systems' costs, complexities, and national importance. "Everybody" includes both technical and nontechnical people, within the armed services and outside them. The topic has even attracted Congressional interest.[1] With all of this concern, it is essential that certain aspects of the reliability of such systems be brought more clearly into focus. This involves consideration of the differences between the two kinds of systems, as well as of the reliability requirements for both.

Both weapon systems and other (operable in peacetime) systems are defined in an initial section of Air Force Regulation 70–9.[2] The sole criterion used to distinguish between the two is that of intended use: a weapon system "forms an instrument of combat" (to quote the above regulation); a peacetime system—such as a nonweapon space system—does not. In other words the ultimate (*i.e.*, planned) use of a weapon system involves its being "fired in anger." It has been common usage (as is later found in the above regulation) to let the term "weapon system" be applied to both kinds of systems, and for many purposes this is acceptable. However, when considering the reliability requirements of systems involving ballistic missile boosters, it will be shown that weapon systems cannot always be lumped with other space systems.

A fundamental concept in considering reliability requirements is that these requirements are useful only insofar as they aid in planning the procurement and/or operation of the system to which they are applied. It follows, therefore, that they should be applied only to the extent to which they are useful; *i.e.*, there should be no leveling of *numerical* reliability requirements on a given system merely for the sake of doing so, or because other systems are so treated, or because of other similar reasons.

* Manuscript received by the PGMIL, July 21, 1959.

† Major, U. S. Air Force, Ballistic Missile Division, AF Unit P.O., Los Angeles, Calif.

[1] See, for example, "Department of Defense Appropriations for 1960, Pt. 1. Policy Statements," in "Hearing Before the Subcommittee of the Committee on Appropriations, House of Representatives, 86th Congress, First Session. Subcommittee on Department of Defense Appropriations," U. S. Govt. Printing Office, Washington, D. C., pp. 258-295; 1959.

[2] "Procurement and Contracting. Airborne Weapon System and Support System Procurement," Dept. of the Air Force, AF Regulation 70-9; 1956.

Ballistic Missile Weapon System Reliability

The desired output of any weapon system is the delivery, when desired, of a certain known amount of damage-creating energy upon a target. Regardless of the amount of the energy to be delivered (ranging from that of a small arms bullet to that of a megaton-yield warhead), the desired performance of the weapon system under given conditions of range or duration of operations, etc., may be tied to a single characteristic, the weapon accuracy. In other words, successful performance may be defined as designed energy delivery with an accuracy greater than some arbitrary limit (usually some simple function of the circular probable error). The probability that the weapon system will attain this performance under the given conditions of warning or preparation time, range or duration of operation, etc., is the numerical value of its reliability.[3]

For planning purposes, a known minimum numerical value of the system reliability must be assigned (with a known degree of confidence) to a weapon system involving ballistic missiles. This known reliability value is necessary for planners either to 1) estimate the most probable amount of damage that a given ballistic missile striking force, launched at a randomly occurring (uncontrolled) point in time, can inflict on an enemy, or 2) determine how large a ballistic missile striking force must be procured to be able to inflict a desired amount of damage, with a given degree of confidence, on an enemy under the same time consideration as in 1) above. Underlying this consideration is the concept that this country's national policy does not permit us the initiative in determining the exact time at which these weapon systems will be used in their ultimate operational environment, *i.e.*, "fired in anger." (With the present increasing emphasis on such ballistic missile weapons, maximum permissible national reaction times are reduced to fractions of an hour, strengthening the validity of this concept.)

[3] Note that for ballistic missiles the condition of warning or preparation time is at least as important as that of range or duration of operation. In fact, ballistic-missile weapon-system reliability is frequently broken down into at least three factors: probability of being ready to launch whenever desired, probability of achieving successful launch whenever desired, and probability of achieving successful flight. In any event, numerical values of both minimum accuracy and reliability are required for planning purposes.

Reliability of a Nonweapon Space System Using Ballistic Missile Boosters

At present, budgetary considerations influence the planning for such a system's size (*i.e.*, the number of ballistic missile boosters to be assigned to the system program) much more than for weapon systems. This is because of the fact that while peacetime-operable systems can conceivably be used for any of the system functions given in Air Force Regulation 70–9 (logistics, training, intelligence, etc.), the current state-of-the-art limits these programs to exploratory, semi-R and D efforts. The present cost and scarcity of ballistic missile boosters (including the necessary manpower, facilities, and supplies for their operation) puts a practical limit to the number of boosters available for such a program. As a result of this budgetary rather than operational limit, a space-system program of the kind being discussed in this paragraph, which will usually have many objectives (*i.e.*, desired outputs), will not have exactly the same objectives for any two attempted launches. In other words, there are no "space launches"; the failure (partial or complete) of any launch represents an irreparable failure to achieve a portion of the program's over-all objective. This implies a reliability requirement of 100 per cent which is unrealistic.[4]

Although future systems of this nature may not suffer from a budgetary, "no spares" limitation, the multiple-objective possibilities will always have to be considered.

Finally, the initiative for the use of such systems, since they operate during peacetime, at present generally rests with the planners. Therefore, no requirement imposed by the need to consider limited preparation or warning time, exists for system reliability. This is in direct contrast to the case for ballistic missile weapon systems.

Recommendations and Conclusions

It can be seen that space systems which are operable during peacetime and which use ballistic missile boosters, merit careful consideration as being distinct from ballistic missile weapon systems when their reliability aspects are involved. This does not mean that there will always be differences, but that sufficient basic differences may exist in individual system programs to require a different approach to expressing and achieving system reliabilities. Each nonweapon space system must be considered individually with regard to the following three criteria:

1) Does the system have only one all-important objective?

2) Can this objective be expressed in terms of a single system output characteristic corresponding to the accuracy of a weapon system?

3) Does the program for the system envisage sufficient material, when compared to the demands of the system's over-all objective, to permit redundancy, *i.e.*, "spare launches" (less than 100 per cent reliability requirement)?

Only if all three of these questions can be answered in the affirmative can the nonweapon space system be considered as if it were a weapon system so far as its reliability is concerned, *i.e.*, its reliability can be expressed as a simple probability.

For a system which does not meet the above criteria, the approach again is individualistic. Perhaps numerical expressions of reliability, if required, may be given in terms of maximum permissible losses of system outputs which characterize the system's objectives.[5,6] This implies that failure to attain these objectives to any extent whatsoever is permissible, but this may not be the case. If no such failure is permissible for planning purposes, then all that can be established as a system reliability requirement is the maximum possible reliability commensurate with available funds and the state of the art. Imposition of firmer demands (in the form of numerical values, however expressed) merely hampers development of the system by misdirected application of the limited funds and manpower available for this development.

Finally, the stupendous costs of the types of system discussed here make it extremely unlikely that tests of the entire system will ever be used as the sole means to demonstrate whether any predetermined system reliability requirements have been met at the end of the system development period. This means that any such demonstrations must involve tests of relatively inexpensive components of the system. This, in turn, implies the placing of a further requirement on the space system reliability approach: that it be of such a nature that any numerical system reliability requirements can be resolved into relatively easily demonstrable, component reliability requirements, preferably at the component part level.

A system reliability approach using the above concepts will place no heavier loads than those presently placed on design and reliability engineers working on component and component part levels; it *will* insure that these engineers' efforts will contribute more effectively to the desired system reliability.

[4] A secondary effect implied by this multiple-objective consideration is that the hardware will vary sufficiently from launch to launch so that success or failure in earlier launches of a program can no longer be used to predict the reliability (in terms of probability of success) of the later launches of the program. This is, of course, in direct opposition to the practice for ballistic missile weapon systems. This can be put into other terms by saying that the multiple-objective nature of such a peacetime-operable program makes the expression of its reliability as a numerical probability at least ambiguous, if not completely without meaning.

[5] A. C. Block, "Methods of relating performance to reliability," *Proc. Fifth Natl. Symp. on Reliability and Quality Control in Electronics*, Philadelphia, Pa., pp. 389-395; January 12-14, 1959.

[6] J. L. Burnside, "A Proposal for the Specification of Reliability in Military Equipment Contract," Lockheed Aircraft Corp., Missile and Space Div., Sunnyvale, Calif., Rept. No. LMSD-421249; February 15, 1959.

Radar Beacons for IRBM/ICBM*

F. J. CLARK†

Summary—**This paper summarizes problems which confront engineers who are responsible for the design of radar beacons and beacon antennas used in IRBM and ICBM test vehicles. The most important factors which affect compatibility between the beacon and tracking radars at the test range are enumerated. Cited also are several design areas which should be correlated with the test range prior to finalization of beacon design criteria.**

Introduction

DESIGN engineers concerned with radar beacons and beacon antennas for IRBM or ICBM test programs are confronted with many difficult interrelated problems. The general scope of those problems is probably not exceeded in any other area of electronic design activity.

In brief, the items to be considered by the engineer include simultaneously the requirements associated with uncompromising physical and operational environments. Specifically, he will be concerned with environmental extremes regarding temperature, pressure, vibration, and acceleration. His design criteria will be strongly influenced also by limitations on size, shape, weight, and power consumption. With respect to the test range environment, he will be fortunate if his initial activities or other commitments leave time to investigate thoroughly and to correlate the beacon design requirements with the capabilities of the tracking radars and their specific locations or planned utilization. The latter situation is one that will always require special attention because of the continual efforts of the test range to increase the performance capability of its radar facilities.

Compatibility Considerations Relating to Chain-Radar Operations

Successful radar beacon utilization in ballistic missiles is (usually) based on the necessity for simultaneous tracking by two or more widely separated radars (*i.e.*, chain-radar operation). This requirement, which presumes a satisfactory degree of compatibility between the beacon and the tracking radar, establishes basic criteria for the beacon design parameters listed below. Since the operational aspects for each missile test program differ, it is not feasible to suggest that either of these parameters is more important than another. Experience indicates, however, that deficiencies or incompatibilities in the following design areas cause most tracking failures in chain-radar operations:

1) Beacon antenna radiation pattern and/or polarization—this is also allied with changes in aspect angle and in-flight stability of the missile.

2) Poor frequency stability characteristics in transmitter and/or receiver.

3) Insufficient radiated power.

4) Inadequate receiver sensitivity.

5) Unfavorable AGC characteristics.

6) Too stringent a requirement relative to optimum spacing of (radar) interrogation code pulses.

7) Long recovery time.

8) Poor receiver selectivity.

Design Considerations for Beacon Antenna

The engineer should be aware of the type of antenna scan and polarization utilized by the tracking radars when formulating design criteria for the beacon antenna. For example, a simultaneous lobing, amplitude comparison, monopulse radar is especially sensitive to interferometer-type nulls in the radiation pattern when two or more beacon antennas are driven simultaneously. As a typical case, four such antennas spaced 90° around a specific missile produced several 30-db nulls approximately 4.5° apart. As the radar looked at this portion of the pattern, discontinuities in the angle tracking data occurred each time missile roll corrections caused the radar to scan through a null.

Another important consideration involves a practice at the test ranges of employing separate "skin" and "beacon" receivers to provide simultaneous radar display of skin and beacon signals. This is a range safety measure which permits transfer of the tracking function to the skin return in case of beacon failure at or soon after missile launch. This procedure, with current radars, sacrifices 3 db in the beacon reply due to signal "splitting" in the radar mixer. It also poses a question to test range personnel concerning the optimum radar antenna polarization for simultaneous skin and beacon tracking. Present opinion at AFMTC favors linear polarization for the radar and circular polarization for the beacon. After further investigation it may be determined that this idea should be reversed, *i.e.*, circular polarization may be preferred on the radar and linear polarization on the beacon. Either arrangement, however, will introduce another 3-db loss (each way) in the radar-beacon transmission loop.

Beacon Magnetron Frequency Stability Problem

One magnetron design parameter which appears to have received only passive interest involves frequency change vs pulse repetition rate. When a second and perhaps third radar in a chain network phases in with beacon interrogations, minimum shift in beacon magnetron frequency is desired. Otherwise, the receiver AFC may fail to maintain proper tuning of the radar with the beacon transmitter. Since tracking failures cannot easily be post-related to this

* Manuscript received by the PGMIL, July 21, 1959.

† Data Instrumentation Div., Directorate of Range Dev., Patrick AFB, Fla.

deficiency, it deserves careful consideration in missile-beacon applications.

The AGC Problems

Simultaneous interrogations by more than one radar infers that the beacon must alternately respond to strong and weak signals. At times, the level of one signal may be near zero dbm and the other(s) anywhere from −30 dbm to −65 dbm. This requires special attention in receiver design, but anything less than instantaneous AGC in the beacon is undesirable for chain-radar operations.

Considerations Relating to the Spacing of Interrogation Code Pulses

For multiple pulse interrogation codes, close spacing and tight tolerance on the position of pulses impose a problem in calibrating the radar pulse encoder at distant range stations. Multiple pulse codes are used principally to reduce interference from undesired radars. Close pulse spacing with narrow position deviation limits provides additional safety against such interference. However, for a radar to transmit reliably and consistently such multiple pulse codes, rigorous and precise calibration of the radar encoder is necessary. Previous chain-radar experience leads to a question in this case concerning the validity of the earlier philosophy of "close spaces—tight tolerances." Factors bearing on this problem which encourage some relaxation in requirements are:

1) The reliability of precision calibration equipment, after exposure to a humid climate and shipment to a remote range site, is actually indeterminate.
2) A reliable estimate on the long-term uniformity of calibration equipment at each of several widely separated sites cannot be established.

Recovery Time Considerations

Recovery time relates to the ability of a beacon to reply to each interrogation received. Relatively high interrogation rates, such as encountered with chain-radar operations, require a reasonably short recovery time. Currently, with three "long-range" radars in the chain, a maximum recovery time of 300 μsec is permissible. Future radar improvements to provide automatic sequencing, or interlacing of interrogations from several radars, will reduce maximum permissible beacon recovery time to approximately 50 μsec.

Minimum recovery time is a problem to the extent that ring-around, or self-triggering from the beacon's own transmissions should not occur. If recovery time is less than approximately 12 μsec, however, the beacon reply signals reflected from nearby structures (in the launch area) are likely to cause self-triggering.

Beacon Transmitter Power and Receiver Sensitivity Considerations

The rated power output of the beacon, of course, has a bearing on the predicted beacon signal level that will be available at the radar receiver. To have any real significance, however, the beacon output power should be appropriately related to the deepest null through which any particular test range radar is expected to track. With this qualification, the beacon transmitter power is of most interest as one of the factors in the communications loop between the radar and the beacon. Three other items of interest in that loop are beacon receiver sensitivity, radar transmitter power, and radar receiver sensitivity. Systems-wise, the objective always is to have the quantitative values for those items so related that the ability to communicate from the radar to the beacon will be identical to that which will be provided between the beacon and the radar. When that condition is achieved, the two-way path between the radar and beacon is referred to as a balanced-loop. Due to various technological considerations, responsibility for meeting the balanced-loop criteria is normally placed on the beacon designer. He must therefore have up-to-date information on the characteristics of test range radars before he can establish optimum design limits for the beacon receiver or transmitter. Furthermore, he needs such information in order to make intelligent compromises in the beacon design which, for many special purposes, may be necessary.

Receiver Selectivity Considerations

Beacons with crystal-video-type receivers inherently have insufficient sensitivity and poor frequency selectivity characteristics. Because of their low sensitivity, they are generally considered unsatisfactory for chain-radar operations. They are also considered unsatisfactory in this application because of their susceptibility to interference from radars operating in each of the primary radar frequency bands. Experience reveals that such a nonselective beacon will frequently be triggered by an adjacent channel CW signal, or by a radar operating at a frequency separated from the nominal frequency of the beacon receiver by more than 2500 mc.

Even with super-het receivers, the designer should keep in mind that poor selectivity will create a troublesome problem. The high concentration of electronic radiating devices at a test range, operating at many different frequencies with all types of modulation and power levels from fractions of watts up to several megawatts, presents a more severe electronic environment than is normally experienced in any other beacon application.

Other General Compatibility Considerations

Data Accuracy vs Radar S/N Ratio

In most missile radar beacon applications, the ability to estimate quickly the quality of the radar data is desirable. The simplified equations presented below provide a convenient method for doing this, assuming that the beacon transmitted power and radiation pattern are known. These equations have been verified under controlled tests using a specific monopulse radar. However, similar equations may be derived for other precision tracking radars:

RMS angle noise error (mils):

$$\sigma_\theta = \frac{\theta}{\sqrt{2\,\frac{f_r}{B_n}\cdot S/N}}, \qquad (1)$$

where

θ is antenna beamwidth (mils)
S/N is IF signal-to-noise power ratio in the sum channel (for $S/N > 6$ db)
f_r is radar repetition rate, and
B_n is equivalent noise bandwidth of angle servos.

RMS range error (yards):

$$\sigma_R = \frac{\tau}{\sqrt{\frac{f_r}{B_n}\cdot\frac{S}{N}}} \qquad (2)$$

where

τ is pulse width (in yards)
B_n is bandwidth of radar range servo, and S/N and f_r are the same as in (a) above.

These equations are of interest at AFMTC since they provide convenient, slightly conservative estimates of radar performance capabilities over any specific portion of a missile's trajectory. The signal-to-noise ratio is the most significant factor, since it is the only variable which is not under direct control of the radar operator. Note that for tracking high-velocity close-in targets, the wider servo bandwidths that must be used require higher signal-to-noise ratios—nominally, 19-23 db—to maintain a specified level of system accuracy.

Since the use of these equations presupposes a one-to-one beacon reply for each radar interrogation, a word of caution regarding them is added. If the beacon receiver sensitivity or beacon antenna pattern characteristics are deficient, the beacon will "countdown" (not reply to every radar interrogation). Beacon countdown directly affects the quality of radar data, but as a rule of thumb, countdown of up to ten per cent may be permissible when tracking missiles out beyond 150 miles. In order for the radar to maintain automatic track, the maximum allowable beacon countdown is established by the commutation (sampling) rate of the error signal from the radar tracking servos. This commutation rate in a monopulse radar is usually ⅓ to ⅙ of the radar PRF. To maintain automatic track (even though the data will be very poor) the radar should receive one beacon reply for each half-cycle of the error commutation signal.

Beacon Reply-Delay Considerations

A choice of beacon reply-delay settings is desirable when performing prelaunch pad checks with the radar. This feature will permit the separation of beacon replies from the radar signals which are reflected from missile test stands or other structures in the vicinity of the launch pad. The provision of at least two fixed-delay settings is desirable. Furthermore, simultaneous tracking of more than one beacon in the same missile will be possible if a different delay setting for each beacon is available.

The range data accuracy from a precision radar is directly related to variations in reply-delay time of the beacon. The capability of current radars suggests that delay variations should not exceed 0.006 μsec. This is a severe requirement when it is related to the necessity for chain-radar tracking and the wide differences in radar signal levels encountered by the beacon. In this circumstance, reference is again made to the fact that the usual type receiver AGC is undesirable.

Target Acquisition Techniques

Two techniques used at downrange stations to acquire the target at maximum range involve switching to narrow-band radar receiver operation and the use of wider transmitter pulses. The narrow bandwidth provides an improvement in radar receiver signal-to-noise ratio of approximately 4 db, and the wider pulses increase the range at which the beacon may be triggered, *i.e.*, with same radar PRF.

Conclusions

This discussion has presented a brief review of several important and somewhat arbitrarily chosen problem areas concerning the design and utilization of radar beacons for IRBM and ICBM tests. It has been possible to use quantitative data in only a few instances; first, because missile test program objectives differ; second, because of the uncertainties relating to the final outcome of current radar improvement programs.

Portions of this discussion, however, are presented as a critique of current methods and techniques used in the formulation of beacon design criteria. This approach seems justified because of a continuation in basic design deficiencies for a large number of the more recent beacon developmental projects. The primary difficulty seems to be based on failure of beacon designers to properly observe the "systems concept" in establishing beacon design requirements. The designer is thus reminded that, first, and through whatever channel may be appropriate, he should expend all effort necessary to learn the characteristics of test range radars and the operational techniques utilized.

Acknowledgment

The author gratefully acknowledges that a large portion of the material discussed herein is based on unpublished data and informal discussions during the past year with A. E. Hoffman-Heyden, RCA Service Co., Patrick AFB, Fla. Acknowledgment is also made of numerous beneficial discussions on radar beacon problem areas with F. H. Dyke, RCA Service Co., L. F. O'Kelly, Radiation, Inc. (formerly RCA Service Co.), and H. C. Wilson, AFMTC.

Design Studies for a Rubidium Gas Cell Frequency Standard*

J. M. ANDRES†, D. J. FARMER†, AND G. T. INOUYE†

Summary—**A description is given of several studies undertaken in the design of a small, gas cell stabilized atomic frequency standard making use of the field-independent hyperfine resonance of rubidium 87 at 6834 mc. In the standard considered, light from a rubidium vapor lamp is used to enhance the population differences between the atomic levels involved in the resonance and also to provide a means of detecting the microwave resonance. One of the studies described is concerned with the generation of requisite microwave energy at the resonant frequency, another with the choice of an optimum length for the gas cell, and the last with the optimization of parameters for the modulation process used.**

I. Introduction

WE present here the results of several studies undertaken in the design of an atomic frequency standard. The standard is of the gas cell absorption type and is intended for possible use in missiles or space vehicles—applications which subject the device to stringent limitations on weight and power consumption, and which demand high performance for operation under vibration environments varying from moderate to severe. Of the many problems these and other requirements present to the designer, we shall consider here only three—one deals with generation of the requisite microwave energy, another leads to an optimum choice for the length of the absorption cell, and the last is concerned with optimization of parameters for the modulation process employed. All three of these problems can be discussed within the framework of the functional diagram for the standard shown in Fig. 1 and the brief description of its operation given below.[1]

Optical resonance radiation from a rubidium lamp is transmitted through a glass cell containing a vapor of the isotope rubidium 87 and a small amount of argon or other buffer gas, the purpose of the latter being to reduce Doppler broadening in the microwave resonance of interest [6]. The action of the optical resonance radiation produces a difference in population between the hyperfine levels of the ground state of Rb^{87} far in excess of that which obtains under thermal equilibrium. This is the process of optical pumping [7], [8]. The energy separation of the hyperfine levels is approximately 6834 mc; when the atoms in the cell are subjected to a radiation field of that frequency, transitions between the hyperfine levels are induced which tend to reduce the population difference built up by optical pumping and, in so doing, to change the amount of optical resonance radiation transmitted through the gas cell to the optical detector.

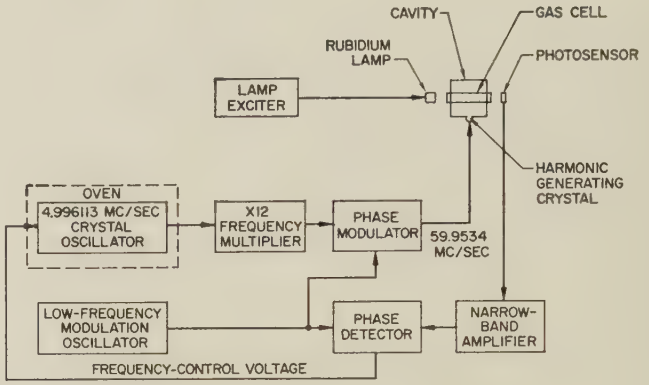

Fig. 1—Functional diagram of frequency standard making use of the optical detection of the field-independent hyperfine resonance of rubidium 87 occurring at 6834 mc. Arrangements for producing the static magnetic field required and other control equipment are not shown.

Modulating the phase or frequency of the microwave field a small amount at some low rate modulates the intensity of the light reaching the detector at the same rate. The amplitude of the modulated light intensity is in some sense proportional to the slope of the microwave resonance absorption line. By synchronously demodulating the amplified output of the photosensor a dc error voltage is obtained which is used to control the frequency of a piezoelectric quartz crystal oscillator. The oscillator operates at a subharmonic of the hyperfine resonance frequency and, through the multiplier chain, provides the microwave energy used in irradiating the gas cell. If the control loop so formed is not closed and the microwave frequency is varied through resonance the error voltage developed at the output of the phase detector is as shown in Fig. 2.

II. Microwave Generation

Microwave power absorbed by the rubidium atoms in the gas cell is negligibly small; however, to induce transitions an RF magnetic field having an amplitude of about 3×10^{-5} gauss must be maintained. A field of that magnitude may be obtained with a power dissipation of 10^{-8} watts in a cavity having a loaded Q of about 2000—the latter being a value realizable for a cavity enclosing the gas cell. This rather low power requirement for the 6834-mc signal suggests that it be derived as a harmonic from a crystal diode. Because of weight and power considerations it is desirable that the subharmonic signal driving the diode be generated in a transistor stage; thus the question of interest is the order of multiplication that should be required of the diode. The answer hinges on the state of the art of the components.

One of the most recent advances has been the availability on the commercial market of the diffused-base silicon

* Manuscript received by the PGMIL, July 21, 1959.
† Space Technology Labs., Inc., Los Angeles 45, Calif.
[1] More detailed information concerning the principles governing the operation of devices of this type is found in [1]-[5].

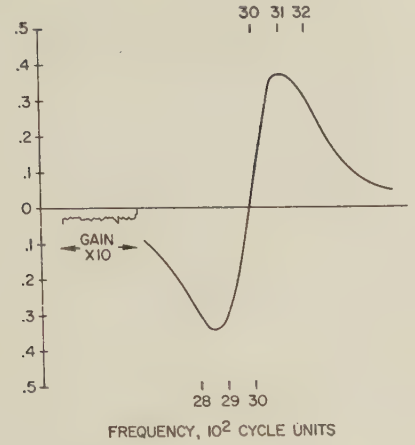

Fig. 2—The error voltage at the output of the phase detector as the microwave frequency is slowly passed through the atomic resonance. This curve was obtained in the laboratory with apparatus similar to that shown in Fig. 1. An indication of the noise present is found by increasing the narrow-band amplifier gain when the microwave frequency is off resonance.

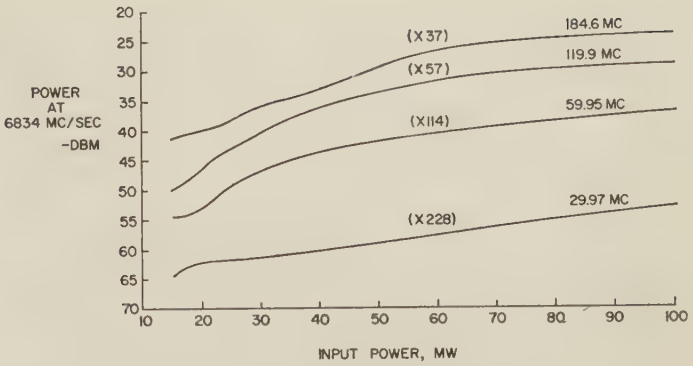

Fig. 3—The frequency multiplication characteristics of a commercially available silicon diode (Microwave Associates 460E).

p-n junction diodes. The properties of one such device used as a frequency multiplier are shown in Fig. 3. We note that 40 milliwatts input at the 114th subharmonic, about 60 mc, produces the required power. By comparison, if a diode of the usual type, such as a 1N23B, were to be used, measurements show that 500 milliwatts input would be required at the 50th subharmonic, or 40 milliwatts at the 17th subharmonic.

Transistors presently available could be used in conjunction with the usual crystal diode; however, use of the p-n junction diodes requires fewer transistor multiplier stages, and the lower frequencies involved result in a greater electrical efficiency. We can expect that improvements in both transistors and diodes may soon admit even further reduction in the number of components required in the microwave generator portion of the standard.[2]

III. Optimum Cell Length

One example of system optimization concerns the choice of an optimum gas cell length. The optimum length is defined to be the length giving the maximum change in transmitted light intensity as the microwave frequency passes through the atomic hyperfine resonance frequency. The light absorbing character of the cell depends upon several factors: the length of the cell, the number of absorbing atoms present in the cell in a unit length, the distribution of these atoms among the several absorbing substates, the spectral character and polarization of the light incident upon the cell, and the atomic thermal relaxation effects in the cell. The distribution of atoms in the substates and, hence, the light absorbed by the cell is changed as the microwave frequency passes through resonance. The magnitude of change depends upon the cell length and the other factors. Thus, in order to determine an optimum cell length, it is necessary to determine the dependence of the light absorption by the cell upon these various factors. Let us first make some simplifying assumptions.

We shall assume that the incident optical radiation is unpolarized and is of two frequency components which have the intensity g_1 and g_2 and which are capable of being absorbed by the $F = 1$ and $F = 2$ sublevels of the $5S_{1/2}$ ground state of Rb^{87}, respectively.[3] When light is absorbed and the atoms are subsequently excited to the $5P_{3/2}$ or $5P_{1/2}$ states, we assume that the states are completely mixed by collisions with the buffer gas atoms before reradiation so that the probability of atoms returning to any one of the eight sublevels is equal to one eighth of the total original absorption probability. In addition, we assume that the eight sublevels are mixed by means of thermal relaxation processes characterized by a relaxation time T, that reradiated light cannot be further absorbed, and that the atoms at a given position in the cell remain relatively fixed in position during the absorption and reradiation process. With these assumptions it is possible to compute the light absorbed as a function of gas cell length and other factors and to determine the cell length giving the maximum change in transmitted light when the microwave frequency passes through the atomic resonance.

For light of frequency ν incident upon an atom, the probability of absorption per unit time per atom is

$$P = \pi r_0 c g(\nu) f \qquad (1)$$

where $r_0 = 2.818 \times 10^{-13}$ cm, the electron radius, $c = 3 \times 10^{10}$ cm/sec, the velocity of light, $g(\nu)$, is the spectral intensity, the number of photons/cm² sec in a 1-cps band, and f is a dimensionless number called the oscillator strength of the transition.

The number of atoms per cm³ in the three substates of $F = 1$ capable of absorbing light is $N(a_1 + a_2 + a_3)$, where N is the total number of rubidium atoms per cm³ and a_1, a_2, and a_3 represent the fraction of the total number in each of these substates. The atoms are not "tuned" to

[2] It may be argued that further simplification of the design of Fig. 1 can be achieved even now by using a crystal oscillator of higher frequency. The choice of 5 mc is based on the apparent superiority of available crystal units in that frequency neighborhood.

[3] For information about spectroscopic notation and atomic energy levels see [9]. [5] contains a figure showing the energy levels in sodium, which is similar to rubidium.

absorb a single frequency, but because of Doppler effect, are distributed to absorb over a band of frequencies of width $\Delta\nu_D$. If they are assumed to be uniformly distributed over this band, the number capable of absorbing light in a 1-cps band at a frequency ν within the band is

$$\frac{N(a_1 + a_2 + a_3)}{\Delta\nu_D}.$$

If the intensity g_1 illuminating the $F = 1$ substates is assumed uniform over the band $\Delta\nu_D$, we have, for the change in g_1 over this band per length dx,

$$\frac{dg_1}{dx} = \frac{-\pi r_0 c f g_1 N(a_1 + a_2 + a_3)}{\Delta\nu_D}. \tag{2}$$

Similarly, assuming the intensity g_2 illuminating the five $F = 2$ substates is uniform over a band $\Delta\nu_D$, we have, for the change g_2 over the band $\Delta\nu_D$,

$$\frac{dg_2}{dx} = \frac{-\pi r_0 c f g_2 N(a_4 + a_5 + a_6 + a_7 + a_8)}{\Delta\nu_D}. \tag{3}$$

The a_i are functions of x through g_1, g_2 and also of the relaxation time T. Let us consider what a_i's are for two cases of interest.

Case 1—Microwave Frequency Off Resonance

Under these circumstances $a_1 = a_2 = a_3$ and $a_4 = a_5 = a_6 = a_7 = a_8$. By balancing the relative number of atoms leaving a state with the number re-entering the state, a_1 and a_4 can be determined. Thus, the processes of absorption, reradiation, and relaxation must yield no net flow of atoms from a given state under equilibrium conditions. A determination of a_1 and a_4 gives:

$$a_1 = \frac{I_2 + \alpha}{5I_1 + 3I_2 + 8\alpha} \tag{4}$$

$$a_4 = \frac{I_1 + \alpha}{5I_1 + 3I_2 + 8\alpha} \tag{5}$$

where

$$\alpha = \frac{1}{\pi r_0 f c T g_0},\quad I_1 = \frac{g_1}{g_0},\quad \text{and } I_2 = \frac{g_2}{g_0}.$$

(α, I_1, I_2 are dimensionless.)

Putting (4) and (5) into (2) and (3) we obtain

$$\frac{dI_1}{dy} = -\frac{3I_1(I_2 + \alpha)}{5I_1 + 3I_2 + 8\alpha} \tag{6}$$

$$\frac{dI_2}{dy} = -\frac{5I_2(I_1 + \alpha)}{5I_1 + 3I_2 + 8\alpha} \tag{7}$$

where

$$y = \frac{\pi r_0 c N f x}{\Delta\nu_D},$$

is a dimensionless quantity.

For infinite relaxation time $\alpha \to 0$ and (6) and (7) reduce to equations of the form obtained in [5].

Case 2—Microwave Frequency On Resonance

We assume the microwave power saturates the transition between substates 2 and 6. Thus $a_2 = a_6$. In addition $a_1 = a_3$ and $a_4 = a_5 = a_7 = a_8$. Under equilibrium conditions we obtain:

$$a_2 = a_6 = \frac{4(I_2 + \alpha)(I_1 + \alpha)}{\Delta} \tag{8}$$

$$a_1 = a_3 = 2\,\frac{(I_1 + I_2 + 2\alpha)(I_2 + \alpha)}{\Delta} \tag{9}$$

$$a_4 = a_5 = a_7 = a_8 = \frac{2[I_1^2 + I_1 I_2 + \alpha(I_2 + 3I_1) + 2\alpha^2]}{\Delta} \tag{10}$$

where

$$\Delta = 4[2I_1^2 + 5I_1 I_2 + I_2^2 + \alpha(7I_2 + 9I_1) + 8\alpha^2].$$

Putting these quantities into (2) and (3) we obtain

$$\frac{dI_1}{dy} = \frac{-I_1[2I_1 I_2 + I_2^2 + (4I_2 + 2I_1)\alpha + 3\alpha^2]}{[2I_1^2 + 5I_1 I_2 + I_2^2 + \alpha(7I_2 + 9I_1) + 8\alpha^2]} \tag{11}$$

$$\frac{dI_2}{dy} = \frac{-I_2[2I_1^2 + 3I_1 I_2 + (3I_2 + 7I_1)\alpha + 5\alpha^2]}{[2I_1^2 + 5I_1 I_2 + I_2^2 + \alpha(7I_2 + 9I_1) + 8\alpha^2]} \tag{12}$$

where y, α, I_1, and I_2 are the dimensionless quantities previously defined.

The magnitude of the signal is defined by the change in total light intensity $I_1 + I_2$ as the microwave frequency is changed from off resonance to on resonance, *i.e.*, the difference in the two cases just treated. The quantity $S = (I_1 + I_2)_{\text{off res}} - (I_1 + I_2)_{\text{res}}$ is plotted in Figs. 4-6 for three values of I_{10} and I_{20}, the magnitude of I_1 and I_2 at $y = 0$, and for a number of values of α.

The case of $I_{10} = 1.0$ and $I_{20} = 0.25$ corresponds to illuminating the $F = 1$ levels more intensely than the $F = 2$ levels. This is achievable, in practice, by filtering the light from a Rb^{87} lamp by passing it through a cell containing Rb^{85} [10]. The case $I_{10} = I_{20} = 1.00$ corresponds roughly to illuminating with a lamp containing naturally occurring rubidium. The case $I_{10} = 0.25$, $I_{20} = 1.0$, corresponds to illuminating with light from a Rb^{85} lamp. Some reasonable values for the quantities of interest are:

$$g_0 = 10^5 \text{ photons/cm}^2 \text{ sec sec}^{-1},$$
$$T = 10^{-2} \text{ sec},$$
$$f \simeq 1,$$
$$\Delta\nu_D = 5 \times 10^8 \text{ cps},$$
$$N = 10^{10} \text{ atoms/cm}^3; \text{ (temperature} \sim 40°\text{C)}.$$

These values give $\alpha = 0.04$ and

$$y = \frac{x(\text{cm})}{1.88} \qquad (y = 4 \text{ for } x = 3 \text{ inches}).$$

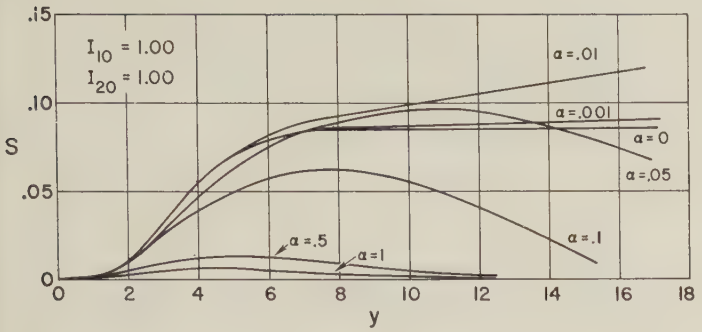

Fig. 4—The signal quantity, S, is a function of the dimensionless length y, for several values of the parameter α. Dimensionless intensities at $y = 0$ are $I_{10} = 1.0$, $I_{20} = 1.0$.

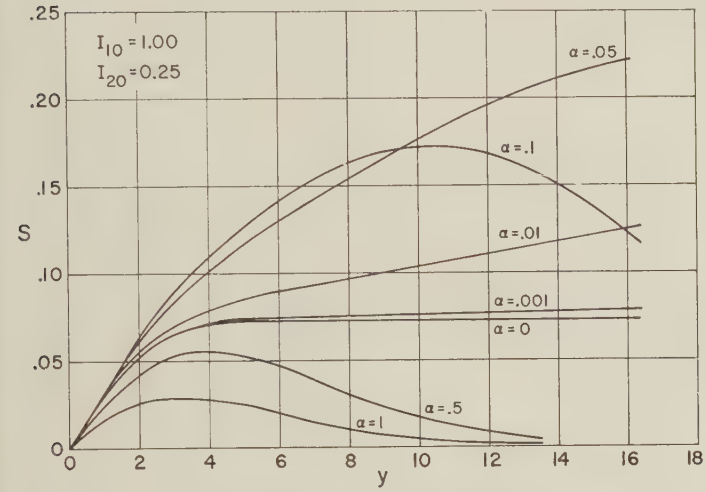

Fig. 5—The signal quantity, S, as a function of the dimensionless length y, for several values of the parameter α. Dimensionless intensities at $y = 0$ are $I_{10} = 1.00$, $I_{20} = 0.25$.

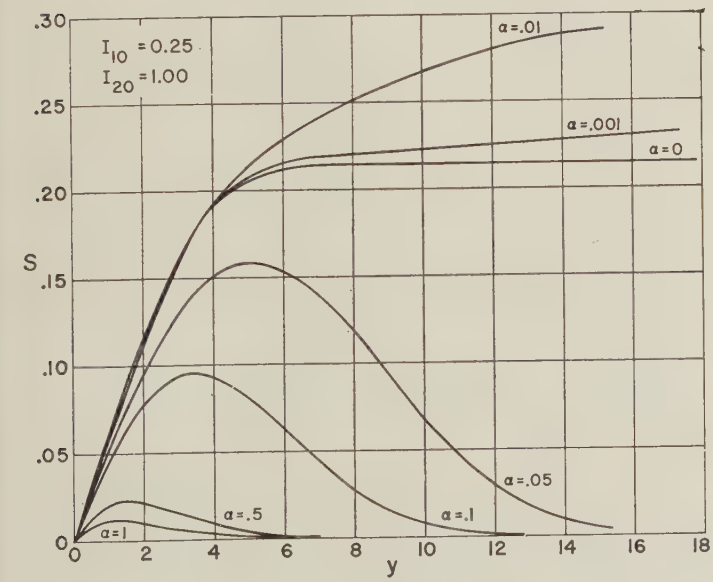

Fig. 6—The signal quantity, S, as a function of the dimensionless length y, for several values of the partmeter α. Dimensionless intensities at $y = 0$ are $I_{10} = 0.25$, $I_{20} = 1.00$.

Looking at the curves for $\alpha = 0.05$, it is seen that a maximum occurs somewhere between $y = 6$ and $y = 20$, depending on the nature of the illumination. We have chosen to make the cell length approximately six inches, using a cavity mode TE_{014}. As the temperature is increased, thus increasing N and y, the signal obtained in the laboratory exhibits a maximum at a temperature of about 37°C. Thus, the fact that such a maximum exists is readily demonstrable. Since the intensities $\mathcal{I}_1$ and $\mathcal{I}_2$ emitted by the lamp are not known with any precision, it is difficult to determine a definite identification between these theoretical curves and the laboratory results. The curves indicate that operation with a Rb^{85} lamp should give a larger signal for a cell which is shorter than required with the other lamps—a fact in agreement with some tentative laboratory results.

IV. Optimization of Modulation Parameters

It is convenient to consider the role played by the atomic system as that of a frequency discriminator of very high stability. Departures of the controlled crystal oscillator from the center frequency of this discriminator are sensed, and the error voltage is used to correct the frequency of the oscillator. The process is thus analogous to the operation of usual automatic frequency control systems, and a similar analysis of the control loop may be applied. An important parameter of such a loop is, of course, the slope of the discriminator characteristic at center frequency. Other things being the same, it is desirable to obtain as great a value for the slope as circumstances will allow. The previous section dealt with one means of increasing the resonance signal and, hence, the discriminator slope. The present discussion considers the effect of the modulation parameters on the discriminator slope and the method by which a careful choice of these parameters can increase the slope.

As a starting point we use the result of Karplus [11] for the signal produced when an atomic resonance is observed with a frequency-modulated microwave excitation. The general result relates the modulation rate Ω, the frequency excursion amplitude of the modulated wave $\dot{\omega}$, the functional form of the frequency modulation $h(\Omega t)$, and the deviation of the unmodulated microwave frequency from the line center $\tilde{\omega}$, to a function F containing the time dependence of the microwave absorption coefficient.

$$F = \mathrm{Im}\left\{ i \int_0^\infty d\tau \exp\left[- i \int_{t-\tau}^{t} dt' \omega' h(\Omega t') - (i\tilde{\omega} + b)\tau \right] \right\} . \quad (13)$$

The quantity b is the reciprocal of the relaxation time T; it will depend on processes occurring within the gas cell but not on the modulating parameters and is assumed as given.

Provided the probability per second for optical photon absorption in the pumping process is greater than Ω, *i.e.*, $l - 1 < I_{1/\alpha}$, intensity modulation of the optical resonance radiation transmitted through the gas cell to the detector will be proportional to F. For these results to be applicable, the microwave field must be sufficiently weak so that no "saturation" effects occur.

If the microwave radiation is phase modulated at a rate Ω with a deviation of amplitude ϕ such that its instantaneous phase is $\omega t + \phi \sin \Omega t$, then we may write $\dot{\omega} = \phi\Omega$, and for the frequency modulation function, $h(\Omega t) = \cos \Omega t$. With this form for h, (13) may be integrated to yield for the component of F oscillating at frequency Ω,

$$F_\Omega = \frac{1}{b}\left[A \cos \Omega t - B \sin \Omega t\right] \tag{14}$$

with

$$A = \sum_{s=-\infty}^{\infty} \frac{J_s(\phi)\left[J_{s+1}(\phi) + J_{s-1}(\phi)\right]}{(sl + c)^2 + 1} \tag{15a}$$

$$B = \sum_{s=-\infty}^{\infty} \frac{J_s(\phi)\left[J_{s+1}(\phi) - J_{s-1}(\phi)\right]}{(sl + c)^2 + 1} \cdot (sl + c), \tag{15b}$$

where $J_s(\phi)$ is the Bessel function of the first kind of order s,

$$c \equiv \frac{\bar{\omega}}{b}, \quad g \equiv \frac{\omega'}{b}, \quad l \equiv \frac{\Omega}{b},$$

and

$$\phi = \frac{g}{l}.$$

While components of F at frequencies $n\Omega$ $(n = 2, 3, \ldots)$ are also present, only the fundamental is usually of interest since in practical systems the signal from the photosensor is processed in a narrow-band amplifier tuned to that frequency.

Note that F_Ω has two components, one of amplitude A oscillating in phase with the frequency modulation function h (but out of phase with the phase modulation), and a second of amplitude B, out of phase with h. It may be shown that $B \to 0$ as either $b \to 0$ or $\Omega \to 0$ whereas A is nonzero for $b = 0$ or $\Omega \to 0$. Thus, the presence of the out-of-phase component arises from relaxation processes, as we might expect. Both A and B vanish as $\dot{\omega} \to 0$ or as $\bar{\omega} \to 0$.

We may view the operation of the phase detector as producing the time average of the product of its inputs. One input is F_Ω and the other is the phase modulation function; to account for phase delays in the narrow-band amplifier or for delays that may be intentionally introduced the reference input is represented as proportional to $\sin(\Omega t + \Phi)$. The phase detector output is thus proportional to

$$A \sin \Phi - B \cos \Phi \tag{16}$$

which describes the general shape of the discriminator characteristic for the system. The curve shown in Fig. 2 is an example of the function described by (16).

In seeking the maximum slope at the center frequency of the characteristic, *i.e.*, at c or $\bar{\omega} = 0$, let us ignore for the moment the latitude allowed by choice of Φ and examine

$$\left(\frac{\partial A}{\partial c}\right)_{c=0} \quad \text{and} \quad \left(\frac{\partial B}{\partial c}\right)_{c=0}.$$

Those two quantities have been calculated for various values of l and g and are displayed in Figs. 7 and 8. The values of the modulation parameters yielding maximum slope in either case may be calculated; we find

$$\max\left(\frac{\partial A}{\partial c}\right)_{c=0} = -0.770, \text{ at } l = 0, \; g = 0.707,$$

and

$$\max\left(\frac{\partial B}{\partial c}\right)_{c=0} = 0.750, \text{ at } l = 1.732, \; g = 1.836.$$

Examining Figs. 7 and 8, it is noted that for values of l and g which result in large slope for one component, the slope of the other components is rather small; we conclude that $\Phi \simeq \pi/2$ or $\Phi \simeq 0$ (the former giving A as the discriminator characteristic and the latter, B) will yield conditions of maximum slope provided the appropriate values of l and g are chosen. On the basis of optimum slope alone, use of the A characteristic is clearly indicated; however, other factors may have to be considered. For several reasons, chiefly to reduce 1/f type noise generated in the optical pumping lamp or the photosensor and subsequent amplifier, it is desirable to use as large a modulation rate as practicable. Attaining its maximum slope at a modulation rate different from zero, the B component accommodates this condition very conveniently.

Curves similar to those shown in Figs. 7 and 8 have also been calculated for frequency modulation whose form is a square wave. The results are similar, except that the maximum slope of the A characteristic is somewhat greater at zero modulation rate, and the slope for a given value of g, in general, falls off more rapidly with increasing modulation frequency. For the B component, the maximum slope is about 0.5. We have not undertaken to solve for the optimum form of the modulation function, nor do we expect that the effort would be very rewarding since there is not a very great difference in results between the two rather extreme cases already discussed; furthermore, the complication in producing a modulating function different from sinusoidal would probably weigh against its use in any practical design.

The remarks which have been made regarding the desirability of using the B characteristic are based on the original assumption that other things are the same. The other things, of course, are the noise contributions of various portions of the system. Noise which may be viewed as amplitude modulation, such as produced by fluctuations in the lamp intensity or the usual noise from the detector and following circuits, will effect the output of the phase de-

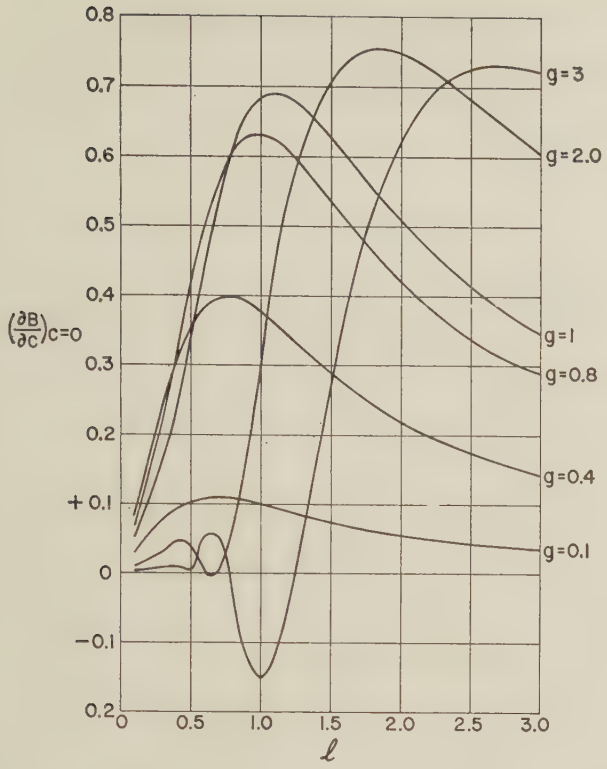

Fig. 7—The slope at resonance of the component of the optical intensity modulation out of phase with the frequency modulation function.

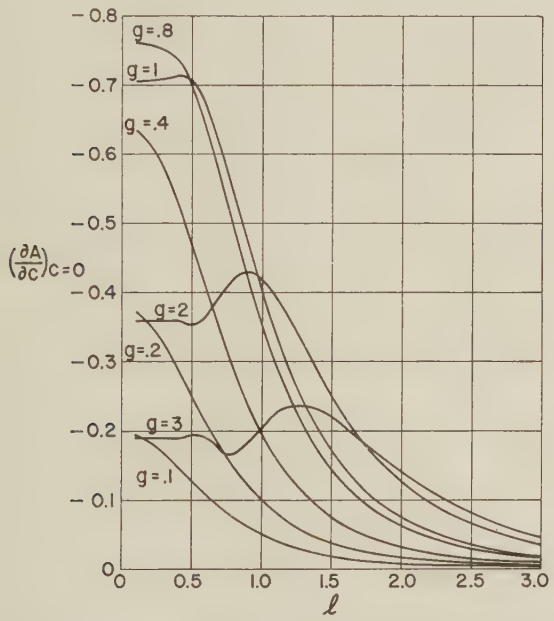

Fig. 8—The slope at resonance of the component of the optical intensity modulation in phase with the frequency modulation function.

tector similarly whether the A or B component is used. Another type of noise, spurious phase modulation components on the microwave signal, such as may be produced either in the crystal oscillator itself or in the subsequent circuits, may affect the separate components differently. When the total phase deviation at the microwave frequency is less than a radian, it proves possible to obtain an analytic representation for the noise spectrum at the output of the phase detector; however, the results in the form that we presently have them do not admit of ready comparison for the two separate cases. Within the present state of the art, noise produced in the optical pumping lamp and the photosensor seem to be the dominant sources of frequency instability. Presumably these contributions can be decreased as technology progresses, and the phase type noise may then become more important.

V. Acknowledgment

It is a pleasure to acknowledge several illuminating discussions with Dr. R. C. Ward regarding the modulation parameter optimization, and the assistance of H. Tuens and Miss R. Gittelman of our Computation Center who programmed the equations of Sections III and IV for the IBM 704 computer.

VI. References

[1] J. P. Wittke, "Molecular amplification and generation of microwaves," Proc. IRE, vol. 45, pp. 291–316; March, 1957.
[2] R. H. Dicke, T. R. Carver, and C. O. Alley, "Investigations of the Effect of Gas Collisions and Optical Pumping on the Breadth of Spectral Lines," first through twelfth quarterly reports by Palmer Physical Lab., Princeton University, Princeton, N.J., to U.S. Army Signal Eng. Lab., Fort Monmouth, N.J., on Contract DA-36-039 SC-70147; 1955–1958.
[3] W. E. Bell and A. Bloom, "Optical detection of magnetic resonance in alkali metal vapor," *Phys. Rev.*, vol. 107, pp. 1559–1565; September 15, 1957.
[4] W. E. Bell and A. Bloom, "Optically detected field-independent transition in sodium vapor," *Phys. Rev.*, vol. 109, pp. 219–220; January 1, 1958.
[5] W. E. Bell, A. Bloom, and R. Williams, "A microwave frequency standard employing optically pumped sodium vapor," IRE Trans. on Microwave Theory and Techniques, vol. MTT-7, pp. 95–98; January, 1959.
[6] R. H. Dicke, "The effect of collisions upon the Doppler width of spectral lines," *Phys. Rev.*, vol. 89, pp. 472–473; January 15, 1953.
[7] A. Kastler, "Optical methods of atomic orientation and of magnetic resonance," *J. Opt. Soc. Amer.*, vol. 47, pp. 460–465; June, 1957.
[8] H. G. Dehmelt, "Slow spin relaxation of optically polarized sodium atoms," *Phys. Rev.*, vol. 105, pp. 1487–1549; March 1, 1957.
[9] H. E. White, "Introduction to Atomic Spectra," McGraw-Hill Book Co., Inc., New York, N.Y.; 1934.
[10] P. L. Bender, E. C. Beaty, and A. R. Chi, "Optical detection of narrow Rb^{87} hyperfine absorption lines," *Phys. Rev. Letters*, vol. 1, pp. 311–313; November 1, 1958.
[11] R. Karplus, "Frequency modulation in microwave spectroscopy," *Phys. Rev.*, vol. 73, pp. 1027–1034; May 1, 1948.

Some Considerations in the Design of the Guidance and Control System for Discoverer*

JOHN J. SCHMITT, JR.†

Summary—**The limited number of flight tests to date has indicated that the Discoverer satellite will be a highly reliable and effective system from which the ARPA and the Air Force expect to gain valuable additional knowledge of outer space. The achievement of this high degree of reliability and effectiveness of the satellite means that each of its subsystems must, in fact, be even more reliable and effective. The Discoverer guidance and control system is meeting their specifications because of the simplicity of the over-all design—simplicity for reliability with sufficient sophistication to accomplish its mission effectively.**

The mission of the guidance system is that of providing adequate attitude, velocity, and time references to guide the satellite into a desired orbit, to control its attitude on orbit, and to provide switching in the proper sequence for certain principal satellite functions. The mission of the control system is simply that of positioning the vehicle in the proper attitude commanded by guidance. The investigations that were made and those which are being continued in the determination of the optimum configuration for the desired performance are described in some detail. The present system, is discussed, which comprises, for guidance, an inertial reference package, a horizon scanner, and a computer for grammar, and for control, both a hydraulic and pneumatic system.

In summary, a typical flight of the Discoverer, from separation from the Thor booster until stabilization on orbit, is outlined and the functions of the guidance and control systems are described.

THE limited number of flight tests to date has indicated that the Discoverer satellite will be a highly reliable and effective system from which the ARPA and the Air Force expect to gain valuable additional information and knowledge of outer space. The achievement of this high degree of reliability and effectiveness of the satellite means that each of its subsystems must, in fact, be even more reliable and effective. The Discoverer guidance and control system is meeting its specifications because of the simplicity of the over-all design—simplicity for reliability with sufficient sophistication to accomplish its mission effectively. It is the purpose of this article to describe the consideration given to this philosophy, simplicity with sophistication, in the design of the system.

First, the mission of the guidance and control system must be defined. The mission of guidance is that of providing adequate attitude, velocity, and time references to guide the satellite into a desired orbit, to control its attitude on orbit, and to provide switching in the proper sequence for certain principal satellite functions. The mission of control is simply that of positioning the vehicle in the proper attitude commanded by guidance. Although many involved and complicated techniques can be conceived to perform the missions defined, the approach in this case was to design a system which utilized simple, well-known, proven techniques as often as possible.

As previously defined, the function of guidance is to provide attitude, velocity, and time references. Consider these requirements separately. Many designs, including various inertial platforms, were considered for attitude determination. With some of the platform considered, it would have been necessary to use an autopilot which included a body-mounted inertial reference system. The logical next step in this investigation was to determine if a body-mounted gyro-reference system alone would be adequate. This would negate the high cost and added complexity of an inertial platform. In place of a detailed discussion of satellite trajectories, it will be sufficient to state that the vehicle attitude at injection into orbit is extremely critical in achieving a desired orbit. An analysis indicated that the typical autopilot reference gyros alone would not, under the expected environment, provide an adequate reference. Consideration was given to the possible use of a horizon-scanning device which would give an adequate reference and which could accordingly correct the autopilot gyros. A number of studies had been made which indicated that such a device was not only feasible, but that its development could be accomplished quickly and at nominal cost. The combination body-mounted, inertial-reference, package-horizon scanner appeared to be very promising, especially since the scanner had real potential for use on orbit as an attitude-indication and control-system reference device.

The velocity indication requirement was met simply with a longitudinal accelerometer whose output drives a motor-driven integrator.

Although more sophisticated and elaborate timing devices were investigated, an accurate electromechanical timer was chosen as a time reference. This timer was designed to include a number of cam-operated switches for the proper programming of certain satellite functions. If necessary, the cams are easily reset to accommodate various program changes from flight to flight.

The selection of a control system capable of accepting the guidance system commands and of accordingly positioning the satellite remained. The necessary servo loops which included the common use of rate gyros for stability purposes were designed. Because the attitude of the satellite must be controlled not only during the time when the orbital injection rocket engine is operating, but also before and after that period, two sets of "muscles" were necessary. Hydraulic actuators were chosen for the engine gimbaling in pitch and yaw. This hydraulic control system uses

* Manuscript received by the PGMIL, July 21, 1959.

† Major, U. S. Air Force, Ballistic Missile Division, AF Unit P.O., Los Angeles, Calif.

an electrically driven pump to supply the necessary pressure. To control the satellite in pitch and yaw at times when the rocket engine is not operating, and in roll at all times, an array of gas reaction jets was chosen. Consideration was given to simple on-off-type valves which supply gas to the appropriate jets but, because of the need for more accurate control at the minimum expenditure of stored gas, the development of proportional valves which supply gas to the appropriate jets in direct relation to the size of the required correction was undertaken. The choice of this pneumatic control system completed the determination of the components for the guidance and control system. Throughout the entire determination, the proper balance between simplicity and sophistication was uppermost in the minds of the designers.

To complete the description, it must be shown how these components are integrated into a system to perform the job of guiding the Discoverer into a desired orbit and of controlling its attitude on orbit. Upon separation from the Thor booster, the satellite coasts to a point just prior to the apogee of its ascent ellipse. The orbital injection rocket engine is started at this point and adds sufficient horizontal velocity to the vehicle to cause it to orbit. When the proper orbital velocity has been attained, the engine is shut down. The satellite, now on orbit, maintains a local horizontal attitude. Just prior to separation from the Thor, the inertial-reference package-position gyros are uncaged in order that they may use as a reference the attitude of the Thor/Discoverer at Thor burnout. Upon separation, the timer initiates a torquing program to the pitch gyro which causes the satellite, by operation of the gas jets, to pitch to the local horizontal. The timer then actuates the horizon scanner which maintains control of the vehicle in the local horizontal position through the inertial reference package and pneumatic control loop. At the proper time, the timer initiates the rocket-engine start sequence and switches control of the vehicle in pitch and yaw from the pneumatic system to the hydraulic system. The horizon scanner and intertial reference package continue to maintain control of the vehicle in the local horizontal position. During the orbital injection the longitudinal accelerometer and integrator operate to measure the velocity gained during this period. When the proper velocity has been gained, the integrator causes shutdown of the satellite engine. Once on orbit, the timer switches control of the vehicle in pitch and yaw back to the pneumatic control system. Horizontal attitude control on orbit, an important first in the increased performance of control systems, is thus maintained in the same manner as it was during the earlier coast phase of the vehicle's flight.

The ARPA, Air Force, and Lockheed (the prime contractor for the Discoverer), as well as those Lockheed subcontractors involved, are proud of our accomplishments. We are not, however, complacent. Components can be improved and simplified, power requirements can be reduced, as can be the number of switching functions. The latter are some areas in which we expect to gain more reliability and effectiveness.

Today more stringent and demanding guidance and control requirements challenge the Air Force and all associated industry. These requirements can and will be met by utilizing the knowledge gained from the Discoverer and other early satellite developments, and by applying the basic design philosophy—simplicity with sophistication.

Contributors

J. M. Andres was born on February 4, 1927, in Santa Ana, Calif. He received the B.S. and M.S. degrees in physics from the California Institute of Technology, Pasadena, in 1949 and 1950, respectively. In 1953 he received the Ph.D. degree in physics from the Massachusetts Institute of Technology, Cambridge.

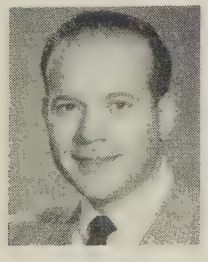

J. M. Andres

He was a graduate teaching assistant at Cal-Tech from 1949 to 1950, and a research assistant in the acoustics laboratory at M.I.T. from 1951 to 1953. Then, from 1953 to 1954, he was employed by the California Research Corporation, La Habra, Calif., working there on petroleum exploration problems. He joined the Ramo-Wooldridge Corporation, guided missile research division (later the Space Technology Laboratories), where he is presently employed, in 1954.

Dr. Andres is a member of the American Physical Society, Sigma Xi, and Tau Beta Pi.

❖

F. J. Clark (SM '58) was born in Alachua, Fla., on January 15, 1914. He received the B.E.E. degree from the University of Florida in 1940. He completed Naval Officer radar training and served 30 months as aviation electronic maintenance officer at Norfolk, Va., and Otis Field, Mass., during World War II.

F. J. Clark

After a short period at the Naval Research Laboratory, he spent five years with the Bureau of Aeronautics as project engineer on radar bombing and fire control systems. From 1951 to 1954, Mr. Clark was in various administrative engineering positions at the Air Force Missile Test Center. He joined RCA Service Company at

AFMTC and held supervisory assignments relating to instrumentation systems planning and coordination. Since early 1958, he has been an engineer in the Data Instrumentation Division of the Directorate of Range Development, Patrick AFB, Fla., with staff engineering supervisory duties for several radar and infrared instrumentation projects.

Mr. Clark is a member of IRIS (Infrared Information Symposium) and of the Radar Beacon Subcommittee, IRIG.

❖

Captain DePaul J. Corkhill was born at Lansford, Pa., on December 14, 1923. After taking metallurgical engineering studies, from 1941 to 1943 at Lehigh University, Bethlehem, Pa., he attended Villanova College, Pa., in 1943-1944, and studied premedical subjects. Thereafter, from 1944 to 1947, he attended the University of Pennsylvania, Philadelphia, and received the V.M.D. degree in 1947. In 1955 he began training in the medical aspects of nuclear radiation and has since attended courses at Oak Ridge, Tenn.; Nuclear Reactor Site, Hanford, Wash.; Los Alamos, N.M.; National Test Reactor, Idaho Falls; Nevada Test Site; and Sandia Base, N.M. In 1958 he graduated from the radiobiology course at Reed College, Portland, Ore., and received the equivalent of the M.S. degree in radiobiology.

DEPAUL CORKHILL

Shortly after 1947, Dr. Corkhill joined the Department of Agriculture and spent two years in Mexico campaigning against the foot-and-mouth disease epidemic there. He became district supervisor and took on the responsibility of eliminating this disease in three states. Then, returning to the United States, he practiced veterinary medicine with his father until 1951. In 1951, under the doctor's draft, he was called into military service, and became an Air Force Reserve Officer; in 1953 he was called into active duty. Currently, as chief of the operations section at the aeromedical field laboratory of the Air Force Missile Development Center, Holloman AF Base, N.M., he is engaged in monitoring a contract for a cosmic ray counter which will be capable of counting, telemetering, and recording primary cosmic rays at any altitude.

Dr. Corkhill is a member of the American Veterinary Medical Association.

❖

Donald J. Farmer was born in Morenci, Ariz., on April 7, 1925. He received the B.S. and Ph.D. degrees in physics from the University of Washington, Seattle, in 1950 and 1954, respectively.

He was a research associate at the University of Washington from 1954-1955. Then he joined the Ramo - Wooldridge Corporation, guided missile research division (later the Space Technology Laboratories), where he is presently employed, in 1955. He has been working on radio propagation problems and atomic frequency standards since that time.

D. J. FARMER

Dr. Farmer is a member of the American Physical Society and Sigma Xi.

❖

Fritz W. Hoehndorf was born in Berlin, Germany on March 30, 1900. He received the Ph.D. degree in applied mathematics from the University of Berlin in 1926.

At the end of World War II he was director of the Institute for Atmospheric Physics of the German Research Center for Gliding (DFS), where his work was, for the most part, connected with gliding meteorology. After four years with the German Weather Service, he came to Holloman AFB, N.M., in 1953, where he has been working on radiation and feasibility studies of missiles.

F. W. HOEHNDORF

❖

Captain Rudolf A. Hoffman was born at Ballinger, Tex., on May 16, 1932. He received the D.V.M. degree from Texas A & M College, College Station, in 1955. In 1958 he completed a one-year course in advanced radiobiology for medical officers at Reed College, Portland, Ore. He has also attended courses at Oak Ridge, Tenn.; Nuclear Reactor Site, Hanford, Wash.; Nevada Test Site; Sandia Base, N.M.; and Walter Reed Army Institute of Research, Washington, D.C.

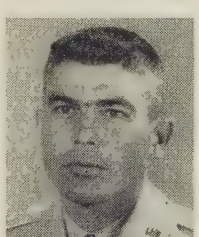

R. A. HOFFMAN

Dr. Hoffman entered the Air Force in 1955 and was assigned to active duty at Gunter AFB, Ala. He later served as base veterinarian at Randolph AFB, Tex. In 1958 he was assigned to the aeromedical field laboratory of the Air Force missile development center, Holloman AFB, N.M., where as a task scientist in the operations section, he is currently doing radiobiological work in the bioastronautics branch which is connected with biomedical programs designed for research into human space flight.

Dr. Hoffman is a member of Phi Zeta, Phi Kappa Phi, the American Veterinary Medical Association, and the American College of Veterinary Toxicologists.

❖

George T. Inouye (S'46-A'53-M'58) was born on November 27, 1922, in Sacramento, Calif. He received the B.S. degree in electrical engineering from Swarthmore College, Swarthmore, Pa., in 1944 and the Ph.D. degree in applied physics from Harvard University, Cambridge, Mass., in 1953.

G. T. INOUYE

He was employed by Technicolor Corporation, Hollywood, Calif., from 1953 to 1957. Then, in 1957, he joined the Ramo-Wooldridge Corporation guided missile research division (later the Space Technology Laboratories) where he is presently employed.

Dr. Inouye is a member of Sigma Xi.

❖

Aubrey B. Mickelwait was born in Honolulu, Hawaii, on May 2, 1925. He received the B.S., M.S., and Ph.D. degrees in physics, from Carnegie Institute of Technology, Pittsburgh, Pa.

A. B. MICKELWAIT

He has had six years' experience in the quantum field theory, theoretical physics, meson theory and is the author of several technical papers. He joined Space Technology Laboratories, Los Angeles, Calif., in 1955 as a member of the technical staff and is presently head of the Navigation Section, Guidance and Navigation Department of the Guidance Research Laboratory. There he has been engaged in research and systems analysis work on the Atlas, Titan, Thor, and Minuteman guidance systems. During the last several years, he has done theoretical and design work on trajectories, payloads, and guidance systems for space vehicles such as the Pioneer moon flights.

Dr. Mickelwait is a member of the American Physical Society, American Geophysical Union, Sigma Xi, Institute of Aeronautical Sciences, and Tau Beta Pi.

Robert A. Park was born in Stockholm, Sweden on September 4, 1923. He received the M.A. degree in English in 1949 and the Doctor of Laws degree in 1955, both from the University of Chicago, Chicago, Ill.

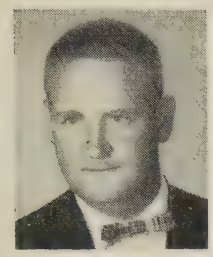

R. A. Park

From 1949 to 1950, he taught creative writing at the University of Chicago; during 1949, he taught English at the University of Illinois, Urbana; from 1949 to 1955, he taught English, humanities, and reading at Wilson Junior College, Chicago, Ill. From 1955 to 1957, he was an Assistant Attorney General for the State of Oregon. He joined Space Technology Laboratories, Los Angeles, Calif., in July, 1957, and is presently connected with a special project on the Executive Vice-President's staff.

Mr. Park is a member of the Oregon Bar Association and the California Bar Association.

❖

Major John J. Schmitt, Jr., graduated from West Point Military Academy in 1946 and in 1951 attended the USAF Institute of Technology at Wright - Patterson Air Force Base, Dayton, Ohio, where he attended a fifteen-month course in graduate armament engineering. He continued his education at the Massachusetts Institute of Technology, Cambridge, where he studied weapon systems engineering and received the M.S. degree in 1954.

J. J. Schmitt

In 1946, he was assigned to the Strategic Air Command where his primary duty was that of pilot and aircraft commander on B-29's and B-50's. In 1954, he was arming and fuzing project officer at the Air Force Special Weapons Center, Kirtland AF Base, N.M. He was assigned to the Air Force Ballistic Missile Division, Los Angeles, Calif., early in 1958, to his present duty as guidance and control project officer for Discoverer.

❖

John E. Taber was born on May 23, 1925, in Burbank, Calif. He received the B.S. degree in electrical engineering in 1946 from the California Institute of Technology, Pasadena, and the M.S. degree in electrical engineering from the University of California, Berkeley, in 1951.

In 1946, Mr. Taber joined the Hughes Aircraft Company, Los Angeles, Calif., where he worked on instrumentation and telemetry equipment. In 1948 he became employed by the Glenn L. Martin Company, Baltimore, Md., in the telemetry section. Upon returning to Hughes Aircraft Company in 1950, he did development work on high-speed digital communication systems. He continued this type of work at the communication division of the Ramo-Wooldridge Corporation, Los Angeles, from 1954 to 1958. He joined Space Technology Laboratories, Inc., Los Angeles, in 1958 and is presently associate manager of the instrumentation department there. Mr. Taber holds three patents concerning digital communication techniques.

J. E. Taber

❖

Edwin H. Tompkins, Jr. (S'48-A'50-M'56) was born in Charlottesville, Va. on October 9, 1928. He received the B.S. degree in electrical engineering in 1948 from Virginia Polytechnic Institute, Blacksburg, Va. and the M.S. and Ph.D. degrees in 1952 and 1955, respectively from North Carolina State College, Raleigh.

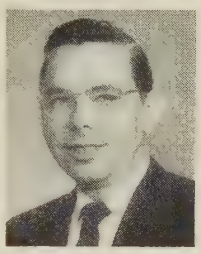

E. H. Tompkins

From 1951 to 1957, he was associated with the Rocket Research Group at North Carolina State College, working in exterior ballistics of rocket flight. During 1957 and 1958, he was assistant professor of mathematics and electrical engineering at the college and has had experience in electrical circuit theory and nonlinear mechanics. He joined Space Technology Laboratories, Los Angeles, Calif., in 1958 and is presently a member of the technical staff, Guidance and Navigation Department of the Guidance Research Laboratory, Research and Development Division.

Dr. Tompkins is a member of the American Mathematical Society and Sigma Xi.

❖

Major Henry Triwush was born in Chicago, Ill., in 1919. He received the B.S. degree in chemistry from the University of Chicago in 1940 and did further graduate work there. In 1946-1947, part of which time he had a Lederle fellowship, he attended Northwestern University in Evanston, Ill. and received the M.S. degree in physical chemistry in 1949.

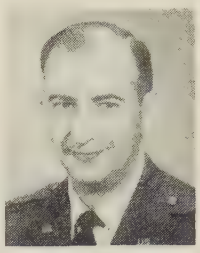

H. Triwush

In 1942, he joined the Central Laboratory of Division 10 of the NDRC, located at Northwestern University, where he assisted in research on gas mask absorbents. He enlisted in the Army Air Corps in 1942 and received his commission as a navigator in 1944. After a combat tour with the Eighth Air Force in England, he returned to this country for duty as a radar-bombardier instructor until he reverted to inactive status in 1945. He was recalled to active duty in 1948 and has remained in the Air Force since that time. Major Triwush's principal service assignments since recall have been with the Strategic Air Command, with the Electronics Components Laboratory, Wright Air Development Center, Dayton, Ohio, and currently, after having attended the Air Force Command and Staff School, with the Air Force Ballistic Missile Division, where his duties involve dealing with space system reliability problems.

Major Triwush is an associate member of Sigma Xi and a member of Phi Lambda Upsilon. Presently, he holds the aeronautical rating of master navigator.

❖

Paul F. von Handel was born in Bisenz, Austria, on January 30, 1901. He received the M.S. degree from the Technical University, Munich, Germany, and later, the Ph.D. degree in electronics from the Technical University, Berlin, Germany, in 1931.

P. F. von Handel

He was formerly director of the Institute for Electronics Research of DVL in Berlin, a member of the German Academy of Sciences, president of the Board of Electronic Navigation, and professor at the Technical University, Berlin. His special fields of activity were studies on wave propagation and electronic navigation, for which he received the Lilienthal Prize for Aeronautical Research in 1944.

He arrived in the U.S.A. in 1953, and has since been working on problems related with kinematics, guidance and control of guided missiles, wave propagation, and electronic warfare.

Dr. von Handel is presently chief of the Orbital Mechanics Division, Directorate of Advanced Technology, Air Force Missile Development Center, Holloman, AFB, N.M.

IRE Transactions on Military Electronics

Index to Volume MIL-3, 1959

Contents

Index to Authors

Index to Subjects

INFORMATION FOR AUTHORS

The PGMIL TRANSACTIONS is intended to bridge the gap between the various disciplines contributing to military electronics. Since this includes most of the branches of electronics, the military, and many fields which are associated with but not actually within the realm of electronics, it is essential that the papers published be of broad interest. The emphasis should be on readable, thought-provoking material that stimulates an attitude of open mindedness and curiosity.

Papers are solicited in the following general subject categories:

Military sciences—Military science fiction, famous battles involving electronics, basic problem areas of military electronics.

Technical survey—Tutorial technical papers on radar, communications, navigation, systems and operations research, etc.

Integrating papers—Integration of concepts common to several fields, as for example, wave phenomena, information theory, etc.

Physical sciences—Fundamentals of modern physics that may influence the future of military electronics.

Mathematical concepts—Applications and implications of modern mathematical methods.

Associated subjects—Survey of fields that are neither military nor electronic but which are important to the advancement of military electronics.

Manufacturing—Industrial and military problems of reliability, quality control, etc.

It is requested that each paper be submitted in duplicate. Standard IRE practice should be followed in preparation of the manuscript and illustrations. Papers should be sent to James Q. Brantley, Jr., or Donald R. Rhodes, PGMIL Editors, P.O. Box 6904, Orlando, Fla.

INVITATION TO MEMBERSHIP IN PGMIL

Members of the IRE may join the Professional Group on Military Electronics as active, voting members by payment of the annual fee of $2.00. Nonmembers of the IRE who qualify may become nonvoting affiliates under the new IRE affiliate Plan by payment of an annual fee of $4.50 in addition to the assessment of the Group. All applications for membership affiliation should be addressed to the Chairman of the PGMIL Membership Committee, William M. Richardson, The Ramo-Wooldridge Corporation, 1300 Connecticut Ave., Washington 6, D.C., or to IRE Headquarters.

INSTITUTIONAL LISTINGS

The IRE Professional Group on Military Electronics is grateful for the assistance given by the firms listed below, and invites application for Institutional Listings from other firms interested in the field of Military Electronics.

PHILCO CORP., Government and Industrial Div., 4700 Wissahickon Ave., Philadelphia 44, Pa.
Microwave, Radar, Computer, Guided Missile and Other Military Electronics Production, Research and Engineering

THE RAMO-WOOLDRIDGE CORPORATION, 5730 Arbor Vitae St., Los Angeles 45, Calif.

REPUBLIC AVIATION CORPORATION, Farmingdale, N. Y.
Aircraft and Missile Design and Manufacture

TEXAS INSTRUMENTS, INC., 6000 Lemmon Ave., Dallas 9, Texas
Radar, Sonar, M.A.D., Infrared, and Other Electronic and Electromechanical Apparatus and Systems

The charge for an Institutional Listing is $75.00 per issue or $225.00 for four consecutive issues. Applications for Institutional Listings and checks (made out to the Institute of Radio Engineers) should be sent to Mr. L. G. Cumming, Technical Secretary, Institute of Radio Engineers, 1 East 79th Street, New York 21, N. Y.